

University of Minho
School of Engineering

Irving Leander Reascos Valencia

**Quantum Simulation of spin systems
on Quantum Computers**



University of Minho
School of Engineering

Irving Leander Reascos Valencia

**Quantum Simulation of spin systems
on Quantum Computers**

Masters Dissertation
Master's in Engineering Physics

Information Physics
Dissertation supervised by
Ph.D. Nuno Miguel Machado Reis Peres
Ph.D. Joaquín Fernández-Rossier

Copyright and Terms of Use for Third Party Work

This dissertation reports on academic work that can be used by third parties as long as the internationally accepted standards and good practices are respected concerning copyright and related rights.

This work can thereafter be used under the terms established in the license below.

Readers needing authorization conditions not provided for in the indicated licensing should contact the author through the RepositóriUM of the University of Minho.

License granted to users of this work:



CC BY

<https://creativecommons.org/licenses/by/4.0/>

Acknowledgements

I would like to express my heartfelt gratitude to several individuals and institutions who have been instrumental in my journey throughout my Master's program. Your support, guidance, and encouragement have made a profound impact on my academic and personal development. I sincerely appreciate my supervisors: Joaquín Fernández-Rossier, Ernesto Galvão, Bruno Murta, and Nuno Peres, who have been invaluable throughout my journey. Your invaluable support, insights, and guidance have been essential. I'm deeply grateful for your mentorship, igniting my passion for my Master's subjects. Your wisdom will greatly impact my academic future.

To my family, I am eternally grateful for your unwavering support and trust. Irving, my father, and Silvia, my mother, allowed me to pursue my dreams by coming to Portugal. Even when you had to return to Ecuador, you believed in me and gave me the chance to stay in Portugal, continue my studies, and grow as an individual. My brothers, Andrés and Alejandro, who shared this journey with me, your presence has been invaluable. Our shared moments, whether playing basketball, exploring Minecraft, or simply spending time together, have been treasured. Lastly, to my beloved girlfriend, Brisell, or "Bris" as I affectionately call you, you've been my rock and unwavering support, helping me overcome the toughest days. Your presence in my life has been a source of strength and inspiration, and the love and happiness we've shared have been the driving force behind my accomplishments.

I'd also like to acknowledge my friends, who have been a source of motivation and camaraderie throughout my academic journey. To Barros, Gabriel, Magda, Rodrigo, Sara, and Tiago, the *TEKKENLAB* group, I extend my heartfelt thanks for the memorable moments we've shared.

I'm grateful to the International Iberian Nanotechnology Laboratory (INL) for the research opportunity during my Master's program and to the Calouste Gulbenkian Foundation for the New Talents grant, which connected me with a remarkable scholarly community. Your collective support has made this journey enriching and fulfilling experience, and I am truly grateful for each and every one of you.

Statement of Integrity

I hereby declare having conducted this academic work with integrity.

I confirm that I have not used plagiarism or any form of undue use of information or falsification of results along the process leading to its elaboration.

I further declare that I have fully acknowledged the Code of Ethical Conduct of the University of Minho.

University of Minho, Braga, october 2023

Irving Leander Reascos Valencia

Abstract

Quantum simulation represents a formidable challenge for classical computers due to the intricate behavior of quantum systems. Digital quantum computers aim for precise approximations of a wide range of quantum systems. Within the realm of quantum simulation, the study of spin systems plays a pivotal role, providing insights into complex properties challenging to model through classical means. This work focuses on investigating chiral spin systems through the development of a dedicated quantum circuit for chirality measurement.

In this Masters Dissertation, we present an overview of the current state-of-the-art in quantum simulation of chiral spin systems and introduce our approach to addressing this challenge. Scalar spin chirality, a three-body physical observable, holds a critical position both in classical magnetism, where it characterizes non-coplanar spin textures, and in quantum magnetism, serving as an order parameter for chiral spin liquids. In the context of quantum information, scalar spin chirality serves as a witness to genuine tripartite entanglement.

In this study, we delve into various methodologies to tackle the problem at hand, subjecting them to comparison. The objective is to identify the most suitable approach that demands fewer quantum resources. Our best proposed method introduces an indirect measurement scheme based on the Hadamard test, designed to estimate the scalar spin chirality for general quantum states. We apply this innovative approach to measure chirality in two specific types of quantum states: the generic one-magnon states of a ferromagnet and the ground state of a model characterized by competing symmetric and antisymmetric exchange interactions.

Our research findings highlight the practicality of achieving a single-shot determination of scalar chirality for chirality eigenstates, leveraging the power of quantum phase estimation with a single auxiliary qutrit. This novel methodology extends beyond providing a solution to the chirality measurement problem; it also unifies the theory of chirality in both classical and quantum magnetism. The implications of our work offer valuable insights and pave the way for future quantum research endeavors in this domain.

Keywords Quantum Simulation, Magnetism, Quantum Entanglement, Magnetic Order

Resumo

A simulação quântica desafia os computadores clássicos devido ao comportamento complexo dos sistemas quânticos. Os computadores quânticos digitais buscam aproximar uma ampla variedade de sistemas quânticos. Na simulação quântica, a análise de sistemas de spin é essencial para compreender propriedades complexas difíceis de modelar com abordagens clássicas. Este estudo concentra-se em investigar sistemas de spin com quiralidade por meio do desenvolvimento de um circuito quântico dedicado para medição.

Nesta Dissertação de Mestrado, apresentamos um panorama atual da simulação quântica de sistemas de spin com quiralidade e introduzimos nossa abordagem para abordar esse desafio. O operador de quiralidade, um observável físico de três corpos, desempenha um papel crítico no magnetismo clássico, caracterizando texturas de spin não coplanares, e no magnetismo quântico, atuando como um parâmetro de ordem para líquidos de spin com quiralidade. No contexto da informação quântica, a quiralidade serve como testemunha de entrelaçamento tripartite genuíno.

Neste estudo, exploramos várias metodologias para abordar o problema em questão, comparando-as com o objetivo de identificar a mais eficiente em termos de recursos quânticos. O nosso melhor método proposto é um esquema de medição indireta baseado no teste de Hadamard, criado para estimar a quiralidade do spin em estados quânticos gerais. Aplicamos esta abordagem para medir a quiralidade em dois tipos específicos de estados quânticos: os estados genéricos de um magnon de um ferromagneto e o estado fundamental de um modelo com interações de troca simétricas e antissimétricas em competição.

As descobertas de nossa pesquisa destacam a praticidade de alcançar uma determinação única da quiralidade do spin para estados com quiralidade, aproveitando o poder da estimativa de fase quântica com um único qubit auxiliar. Essa metodologia inovadora vai além de fornecer uma solução para o problema de medição de quiralidade; ela também unifica a teoria da quiralidade tanto no magnetismo clássico quanto no magnetismo quântico. As implicações de nosso trabalho oferecem conhecimentos valiosos e abrem caminho para futuras esforços de pesquisa quântica nesse domínio.

Palavras-chave Simulação Quântica, Magnetismo, Entrelaçamento Quântico, Ordem Magnética.

Contents

1	Introduction	1
1.1	Motivation	2
1.2	Minimal Background	5
1.2.1	Quantum Simulation	5
1.2.2	Classical Spin States	6
1.2.3	Quantum treatment	8
1.2.4	Scalar Spin Chirality	10
1.3	Objectives	11
1.4	Outline of the Document	12
2	Theoretical Background and Methodology	14
2.1	Quantum Simulation	14
2.1.1	Analog and Digital Quantum Simulators	14
2.1.2	Designing a Quantum Simulation	16
2.2	Digital Quantum Computers	18
2.3	Quantum Circuits and Techniques	21
2.3.1	Lie-Trotter-Suzuki Formula	21
2.3.2	Linear Combination of Unitaries (LCU)	22
2.3.3	Quantum Fourier Transform (QFT)	24
2.3.4	The Hadamard Test	25
2.3.5	Quantum Phase Estimation (QPE)	27
2.3.6	Efficient Implementation of $ W\rangle$ States	29
2.4	Spin Systems	31
2.4.1	Spin	31
2.4.2	Spin Operators and Their Eigenstates	34

2.4.3	Heisenberg Model	36
2.4.4	Spin Waves	36
2.4.5	Zeeman Effect	38
2.4.6	Dzyaloshinskii-Moriya interaction (DMI)	38
2.5	Spin Chirality	40
2.6	Genuine tripartite entanglement and spin chirality	42
2.7	Methodology	44
2.7.1	Python	44
2.7.2	Analytical Calculations	44
2.7.3	Computer-Assisted Simulations	45
3	Chirality Eigenstate Preparation	47
3.1	Building Chirality Eigenstates	48
4	Chirality Measurement	51
4.1	Characterizing Chirality through Permutation Operations	51
4.2	Employing the Linear Combination of Unitaries (LCU) method for Chirality Operator Implementation	53
4.2.1	Chirality Operator using LCU	53
4.3	Measuring Chirality via Hadamard Test and LCU	54
4.3.1	Combining the Hadamard Test and LCU Algorithm	55
4.4	Time Evolution Chirality Operator	58
4.5	Using Quantum Phase Estimation (QPE) for Chirality Determination	60
4.5.1	QPE with Qutrits	63
4.6	Assessing Chirality using the Cycle Test	65
4.7	Selecting the Best Approach	67
5	Chirality in Spin Models	70
5.1	Broken symmetry magnetism and Bargmann invariants	70
5.2	Spin chirality and tripartite entanglement of one-magnon states	73
5.3	Scalar spin chirality in spin spirals	74
5.3.1	Classical treatment	75
5.3.2	Quantum Ground State and Broken Symmetry	77
5.3.3	Classical and Quantum Chirality	79

6 Conclusions and Future Work **83**

6.1 Conclusions 83

6.2 Future Work 85

List of Figures

- 1 Schematic representation of the General Structure of a Quantum Simulation. Figure 1a depicts the target system, which represents the natural system under analysis. Figure 1b illustrates the mapping of the target system into the quantum simulator, along with the corresponding states of the simulation. 5

- 2 The figure illustrates a general pure state $|\psi\rangle$ defined by the azimuthal angle θ and the polar angle φ . The azimuthal angle provides us with the amplitudes of the state $|0\rangle$ and $|1\rangle$, while the polar angle represents the complex phase between the computational basis states $|0\rangle$ and $|1\rangle$. The state $|+\rangle$ corresponds to the eigenstate with a positive eigenvalue of the Pauli- X operator and can be described by $\theta = \frac{\pi}{2}$ and $\varphi = 0$. Similarly, the state $|i\rangle$ is the eigenstate with a positive eigenvalue of the Pauli- Y operator and is characterized by $\theta = \frac{\pi}{2}$ and $\varphi = \frac{\pi}{2}$ 19

- 3 LCU algorithm for a linear combination of two unitary operators U and V . The dashed box represents the implementation of the operator \mathcal{O}_S , which combines the unitaries U and V . The operator $P(\varphi)$ is a phase gate that adds the phase φ required in the weight of the operator V 22

- 4 LCU algorithm for a linear combination of two unitary operators U and V 24

- 5 The figure illustrates the circuit implementation of the Quantum Fourier Transform (QFT) for an input state $|j\rangle$. It is important to note that the resulting product state at the end of the circuit is in reverse order compared to Equation 2.14. This reversal can be addressed by incorporating swap gates or by considering the reversed order when applying the circuit. 25

6	Scheme of the Hadamard Test for estimating the expectation value of the unitary operator U on the quantum state $ \psi\rangle$. The measurement of the ancilla qubit in the X basis ($b = 0$) yields the real part of $\langle\psi U \psi\rangle$, while the measurement in the Y basis ($b = 1$) yields the imaginary part. The operation S^\dagger introduces a phase of $e^{-i\frac{\pi}{2}}$ when $b = 1$, enabling the measurement of the imaginary part.	26
7	The circuit represents the Quantum Phase Estimation (QPE) algorithm, where U is the unitary operator of interest, $ \psi\rangle$ is the quantum eigenstate of U with eigenvalue $e^{i2\pi\phi}$, and n is the number of qubits in the ancillary register. The box labeled with $\mathcal{O}(U)$ represents the oracles corresponding to the controlled operations. The j -th qubit controls the operation $U^{2^{n-j}}$. Upon measurement, the state $ \varphi\rangle$ is obtained, where φ is the integer that provides the best estimate for $2^n\phi$	29
8	Decomposition of the $B(p)$ operator into a controlled $G(p)$ operation and a inverted $CNOT$ gate Cruz et al. [2019].	30
9	The Figure 9a shows the dichotomy tree for the case $N = 5$. The leaves on the right side of the tree correspond to the "lower child," while the leaves on the left side correspond to the "upper child." The Figure 9b displays the pruned tree obtained from the unpruned tree shown in the left figure. In the pruned tree, the node $(0, 1)$ has been removed. To clarify the control qubit for each leaf, the notation used for each node is (c, n, m) , where c represents the index of the control qubit (starting from 0), and n and m retain the same values as in the unpruned tree.	31
10	Quantum circuit for implementing the $ W\rangle_5$ state using the pruned dichotomy tree in 9b. Each block delimited by the barrier represents a parallel execution block, where, for instance, $B(\frac{1}{2})$ and $B(\frac{1}{3})$ are executed simultaneously. This reflects the logarithmic depth of the method, which in this case is $\lceil\log_2 5\rceil = 3$	32
11	Controlled $G(p)$ operator decomposition.	32
12	The figure depicts the schematic representation of the Stern-Gerlach experiment. It illustrates the particle source, the magnetic monopoles creating an inhomogeneous magnetic field \vec{B} , and the screen detector where particles are detected after passing through the magnetic field.	33

13	Schematic representation of the Stern-Gerlach experiment results: 13a Using classical magnetic dipoles with different orientations of their magnetic moments $\vec{\mu}$ relative to the \hat{z} axis, the magnets deflect them based on their orientations, resulting in a distribution across the screen detector that spans the entire \hat{z} axis. 13b In the quantum case, neutral spin- $\frac{1}{2}$ particles with various initial states are considered. The diagram illustrates the deflection of these particles to only two distinct points on the \hat{z} axis, determined by their \hat{z} spin components.	34
14	The figure illustrates a schematic representation of a 1D Heisenberg chain with periodic boundary conditions. Here, a represents the lattice constant, such that each spin particle is positioned at $r_i = (i - 1)a$, where $i \in [1, N]$, along the 1D chain. The value J signifies the exchange constant, determining the strength of interactions. It's important to note that the spin orientations shown are arbitrary, and the diagram is solely intended for didactic purposes.	37
15	Zeeman splitting effect due to an applied magnetic field $\vec{B} = B_z \hat{z}$. The blue line corresponds to the splitting for the state $ \frac{1}{2}, \frac{1}{2}\rangle$, and the red one corresponds to the state $ \frac{1}{2}, -\frac{1}{2}\rangle$. The energy difference between the cases with and without a magnetic field is $\Delta z = g\mu_B B_z \frac{1}{2}$	39
16	Illustration of the Dzyaloshinskii-Moriya Interaction (DMI). Electrons (red) in a crystal lattice experience a spin-orbit coupling influenced by the atomic nuclei (blue). This interaction induces a vector $\vec{D} \propto \vec{R} \times \vec{r}_{ij}$ that leads to non-collinear magnetic order in the material.	39
17	The volume of the parallelepiped is given by $V = h \cdot A_{\text{base}}$, where $h = \cos \alpha$ represents the height and $A_{\text{base}} = \sin \theta$ the area of the base. These relationships can be intuitively understood through geometry. Alternatively, the triple product $\vec{n}_1 \cdot \vec{n}_2 \times \vec{n}_3 = \cos \alpha \sin \theta$ yields the same result.	40
18	The figure shows a schematic representation of the Hubbard model. The blue arrow represents the hopping of one electron from site i to site j . Additionally, at the site with two electrons, there is the Coulomb repulsion term.	42
19	The figure shows a schematic representation of the Concurrence Fill. The vertices represent the qubits, and the edges are labeled as C_{ij} , where i and j correspond to the vertices of the edge. The length of the edge between qubits i and $j \in \{1, 2, 3\}$ is determined by the square bipartite concurrence C_{ij}	43

20	This figure depicts the quantum circuit $ W\rangle_3 \langle 0 ^{\otimes 3}$ that prepares the $ W\rangle_3$ state. . . .	49
21	The left Figure represents the quantum algorithm in the form of a circuit, with the corresponding values for the phases provided in the table on the right. The values of these phases depend on the desired state to be prepared. For states with zero chirality, no phase is applied. For states with positive chirality, the phases used are ω and ω^2 , while for states with negative chirality, the phases are ω^2 and ω , as indicated in the table and explained in the text. The value of a in the last operator changes between states with $S_z = \frac{1}{2}$ when $a = 0$, and $S_z = -\frac{1}{2}$ when $a = 1$	50
22	The figure illustrates the Linear Combination of Unitaries (LCU) method for applying the chirality operator using the permutation description in 4.4. The dashed box represents the controlled operation R , while the dotted box represents R^\dagger	54
23	Circuit diagram showcasing the combined approach of the LCU algorithm and the Hadamard Test for measuring the expectation value of the chirality operator. The controlled version of the operator $\hat{\chi}$ is implemented using the LCU method (dashed box), enabling the measurement of the chirality operator's expectation value.	56
24	The figure displays the probabilities of measuring each basis state of $n = 2$ qubits using the QPE algorithm, obtained through a noiseless simulation using Qiskit. The simulation consisted of $N_{\text{shoots}} = 2,500$ runs to estimate the probabilities with an error of $\varepsilon = 0.01$, represented in the figure by error bars. Figure 24a shows the probability estimation using the chirality eigenstate $ \chi = -1\rangle$ as the input, figure 24b corresponds to $ \chi = 0\rangle$, and figure 24c corresponds to $ \chi = 1\rangle$. The x-axis of each figure also represents the corresponding values of $\frac{\varphi}{2^2}$. The chirality eigenvalue was estimated by considering the state with the highest probability (see Table 5).	62
25	The figure depicts the Hadamard test for the unitary operator $U_\chi\left(\frac{2\pi}{3}\right) = R$, indicated by the dashed box. As mentioned in the main text (see Subsection 2.3.4), when measured in the Y basis ($b = 1$), the result corresponds to the imaginary part of the unitary operator R , which in this case gives $\langle \psi \hat{\chi} \psi \rangle$ (see Equation 4.25). On the other hand, the measurement in the X basis ($b = 0$) captures the real part of R , which is associated with $\langle \psi \hat{\chi}^2 \psi \rangle$ (see Equation 4.25).	66

26	Figure 26a illustrates the schematic representation of the unitary vector \vec{n} characterized by the polar angle φ and azimuthal angle θ . Additionally, Figure 26b depicts a schematic representation of a general coherent state $ \vec{n}\rangle$ in the Bloch sphere, demonstrating the relationship between the state and the classical vector \vec{n}	71
27	Estimation of scalar spin chirality $\hat{\chi}$ in spin-wave states defined on an N -site ring. The maximal value of $\hat{\chi}$ across all trios of spins- $\frac{1}{2}$ and all N spin-wave states is shown in black (Equation 5.10). The same values were estimated using the Hadamard test in Fig. 25 with 10,000 samples for each N , shown in blue. The horizontal dashed line marks the threshold for genuine tripartite entanglement Tsomokos et al. [2008]. While the scalar spin chirality surpasses this threshold only for $N = 3$, the concurrence fill Xie and Eberly [2021], a measure of tripartite entanglement, confirms its existence for all system sizes in the plot. The black and red solid lines emphasize the decay of $\hat{\chi}$ and the concurrence fill with the system size N	75
28	The figures display the simulation results obtained using QuSpin for a ring with $N = 10$ particles, $J = 1$, and $D = -J \tan \frac{2\pi}{N}$. In these simulations, the operator \vec{S}_i was measured for each particle $i \in [1, N]$ in two systems: one without a local magnetic field ($B_x = 0$, 28a) and the other with a local magnetic field ($B_x = -1$, 28b) to achieve a broken-symmetry ground state. The dashed lines in the figures represent the analytical solutions obtained through classical analysis.	78
29	The figures display the simulation results obtained using QuSpin for a ring with $N = 10$ particles, $J = 1$, and $D = -J \tan \frac{2\pi}{N}$. In these simulations, the correlator $S_1^\alpha S_i^\alpha$, $\alpha \in \{x, y, z\}$ was measured for each particle $i \in [2, N]$ in two systems: one without a local magnetic field ($B_x = 0$, 29a) and the other with a local magnetic field ($B_x = -1$, 29b) to achieve a broken-symmetry ground state. The dashed lines in the figures represent the analytical solutions obtained through classical analysis. In subfigure 29a, the dashed lines represent the analytical classical solutions for $\langle S_1^\alpha S_i^\alpha \rangle$, where $\alpha \in \{x, y\}$	79

- 30 Simulation results for the chirality measurement of the Hamiltonian in Equation 5.11 for $B_x = 0$ (30a) and $B_x = -0.1$ (30b) with varying $B \in [0, 1]$. The Quantum Ground State (QGS) was obtained through exact diagonalization using QuSpin. The Classical Ground State (CGS) was obtained by minimizing the classical energy $E(\theta, q)$ (Equation 5.23). In the case where $B_x = 0$, the ground state is a superposition of an infinite set of spin spirals, resulting in a classical chirality of zero. However, in the case with $B_x = -0.1$, the system leads to a broken-symmetry ground state that allows the existence of classical chirality. Black curve: Exact quantum chirality $\langle \hat{\chi}_{149} \rangle$. Blue dots: Estimated quantum chirality using the cycle test circuit in Qiskit. Green: Classical chirality $\langle \chi_{149}^{cla} \rangle$ computed from the box product of classical spin vectors $\vec{s}_i = (\langle S_i^x \rangle, \langle S_i^y \rangle, \langle S_i^z \rangle)$ over the QGS (see Equation 5.24). Red: Classical chirality χ_{149}^{cla} calculated using Equation 5.22 with values of θ and q_{min} from the CGS. 81
- 31 Classical spin vectors for three different values of B . The left figure corresponds to $B = 0$, and its spin configuration is a coplanar spin spiral with zero chirality. In the middle figure, for $B = 0.17$, the maximum quantum chirality is observed, and the non-zero classical chirality is apparent due to the non-coplanar spin configuration. The right figure, for $B = 1$, shows zero chirality, with the spins aligned with the external magnetic field. The chirality values were presented in Figure 30. 82

List of Tables

1	Common Quantum Gates and Their Representations. There are specific cases for the phase gate $P(\phi)$, namely: $P\left(\frac{\pi}{2}\right)$ corresponds to the S gate, and a phase of $\phi = \frac{\pi}{4}$ gives the T gate.	20
2	Single-Qubit Rotation Gates	21
3	The table summarizes the results obtained by simulating the circuit shown in Figure 22 that apply the LCU method to estimate $\langle \hat{\chi}^2 \rangle$ for each chirality eigenstate. The error is given by $\varepsilon = \frac{8}{\sqrt{N_{shoots}}} = 0.08$, where $N_{shoots} = 10\,000$	55
4	The table summarizes the results obtained by simulating the circuit shown in Figure 23 that uses the Hadamard Test and the LCU method to estimate $\langle \hat{\chi} \rangle$ for each chirality eigenstate. The error is given by $\varepsilon = \frac{4}{\sqrt{N_{shoots}}} = 0.04$, where $N_{shoots} = 10\,000$	57
5	Estimated eigenvalues $\chi = \lambda$ using QPE. The estimation error is limited by the precision determined by the number of qubits. With $n = 2$ qubits, the binary fraction error is bounded by $\delta_{max} = \frac{1}{2^{n+1}} = 0.125$. Consequently, the chirality estimation error is $\epsilon = 3\delta_{max} = 0.375$. The measured value of $\frac{\phi}{2^2}$, providing the best approximation of the binary fraction representing $\phi = -\frac{\lambda}{3}$, was obtained by selecting the result with the highest probability from simulations with different input states (see Figure 24).	63
6	Estimated eigenvalues $\chi = \lambda$ using QPE with $n = 5$ qubits. The estimation error is limited by the precision determined by the number of qubits. With $n = 5$ qubits in the ancillary register, the maximum error in the estimated value of ϕ is $\delta_{max} = \frac{1}{2^{n+1}} \approx 0.02$. Consequently, the error in the chirality estimation is $\epsilon = 3\delta_{max} \approx 0.05$. The table summarizes the results obtained for the estimated eigenvalues using the enhanced QPE setup.	63

7	The table shows the results of the noiseless simulation of the cycle test (see Figure 25), for the chirality eigenstates as input. The estimation was obtained with $N_{shots} = 10,000$ trials. The error bounds for the chirality and chirality squared are $\epsilon_{\chi} = \frac{2}{\sqrt{3N_{shots}}} \approx 0.01$ and $\epsilon_{\chi^2} = \frac{2}{3} \frac{1}{\sqrt{N_{shots}}} \approx 0.007$, respectively.	66
8	The table presented below provides an overview of the resources needed for performing the chirality estimation. It compares the number of ancillary qubits, circuit depth, and the total number of gates. Specifically, the count of CNOT gates is explicitly displayed.	67
9	The table below compares the number of ancillary qubits and the number of shots N_{shots} required to obtain the chirality estimation with a bounded error of $\epsilon = 0.01$. For the QPE method, the number of shots is associated with a probability of obtaining the correct result in a single shot, and this probability is explicitly stated in the table.	69

Chapter 1

Introduction

Some real-world phenomena are difficult to study through observation or experimentation due to their rarity or the necessity of complex and sophisticated equipment. Therefore, a common approach is to study them through simulation, using more accessible resources. These simulations replicate the system's behavior, making its analysis possible. For instance, it is possible to simulate the launch of a spacecraft by modeling all the variables, such as gravitational forces, the propulsion system, atmospheric conditions, and so on, in order to predict and find the optimal launch trajectory to complete the mission. In this example, the necessity of simulation is clear as it provides a way to have confidence in the success and safety of the mission without spending resources or risking lives.

Similar to the previous example, simulating other aspects of physics helps us better understand our universe. Simulation can be seen as a tool to find answers to unresolved questions. Therefore, simulating quantum mechanics is very important due to its applications in fields such as materials science, high-energy physics, and quantum many-body problems [Daley et al. \[2022\]](#). This dissertation focuses on simulating quantum systems, which are systems where quantum phenomena cannot be neglected.

Quantum systems have the capability to exhibit a unique state called superposition, wherein they combine the properties of multiple classical states simultaneously [Daley et al. \[2022\]](#). This leads to the exponential growth of the Hilbert space, which is the space where the system is described. For example, if we consider a system composed of n quantum particles with two allowed states, the dimension of the Hilbert space for this system is 2^n . To simulate this system on a classical computer, which is based on transistors and stores classical information using bits, 2^n complex numbers would be needed to describe a complete superposition of the system. For a sufficient number of particles, a classical computer with the necessary resources does not exist. This limit is known as the classical limit and is reached for $n = 50$ particles, where $2^{50} \approx 10^{15}$ complex numbers would need to be stored. Additionally, for $n = 300$, the number of complex numbers needed to be stored exceeds the number of atoms in the visible universe [Lloyd \[1996\]](#), [Tacchino et al. \[2020\]](#), [Daley et al. \[2022\]](#).

As it is possible to see, simulating quantum systems is challenging, even impossible, for classical computers. The late Physics Nobel Prize laureate Richard Feynman was aware of this problem and, in a lecture in 1982, conjectured the possibility of having a suitable class of quantum machines that could mimic another quantum system. Thus, Feynman introduced the concept of a programmable quantum system, also known as a quantum computer. This approach allows us to overcome the problem of the enormous size of the Hilbert space, because the quantum computer is governed by the same rules of quantum mechanics as the desired system to simulate [Feynman \[1982\]](#).

Recalling the previous example of a system of n two-state particles, if the quantum computer is made up of particles with two allowed quantum states, called qubits for short, then the number of resources needed scales linearly with the scale of the system, just needing n qubits.

The importance of studying techniques for simulating quantum systems using the capabilities of quantum computers is evident, and this is the research field of the present work. Hence, the purpose of this introductory chapter is to provide a detailed explanation of the motivation behind the research goal and the significance of this master's thesis. Additionally, the final section outlines the structure of this document to guide readers and provide a comprehensive understanding of the content covered.

1.1 Motivation

In quantum mechanics, each physical system is governed by an operator known as the Hamiltonian, represented as H . The Hamiltonian encompasses the system's total energy, which includes its interactions, and it establishes the dynamical rules that the system must adhere to. Consequently, when considering a specific state of the system denoted by $\psi(t)$, which corresponds to a particular configuration of its constituent elements, the evolution of this state is determined by the system's Hamiltonian. The connection between these quantities is described by the Schrödinger Equation (SE) presented below [Sakurai and Commins \[1995\]](#), [Cottam and Haghshenasfard \[2020\]](#).

$$H\psi(t) = i\hbar\frac{\partial}{\partial t}\psi(t) \tag{1.1}$$

In this context, \hbar represents the Planck constant. The Schrödinger Equation (SE) is a differential equation discovered by Erwin Schrödinger, and it governs the dynamics of the wave function $\psi(t)$. However, in many practical scenarios, this equation can be transformed into a time-independent form where the operator H can be represented as a matrix, and accordingly, the wave function $\psi(t)$ can be expressed as a complex vector ψ . Consequently, in the time-independent Schrödinger Equation, the equation trans-

forms into an eigenvalue problem, where the eigenvalue represents the energy E of the system [Sakurai and Commins \[1995\]](#), [Cottam and Haghshenasfard \[2020\]](#).

$$H\psi = E\psi \tag{1.2}$$

Therefore, solving this problem involves two main steps. The first step is constructing the Hamiltonian and its matrix representations, which can be done straightforwardly using classical resources. Solving the eigenvalue problem in quantum systems is notably challenging, mainly due to the exponential growth of their Hilbert space with the number of particles (degrees of freedom) involved [Feynman \[1982\]](#), [Daley et al. \[2022\]](#). This requires substantial classical resources, which increase exponentially, as reflected in the size of the Hamiltonian matrix. This challenge is particularly significant for large-scale systems. As mentioned earlier, a potential solution is to employ quantum resources, which scale linearly with the system's size. This approach allows us to study larger systems beyond the classical limit by simulating another quantum system [Feynman \[1982\]](#), [Lloyd \[1996\]](#), [Daley et al. \[2022\]](#).

The process of using quantum resources to simulate desired quantum systems is referred to as quantum simulation [Lloyd \[1996\]](#), [Tacchino et al. \[2020\]](#), [Daley et al. \[2022\]](#). The primary approach to tackle this challenge involves leveraging Quantum Computers (QCs).

The standard paradigm for QCs is the digital quantum circuit model, where the basic unit of representation mimics the classical unit of information known as a bit. In analogy, the minimal unit of quantum information is called a qubit [Nielsen and Chuang \[2002\]](#). Just as classical digital circuits are implemented by utilizing a minimal set of gates to perform required operations, quantum digital circuits have their own set of quantum gates. These gates, similar to their classical counterparts, are employed in a circuit model to construct quantum algorithms [Nielsen and Chuang \[2002\]](#).

In digital QCs, there exists a group of gates known as universal set of quantum gates, which allows the implementation (or approximation with arbitrary accuracy) of any unitary operation [Nielsen and Chuang \[2002\]](#), [Childs \[2017\]](#). This set typically consists of one- and two-qubit operations. Thus, the process of simulating a quantum system using this type of architecture relies on implementing quantum circuits that approximate the desired unitary operations.

While it may seem intuitive to grasp the concept of simulating a physical configuration using another one, the actual implementation is not straightforward. Therefore, it is necessary to develop methods that enable the imitation of the target system and obtain relevant information from it. However, there is an additional constraint associated with the physical implementation of quantum simulators. These devices are governed by the rules of quantum mechanics and leverage its advantages, but they are also

subject to certain challenges. The primary issue is the "coherence" time, which represents the duration during which the computation remains accurate [Nielsen and Chuang \[2002\]](#), [Preskill \[2018\]](#). Beyond this time, noise predominantly affects the information due to interactions between the device and its environment, as well as within the device itself. John Preskill introduced the concept of Noisy Intermediate Scale Quantum (NISQ) technology to describe the currently available devices [Preskill \[2018\]](#). Consequently, when designing a quantum simulation, it is crucial to consider the method's performance in terms of utilizing the fewest possible resources, such as the number of quantum subsystems and the runtime.

Many intriguing problems nowadays lie in the study of quantum systems due to their vast range of applications. Consequently, it is imperative to find ways to investigate these physical configurations. However, the range of quantum systems is incredibly broad. Therefore, this thesis will specifically focus on one type of quantum system: spin systems. In simpler terms, a spin system refers to a collection of quantum systems that possess an intrinsic property known as spin, which will be explained in more detail later. For instance, an electron is a particle with charge and a spin of $1/2$ [Sakurai and Commins \[1995\]](#), [Parkinson and Farnell \[2010\]](#).

There is a class of materials referred to as insulators, which, as the name suggests, do not allow the flow of electric charge within the material. However, within the category of insulating materials, there is another class known as magnetic insulators. While these materials are electrically insulating, meaning the charge is constrained, they still exhibit a degree of freedom associated with spin [Wu and Hoffmann \[2013\]](#). The behavior of these materials is described in terms of the dynamics of the spin. This gives rise to spin models, which provide a framework for understanding their properties and interactions. Examples of spin models include: the Ising model, the Heisenberg model or the XY model [Parkinson and Farnell \[2010\]](#), [Pires \[2021\]](#). These models capture various aspects of spin interactions and have been widely studied in the field of condensed matter physics. The significance of studying this type of quantum entities arises from their diverse range of applications, particularly in the field of quantum magnetism, which aims to comprehend their magnetic properties [Parkinson and Farnell \[2010\]](#).

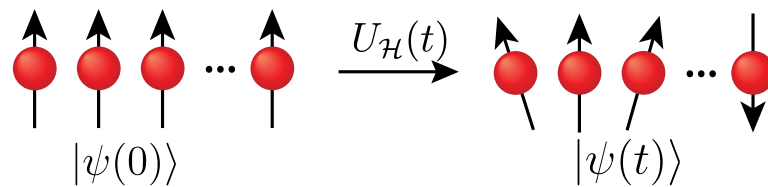
Therefore, the primary motivation behind this dissertation work is to make significant advancements in our understanding of utilizing the capabilities of Quantum Computers (QCs) for performing quantum simulations of relevant cases involving magnetic insulators.

1.2 Minimal Background

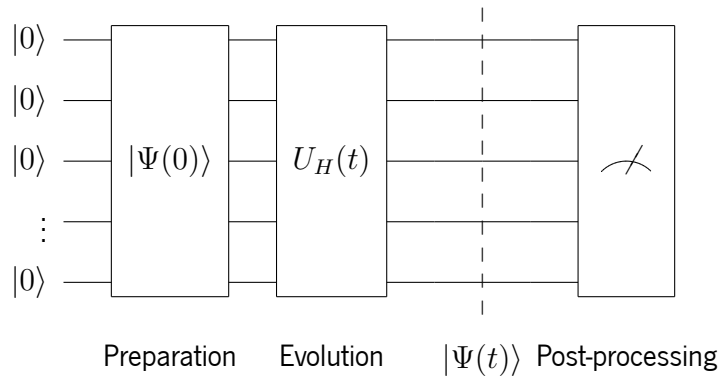
Since most of the necessary physics background for this work has been covered within the dissertation, this section aims to provide a concise introduction to some important concepts required to comprehend the objectives of this thesis. The purpose is to offer a brief overview and ensure that readers have the necessary foundation to grasp the goals and significance of the research presented in this thesis.

1.2.1 Quantum Simulation

The first concept to introduce is the general structure of a quantum simulation. As mentioned previously, a quantum simulation aims to replicate a desired natural quantum system, referred to as the target system, in another system known as the simulator (see Figure 1) Feynman [1982], Daley et al. [2022]. This process can be divided into three stages: preparation, evolution, and post-processing Daley et al. [2022].



(a) Target System



(b) Quantum Simulator

Figure 1: Schematic representation of the General Structure of a Quantum Simulation. Figure 1a depicts the target system, which represents the natural system under analysis. Figure 1b illustrates the mapping of the target system into the quantum simulator, along with the corresponding states of the simulation.

In the preparation stage, the simulator is initialized to match the initial state $|\psi(0)\rangle$ of the target system. This involves mapping the initial state of the target system onto the resources of the simulator $|\Psi(0)\rangle$. Next, in the evolution stage, the quantum state encoded in the simulator undergoes time evolution.

This evolution is governed by a unitary operator $U_H(t)$, which approximates the actual time evolution of the target system denoted by $U_{\mathcal{H}}(t)$ [Brown et al. \[2010\]](#), [Childs \[2017\]](#).

Once the evolution stage is completed, the simulator's state represents the final state of the target system $|\psi(t)\rangle$. To study the properties of this final state, specific measurements are performed. This post-processing stage involves conducting measurements on the simulator to extract relevant information about the target system [Nielsen and Chuang \[2002\]](#), [Childs \[2017\]](#).

Indeed, the post-processing stage of a quantum simulation depends on the specific questions we ask of the system. These questions are designed to extract the desired information about the system, and the results obtained provide insights into certain properties encoded in the final state of the simulation. In the framework of quantum mechanics, these questions are typically addressed by measuring physical observables, which represent measurable quantities in an experiment [Nielsen and Chuang \[2002\]](#). Examples of such observables include position, momentum, or spin [Sakurai and Commins \[1995\]](#). In the mathematical language of quantum mechanics, these observables are represented by operators, often in the form of matrices, as indicated in Equation 1.2 [Sakurai and Commins \[1995\]](#), [Cottam and Haghshenasfard \[2020\]](#).

Indeed, in the probabilistic framework of quantum mechanics, it is not meaningful to talk about a single, definite value when measuring an observable O . This is due to the inherent uncertainty associated with quantum systems. Each measurement of an observable on a general quantum state can yield different outcomes, each with a certain probability [Sakurai and Commins \[1995\]](#), [Kok \[2018\]](#). Therefore, what is more appropriate and physically meaningful in an experiment is the expectation value of the observable, denoted as $\langle O \rangle$. The expectation value represents the average value of the observable obtained by repeating the measurement many times [Kok \[2018\]](#). It is a real quantity that corresponds to a statistical average of the possible outcomes.

1.2.2 Classical Spin States

Another important concept to introduce is the notion of spin states. Spin models are used to describe systems where the spin is the only degree of freedom. Thus, the behavior of the system can be fully described in terms of the spin and its dynamics. To illustrate this concept, let's consider the Heisenberg model of two particles, which describes their interaction [Pires \[2021\]](#). The Hamiltonian for the Heisenberg model for spin- $\frac{1}{2}$ particles is given by:

$$H = -J\vec{S}_1 \cdot \vec{S}_2 \tag{1.3}$$

In this equation, J represents the exchange interaction, also known as the Heisenberg exchange, between the spins Pires [2021]. To better understand this concept, let's first work in the classical picture, where \vec{S}_1 and \vec{S}_2 are the classical spin vectors corresponding to the two particles. These spin vectors \vec{S}_1 and \vec{S}_2 can be thought of as arrows in three-dimensional space, representing the orientation and magnitude of the spins.

Therefore, in the classical picture, the Heisenberg Hamiltonian represents a real number that corresponds to the energy of the system, denoted as E_{class} . It can be expressed in terms of the angular difference θ between the two spin vectors of $S = \frac{1}{2}$ Parkinson and Farnell [2010].

$$\begin{aligned} E_{class}(\theta) &= -JS_1S_2 \cos(\theta) \\ &= -\frac{J}{4} \cos \theta \end{aligned} \tag{1.4}$$

The ground state of the system refers to the state configuration in which the energy of the system is minimized. In this particular example, we have two possible options: when $J > 0$, it corresponds to a ferromagnetic system, and when $J < 0$, it corresponds to an antiferromagnetic system Parkinson and Farnell [2010].

For the classical ferromagnetic case, the minimum energy is given by $E_{class}(\theta = 0) = -\frac{J}{4}$. In this case, the classical ferromagnetic ground state $|FGS\rangle_{class}$ corresponds to the particles' spin vectors pointing along the same direction, with an angular separation of $\theta = 0$. Choosing the favorable direction as \hat{z} , the product state which represents the ground state for the classical ferromagnetic model is given by the following equation, where $|\uparrow\rangle_i$ represents the particle i having its spin aligned with the \hat{z} direction:

$$|FGS\rangle_{class} = |\uparrow\rangle_1 \otimes |\uparrow\rangle_2 \tag{1.5}$$

In the classical antiferromagnetic case ($J < 0$), the state that minimizes its energy is given by $E_{class}(\theta = \pi) = -\frac{|J|}{4}$, where the ground state $|AGS\rangle_{class}$ has the spins pointing in opposite directions, i.e., $\theta = \pi$. By choosing the favorable direction as \hat{z} , where $|\uparrow\rangle_i$ represents a spin of particle i pointing up and $|\downarrow\rangle_i$ represents a spin pointing down, the ground state $|AGS\rangle_{class}$ can be written as the following product state:

$$|AGS\rangle_{class} = |\uparrow\rangle_1 \otimes |\downarrow\rangle_2 \tag{1.6}$$

1.2.3 Quantum treatment

To analyze the Heisenberg Hamiltonian of two spin- $\frac{1}{2}$ particles quantum mechanically, it is necessary to translate the language of the classical Hamiltonian in Equation 1.3 into the language of spin operators. A spin operator is a physical observable that quantifies the total spin projected in a specific direction Parkinson and Farnell [2010], Pires [2021]. In quantum mechanics, the spin vector \vec{S} can be represented in terms of spin vector operators with three components: \hat{x} , \hat{y} , and \hat{z} Sakurai and Commins [1995], Parkinson and Farnell [2010].

$$\begin{aligned}\vec{S} &= S_x \hat{x} + S_y \hat{y} + S_z \hat{z} \\ &= S \vec{\sigma}\end{aligned}\tag{1.7}$$

For the case of spin- $\frac{1}{2}$ particles, the spin operators can be defined in terms of the three-dimensional vector of Pauli operators, denoted by $\vec{\sigma} = (X, Y, Z)$. Specifically, the spin vector operators can be expressed as:

$$\begin{aligned}S_x &= \frac{1}{2} X = \frac{1}{2} \begin{pmatrix} 0 & 1 \\ 1 & 0 \end{pmatrix} \\ S_y &= \frac{1}{2} Y = \frac{1}{2} \begin{pmatrix} 0 & -i \\ i & 0 \end{pmatrix}, \\ S_z &= \frac{1}{2} Z = \frac{1}{2} \begin{pmatrix} 1 & 0 \\ 0 & -1 \end{pmatrix}\end{aligned}\tag{1.8}$$

Here, X , Y , and Z represent the Pauli matrices associated with the x , y , and z directions, respectively. Additionally, there are other spin operators such as the total spin operator S or the spin ladder operators S^\pm , which obey the commutation relations of the orbital angular momentum Parkinson and Farnell [2010]. However, these operators will not be discussed in this chapter and will be addressed in more detail in the Chapter 2.

Using these spin operators, we can apply a quantum treatment to the Heisenberg Hamiltonian for two particles Parkinson and Farnell [2010]. This involves solving the eigenvalue problem defined by the Hamiltonian H in order to determine the energy levels and the corresponding eigenstates of the system.

Since the goal of this section is to introduce concepts, the complete diagonalization of this system can

be found in the reference [Parkinson and Farnell \[2010\]](#). The equation below shows the eigenvalues and corresponding eigenstates of the system:

$$\begin{aligned}
 E &= -\frac{J}{4} \\
 |\psi_1\rangle &= |\uparrow\rangle_1 \otimes |\uparrow\rangle_2 \\
 |\psi_2\rangle &= \frac{|\uparrow\rangle_1 \otimes |\downarrow\rangle_1 + |\downarrow\rangle_1 \otimes |\uparrow\rangle_2}{\sqrt{2}}
 \end{aligned} \tag{1.9}$$

$$\begin{aligned}
 |\psi_3\rangle &= |\downarrow\rangle_1 \otimes |\downarrow\rangle_2 \\
 E &= \frac{3J}{4} \\
 |\psi_4\rangle &= \frac{|\uparrow\rangle_1 \otimes |\downarrow\rangle_2 - |\downarrow\rangle_1 \otimes |\uparrow\rangle_2}{\sqrt{2}}
 \end{aligned} \tag{1.10}$$

The eigenstates with energy $E = -\frac{J}{4}$ are degenerate and form a triplet (total spin $S = 1$), while the state with $E = \frac{3J}{4}$ is a singlet (total spin $S = 0$) that is not degenerate [Parkinson and Farnell \[2010\]](#). For the case in which the Hamiltonian has a ferromagnetic interaction ($J > 0$), the ground state has the same energy as the classical treatment, $E = -\frac{J}{4} = E_{\text{class}}$. However, in the quantum version, the ground state is given by the three eigenstates $|\psi_1\rangle$, $|\psi_2\rangle$, and $|\psi_3\rangle$, where $|\psi_1\rangle$ and $|\psi_3\rangle$ are similar to the classical case, meaning the spins are aligned along the same direction and can be described by a product state. However, the state $|\psi_2\rangle$ is not a product state and does not have a classical analogy. This new ferromagnetic ground state is an entangled state since it is not possible to describe it in terms of the two spin particles separately [Sakurai and Commins \[1995\]](#), [Parkinson and Farnell \[2010\]](#).

$$|FGS\rangle = \begin{cases} |\psi_1\rangle = |\uparrow\rangle_1 \otimes |\uparrow\rangle_2 \\ |\psi_2\rangle = \frac{1}{\sqrt{2}} (|\uparrow\rangle_1 \otimes |\downarrow\rangle_1 + |\downarrow\rangle_1 \otimes |\uparrow\rangle_2) \\ |\psi_3\rangle = |\downarrow\rangle_1 \otimes |\downarrow\rangle_2 \end{cases} \tag{1.11}$$

On the other hand, in the antiferromagnetic case ($J < 0$), the quantum effects become more prominent. The ground state is given by the singlet state $|\psi_4\rangle$ with energy $E = -\frac{3|J|}{4}$, which is much lower compared to the classical version.

Furthermore, the antiferromagnetic ground state is fundamentally different from the classical ground state. It does not have any analogy in classical physics. The ground state is an entangled state that arises from the quantum effects and cannot be described in terms of separate spin particles.

$$|AGS\rangle = \frac{|\uparrow\rangle_1 \otimes |\downarrow\rangle_2 - |\downarrow\rangle_1 \otimes |\uparrow\rangle_2}{\sqrt{2}} \tag{1.12}$$

1.2.4 Scalar Spin Chirality

Understanding quantum magnetic systems involves describing them by using spin models and characterizing the different types of spin states. To study these systems via simulation or experiments, as discussed in the quantum simulation subsection, it becomes crucial to evaluate the expectation values of specific observables. These observables provide information about the properties of the system and can be used to characterize its behavior.

In the realm of quantum magnetism, various types of observables play crucial roles. One important observable is the total magnetization, denoted as $\langle S_T^z \rangle \propto \sum_i \langle S_i^z \rangle$ Kim et al. [2023]. This quantity is determined by calculating the individual magnetization $\langle S_i^z \rangle$ of each particle i . The physical observable S_i^z represents the magnetization of spin i along the \hat{z} direction, which is a single-particle observable Kim et al. [2023].

There are other observables that involve more particles, such as the correlator $\langle S_i^z S_j^z \rangle$, which is an operator involving two particles that measures the correlation between the spins of particles i and j Cottam and Haghshenasfard [2020]. Furthermore, it is possible to define operators involving more than just two particles, allowing for the investigation of more complex interactions and patterns in the system.

Therefore, Wen et al. [1989] in 1989 introduced the concept of a three-particle operator called spin chirality $\hat{\chi}$. This operator can be written in terms of the previously introduced Pauli vector operators for each particle as follows:

$$\hat{\chi} = \vec{\sigma}_1 \cdot \vec{\sigma}_2 \times \vec{\sigma}_3 \quad (1.13)$$

This operator was proposed as a non-trivial order parameter that is relevant, for example, in classical magnetism to demonstrate the non-coplanarity of spin structures such as skyrmions Fert et al. [2017] and frustrated magnets Taguchi et al. [2001]. Skyrmions are topological magnetic objects used in solid-state physics, particularly in spintronics technology. Additionally, it has been shown that in the quantum description, this operator is appropriate for revealing these properties, albeit with a non-classical analogy Sotnikov et al. [2021]. Furthermore, certain system properties can lead to the emergence of a chiral spin liquid (CSL), which is of significance in the study of high-temperature superconductors Wen et al. [1989].

Hence, it is clear the motivation behind studying the chirality of a system. Nevertheless, synthesizing materials in-silico with these chiral properties can be a challenging task, even when the underlying models are well-established. To address this challenge, the utilization of quantum devices enables the simulation and exploration of such systems Tanamoto [2016].

Moreover, when this operator was introduced, the authors established some relations with pre-existing physical concepts. The most significant relation for this work is as follows: Consider a system with three spin- $\frac{1}{2}$ particles, and let the spins be transported around a loop through a cyclic permutation of the spins. This transformation will induce a phase change in the system, known as a Berry Phase [Wen et al. \[1989\]](#). Therefore, the difference between performing the transportation around the loop in one direction versus the opposite direction is related to the chirality of the system. Alternatively, in recent work, a quantum circuit was proposed to measure this type of geometrical phases [Oszmaniec et al. \[2021\]](#). The authors referred to this circuit as a cycle test, which served as motivation for the present work.

1.3 Objectives

The field of digital quantum simulation of chiral spin states focuses on two main areas of research: the development of chiral logic gates, which implement the chiral dynamics for preparing and simulating the behavior of chiral spin states [Ma et al. \[2017\]](#), [Wang et al. \[2019\]](#), and the advancement of measurement techniques for identifying these states [Sotnikov et al. \[2022\]](#), [Mazurenko et al. \[2023\]](#). This work specifically aims to contribute to the latter aspect, namely the development of measurement schemes to detect and characterize chiral spin states.

Traditionally, gaining insights into the system's chirality would involve complete measurement, known as quantum tomography [D'Ariano and Presti \[2001\]](#). However, this approach comes with drawbacks as it measures all the qubits where the state is encoded. Furthermore, this approach requires measuring an orthonormal set of operators called quorums [D'Ariano and Presti \[2001\]](#), where the chirality operator is expressed as a linear combination.

An alternative approach, proposed by [Sotnikov et al.](#), offers a hardware-efficient method to detect phase transitions related to changes in scalar spin chirality. This approach involves measuring the system in two or more randomly chosen single-qubit bases and analyzing the outcomes to probe inter-scale dissimilarities.

However, even though the approach proposed by [Sotnikov et al.](#) relies on direct measurements of the system, the main objective of this dissertation work is to explore a physically motivated strategy for computing the expectation value of the scalar spin chirality. The focus of this thesis is to discover an efficient quantum circuit that enables the measurement of the scalar spin chirality using indirect measurement approaches [Mitarai and Fujii \[2019\]](#).

In addition, as mentioned in the previous section, the chirality of a system is related to the differences in geometric phases, which can be measured using the cycle test method proposed by [Oszmaniec et al.](#)

[2021]. An objective of this work is to explore the potential of utilizing the cycle test method to estimate the chirality of a given system.

In order to achieve the research objectives, several training objectives needed to be fulfilled. Firstly, it was crucial to develop a comprehensive understanding of the basic theory of quantum magnetism, including the description of spin operators and various spin models. This involved an in-depth study of relevant literature to become familiar with the theoretical frameworks and the underlying methods in quantum mechanics. Key topics included the description, construction, diagonalization, and classical simulation of quantum models expressed in terms of spin operators. By acquiring proficiency in these fundamental concepts, a solid foundation was established for investigating the physics underlying scalar spin chirality.

Furthermore, expertise in quantum circuit design and quantum simulation was indispensable for exploring and refining the intended measurement strategies. This entailed acquiring knowledge of various quantum gates, quantum algorithms, and tools for quantum simulation.

As it will be necessary to choose the best approach to estimate the scalar spin chirality a comparative analysis will be conducted to assess the advantages and disadvantages of different approaches in terms of required quantum resources, with the aim of identifying the most suitable method for NISQ (Noisy Intermediate-Scale Quantum) computers. Once the optimal algorithm is determined, its effectiveness will be validated by applying it to calculate the chirality of diverse spin systems. By undertaking this research, the aim is to contribute to the advancement of efficient techniques for measuring the chirality of spin systems, thereby overcoming the existing limitations of current quantum methodologies.

1.4 Outline of the Document

This dissertation comprises seven chapters. The first chapter, which serves as the introduction to this work, has already been presented. Chapter 2 delves deeper into the thesis's background and methodology. Chapters 3 through 5 present the results and the process of acquiring them. The final chapter, chapter 6, provides a summary of the work, draws conclusions, and outlines future research possibilities. In the following text, each chapter will be briefly explained.

Chapter 2 provides the foundational theoretical background for this dissertation, introducing key concepts such as quantum simulation, digital quantum computation, quantum circuit components, quantum algorithms, and quantum mechanics in the context of quantum magnetism. This chapter also presents the state-of-the-art in the field, serving as the foundation for our research.

The methodology section 2.7 outlines the research methods used in this dissertation. It introduces Python as the primary programming language and discusses its importance in scientific computing. The section focuses on two main methodologies: analytical calculations and computer-assisted simulations. Analytical calculations provide theoretical insights into proposed quantum circuits, while simulations are vital for empirical testing.

The Chirality Eigenstate Preparation Chapter 3 focuses on the initial phase of quantum simulation, where we prepare the initial state, specifically the eigenstates of the chirality operator, and discuss their implementation in quantum computers.

Then, Chapter 4 builds on the quantum algorithms introduced in the theoretical background (Chapter 2). We apply quantum circuits to propose and test various indirect methods for measuring chirality within a given state, with a focus on finding the most effective approach in the era of Noisy Intermediate-Scale Quantum (NISQ) computing.

Chapter 5 utilizes the most promising NISQ method developed in the previous chapter to indirectly measure the chirality of various systems. This includes classical magnetic states represented by separable coherent spin states, spin-wave models, and spin spirals. Finally, Chapter 6 summarizes the conclusions drawn from our research and outlines potential directions for future work and research in the field.

Chapter 2

Theoretical Background and Methodology

In the introduction of this dissertation, key concepts were introduced to provide an initial understanding of the thesis and its significance. This chapter serves to further elucidate the theoretical foundation upon which the outcomes of this project are built. This chapter will delve into several crucial topics, including quantum simulation utilizing quantum computers as simulators, the current state-of-the-art of quantum algorithms, Hamiltonians for spin systems, the concept of scalar spin chirality, and the forefront of quantum simulation concerning these specific types of systems.

2.1 Quantum Simulation

As discussed in the previous chapter, simulating quantum systems is a challenging task for classical computers due to the rapid increase in the Hilbert space as the system size grows. For classical computers, this task becomes practically impossible when using greedy algorithms to simulate such systems, like attempting to simulate all interactions and store the complete information of the wave function. Even with more complex classical algorithms, for sufficiently large systems, the required amount of resources becomes unfeasible [Feynman \[1982\]](#), [Lloyd \[1996\]](#), [Daley et al. \[2022\]](#). Consequently, a solution was proposed by Richard Feynman in the early 1980s. This solution involves using one quantum system (referred to as a *simulator*) to simulate another *target* quantum system [Feynman \[1982\]](#).

2.1.1 Analog and Digital Quantum Simulators

In quantum simulation, there are two main classes based on the type of simulator used: analog quantum simulators (AQS) and digital quantum simulators (DQS). Both approaches share the fundamental idea of emulating a quantum system of interest using another quantum system. To differentiate between the two, consider a target quantum system governed by the Hamiltonian \mathcal{H} , which encodes its dynamics and interactions. The target system evolves from an initial configuration $|\psi(0)\rangle$ to a final state $|\psi(t)\rangle$ over a

time t under the time evolution operator $U_{\mathcal{H}}(t)$ Daley et al. [2022].

The key distinction between the two approaches lies in their methods. An analog quantum simulator aims to replicate the dynamics and interactions of the target system. In this case, the simulator's Hamiltonian H approximates the target Hamiltonian \mathcal{H} ($H \approx \mathcal{H}$). Conversely, a digital quantum simulator seeks to approximate the system's dynamics. Here, the unitary time evolution of the simulator approximates that of the target system ($U_H(t) \approx U_{\mathcal{H}}(t)$) Daley et al. [2022].

Both approaches have their own set of advantages and disadvantages. Analog Quantum Simulators (AQS) offer benefits for specific many-body problems, leveraging particular types of quantum platforms that yield good outcomes when used to emulate the target system. For example, trapped ions are well-suited for studying interacting spin systems Monroe et al. [2021], superconducting circuits excel at investigating various interactions like strong photon-photon interactions Wilkinson and Hartmann [2020], and cold atoms are employed to simulate condensed matter systems Henriot et al. [2020]. Flannigan et al. [2022]'s analysis indicates that the first practical instance of quantum advantage in simulation can be achieved through special-purpose analog devices enabling direct model implementation. However, an inherent drawback of AQS is its limited generality. This limitation stems from the fact that AQS are confined to replicating only the types of interactions that the simulator is capable of emulating Daley et al. [2022]. As a result, AQS may not provide a comprehensive solution to a wide range of problems.

Therefore, the DQS aims to be a general-purpose quantum simulator by approximating unitary operations, rather than replicating specific interactions. This is accomplished through the use of digital quantum computers (DQC) which employ a universal set of quantum operations or gates Tacchino et al. [2020], Daley et al. [2022]. This gate set allows for the approximate representation of any unitary operation, enabling DQS to simulate a wide range of quantum systems. However, a significant challenge arises with this approach. To solve any quantum system accurately, a fault-tolerant DQC is required. This implies that the quantum computer can perform computations even in the presence of errors Daley et al. [2022]. Unfortunately, such fault-tolerant DQCs are not currently available. As Preskill [2018] has noted, our current state of quantum computing is characterized by Noisy Intermediate Scale Quantum (NISQ) devices. These devices have limitations in terms of coherent computation time and susceptibility to environmental noise, which restricts the scope of applications that can be effectively handled.

However, it is important to highlight that even within the NISQ regime, there exists a variety of applications where these devices can provide valuable outcomes across different domains. For instance, recent work by Kim et al. [2023] demonstrated the measurement of precise expectation values for circuit volumes exceeding the capabilities of brute-force classical computation. This showcases the practical utility

of quantum computing even in the absence of fault-tolerant capabilities. These achievements are made possible through the application of various error mitigation techniques that are particularly relevant when using real quantum devices. Although this work does not delve into the specifics of these error mitigation algorithms, for further details, please refer to the original paper by [Kim et al. \[2023\]](#).

This work will specifically concentrate on the Digital Quantum Simulation (DQS) case, and the upcoming sections will introduce quantum circuits falling within the realm of Digital Quantum Computing (DQC).

2.1.2 Designing a Quantum Simulation

The process of simulating a quantum system using a quantum simulator can be broken down into three primary stages: preparation, evolution, and post-processing. These stages are fundamental to quantum simulation, regardless of the specific type of quantum simulator employed. The subsequent discussion will delve into each of these stages in greater detail.

Preparation

In the first stage of quantum simulation, qubits are prepared to be in the desired initial state, often corresponding to the system's ground state. This involves defining the basis states of the target system and determining how this information will be encoded within the quantum computer. For instance, representing a single spin- $\frac{1}{2}$ particle in a qubit is straightforward due to its inherent qubit nature. Additionally, for encoding fermions¹, the Fock space representation is commonly employed. In this representation, each qubit signifies an occupation basis state, either $|1\rangle$ (occupied) or $|0\rangle$ (unoccupied) [Claudio \[2022\]](#). Subsequently, the quantum algorithm for preparation establishes the initial computational configuration.

Several algorithms are available for preparing the initial state of a quantum system for simulation. One such method is the Quantum Phase Estimation (QPE) algorithm, which estimates the eigenvalues of a unitary operator U by iteratively applying it [Kitaev \[1995\]](#). This technique will be further elucidated in the upcoming section [2.3](#) on quantum algorithms. Additionally, QPE can be leveraged to prepare a desired eigenstate of the same unitary operator U , as measurement of the eigenvalue causes the input state to collapse into the associated eigenstate [Murta et al. \[2023\]](#).

Another example is the Variational Quantum Eigensolver (VQE), which employs variational techniques to approximate the ground state of a given Hamiltonian by minimizing the measured energy [Peruzzo](#)

¹ Fermions adhere to Fermi-Dirac statistics, which dictate that a collection of N identical fermions is entirely antisymmetrical when any pair is interchanged. Moreover, fermions possess half-integer spin and adhere to the Pauli exclusion principle, much like electrons [Sakurai and Commins \[1995\]](#).

et al. [2014], McArdle et al. [2019]. A different approach is outlined in Carbone et al. [2022], where a recursive method for constructing total spin eigenfunctions through variational means is demonstrated. Furthermore, Murta and Fernández-Rossier [2021] introduces algorithms for encoding the Gutzwiller wave function, while Murta et al. [2023] suggests techniques for encoding Valence-Bond solid states on NISQ devices. Ultimately, the choice of a specific circuit may hinge upon the particular problem under consideration and the desired outcomes.

Evolution

While certain quantum simulation algorithms might focus exclusively on the initial state preparation of a system, others extend to encompass the state's evolution based on a provided Hamiltonian. The manner in which the model is represented on a quantum computer, along with the corresponding quantum operations, depends on the chosen basis state representation. For instance, consider a scenario as depicted in Anselme Martin et al. [2022], where the Hamiltonian is described using fermionic operators. In such cases, it might be necessary to convert it into Pauli operators through techniques like the Jordan-Wigner or Bravyi-Kitaev transformations Bauer et al. [2020]. Various alternative approaches are also available for achieving this objective.

The target Hamiltonian \mathcal{H} for quantum simulation is often represented as a sum of local interactions $\mathcal{H} = \sum_j h_j$, and the system's unitary evolution is achieved through exponentiating this operator, $U_{\mathcal{H}}(t) = e^{-i\mathcal{H}t}$. When the local interactions commute, the overall time evolution operator can be readily decomposed into a sequence of local time evolution operators, $U_{\mathcal{H}}(t) = \prod_j e^{-ih_j t}$. However, in many scenarios, these local interactions do not commute, which requires the use of techniques like Trotterization to approximate the total evolution operator Claudino [2022] or employing the Linear Combination of Unitaries (LCU) method Childs and Wiebe [2012]. These methods will be elaborated upon in more detail in Section 2.3. Once this unitary operation has been transformed into permissible gate operations, a quantum computer can employ it to simulate the evolution of the system.

Post-processing

The final stage of a quantum simulation involves extracting information about the system's ultimate state, such as expectation values for specific observables Childs [2017]. It's important to emphasize that in a quantum computer, only the qubits are subjected to measurement, and this process merely discloses the computational basis² state to which the qubit has collapsed Nielsen and Chuang [2002]. Consequently,

² The eigenstates of the Z (Pauli Z) operator, represented by $|0\rangle$ and $|1\rangle$, are commonly referred to as the computational basis states.

it might be necessary to repeat the simulation numerous times and analyze the resulting data statistically.

For measuring expectation values, we apply operators and process the acquired data. A common technique for obtaining operator expectation values is Hamiltonian averaging. This method entails repeating measurements while altering the basis depending on the specific Pauli operator being measured for each qubit [McClellan et al. \[2014\]](#). Additionally, tomography techniques can be employed to gain deeper insights into the simulated system, employing a similar approach [Cheng and Lou \[2020\]](#).

The mentioned techniques correspond to direct measurement approaches, and an exhaustive characterization of the output state is typically justified when multiple expectation values need to be computed. However, there are alternative methods that involve indirect measurements, which may be more suitable in certain cases than the commonly used direct measurement techniques. The main advantage of these indirect measurement techniques is that they only measure the specific information of interest, making them more compatible with NISQ devices. A notable example of such an indirect measurement procedure is the Hadamard test [Cleve et al. \[1998\]](#), which employs a single ancillary qubit. Quantum phase estimation (QPE) extends this concept to multiple ancillary qubits [Kitaev \[1995\]](#), [Nielsen and Chuang \[2002\]](#).

2.2 Digital Quantum Computers

As previously mentioned, digital quantum computers (DQC) aim to be general-purpose quantum computers. They achieve this by employing a collection of quantum operations that form a universal set, regardless of the particular quantum hardware in use. This universal set of gates allows for the simulation of a wide range of quantum systems [Daley et al. \[2022\]](#). The universal set of gates is defined to approximate any unitary operator U with an arbitrary error ε using a sequence of n gates U_i from the universal set [Nielsen and Chuang \[2002\]](#). This error is defined in the equation below:

$$\left\| U - \prod_{i=1}^n U_i \right\| < \varepsilon \quad (2.1)$$

where $\|A\| \equiv \max_{|\psi\rangle} \frac{|A|\psi\rangle|}{\|\psi\rangle}$ is the spectral norm of the matrix A , defined as the maximum absolute eigenvalue of A and $\|\psi\rangle| = \sqrt{\langle\psi|\psi\rangle}$ [Horn and Johnson \[1990\]](#). In general, a universal set of quantum operations must include the ability to implement a general single-qubit operation, often represented by the U_3 gate (as shown in Equation 2.2), and a two-qubit gate such as the controlled-not (CNOT) gate (see Table 1) [Barenco et al. \[1995\]](#). However, this is not the only universal set. For instance, the Clifford group (generated by the CNOT gate, Hadamard gate H , and S gate) along with the T gate (see Table 1) also forms a universal set [Carignan-Dugas et al. \[2015\]](#).

$$U_3(\theta, \phi, \lambda) = \begin{pmatrix} \cos \frac{\theta}{2} & -e^{i\lambda} \sin \frac{\theta}{2} \\ e^{i\phi} \sin \frac{\theta}{2} & e^{i(\phi+\lambda)} \cos \frac{\theta}{2} \end{pmatrix} \quad (2.2)$$

Since the focus of this work does not involve the specifics of how DQC implements the set of quantum gates, we will employ the commonly used set of quantum operations (see Table 1). Their names and matrix notations are presented below. Additionally, when constructing a quantum algorithm, a circuit notation is often used, where quantum operations are depicted as boxes arranged in horizontal lines. The sequence of operations proceeds from left to right, representing the order of operations over time [Feynman \[1985\]](#), [Nielsen and Chuang \[2002\]](#).

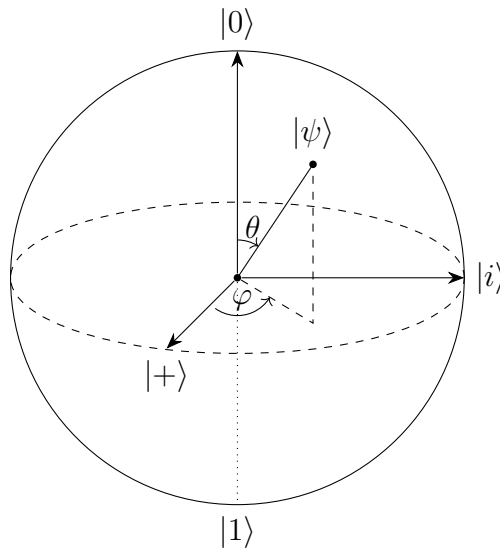
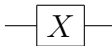
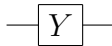
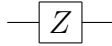
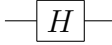
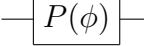
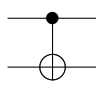
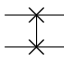


Figure 2: The figure illustrates a general pure state $|\psi\rangle$ defined by the azimuthal angle θ and the polar angle φ . The azimuthal angle provides us with the amplitudes of the state $|0\rangle$ and $|1\rangle$, while the polar angle represents the complex phase between the computational basis states $|0\rangle$ and $|1\rangle$. The state $|+\rangle$ corresponds to the eigenstate with a positive eigenvalue of the Pauli- X operator and can be described by $\theta = \frac{\pi}{2}$ and $\varphi = 0$. Similarly, the state $|i\rangle$ is the eigenstate with a positive eigenvalue of the Pauli- Y operator and is characterized by $\theta = \frac{\pi}{2}$ and $\varphi = \frac{\pi}{2}$.

Table 1: Common Quantum Gates and Their Representations. There are specific cases for the phase gate $P(\phi)$, namely: $P\left(\frac{\pi}{2}\right)$ corresponds to the S gate, and a phase of $\phi = \frac{\pi}{4}$ gives the T gate.

Gate	Circuit Notation	Matrix Notation
Pauli-X (X)		$\begin{pmatrix} 0 & 1 \\ 1 & 0 \end{pmatrix}$
Pauli-Y (Y)		$\begin{pmatrix} 0 & -i \\ i & 0 \end{pmatrix}$
Pauli-Z (Z)		$\begin{pmatrix} 1 & 0 \\ 0 & -1 \end{pmatrix}$
Hadamard (H)		$\frac{1}{\sqrt{2}} \begin{pmatrix} 1 & 1 \\ 1 & -1 \end{pmatrix}$
Phase ($P(\phi)$)		$\begin{pmatrix} 1 & 0 \\ 0 & e^{i\phi} \end{pmatrix}$
$CNOT$		$\begin{pmatrix} 1 & 0 & 0 & 0 \\ 0 & 1 & 0 & 0 \\ 0 & 0 & 0 & 1 \\ 0 & 0 & 1 & 0 \end{pmatrix}$
$SWAP$		$\begin{pmatrix} 1 & 0 & 0 & 0 \\ 0 & 0 & 1 & 0 \\ 0 & 1 & 0 & 0 \\ 0 & 0 & 0 & 1 \end{pmatrix}$

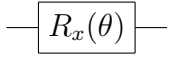
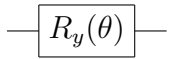
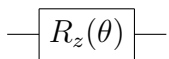
Moreover, it is possible to control single-qubit operations by representing a qubit's pure state in terms of the Bloch sphere [Kok \[2018\]](#). A qubit's state $|\psi\rangle$ can be depicted on the Bloch sphere, as illustrated in [Figure 2](#), and is represented by

$$|\psi\rangle = \cos\frac{\theta}{2}|0\rangle + e^{i\varphi}\sin\frac{\theta}{2}|1\rangle \quad (2.3)$$

Therefore, any single-qubit operation can be decomposed into single-qubit rotations along each axis.

This gives us the three possible rotations $R_\alpha(\theta) = e^{-i\frac{\theta}{2}\sigma_\alpha}$ for $\alpha \in \{x, y, z\}$, where σ_α corresponds to the Pauli- α operator [Nielsen and Chuang \[2002\]](#). These operations can be found in the table 2.

Table 2: Single-Qubit Rotation Gates

Rotation	Circuit Notation	Matrix Notation
$R_x(\theta)$		$\begin{pmatrix} \cos \frac{\theta}{2} & -i \sin \frac{\theta}{2} \\ -i \sin \frac{\theta}{2} & \cos \frac{\theta}{2} \end{pmatrix}$
$R_y(\theta)$		$\begin{pmatrix} \cos \frac{\theta}{2} & -\sin \frac{\theta}{2} \\ \sin \frac{\theta}{2} & \cos \frac{\theta}{2} \end{pmatrix}$
$R_z(\theta)$		$\begin{pmatrix} e^{-i\frac{\theta}{2}} & 0 \\ 0 & e^{i\frac{\theta}{2}} \end{pmatrix}$

2.3 Quantum Circuits and Techniques

With the concept of quantum simulation and digital quantum computers introduced, this section now delves into the presentation of several cutting-edge quantum circuits and techniques, which are highly relevant to the focus of this dissertation on implementing quantum digital simulation. These quantum circuits hold significant importance for the context of this dissertation.

2.3.1 Lie-Trotter-Suzuki Formula

The exponentiation of the sum of two operators, A and B , that do not commute $[A, B] \neq 0$ cannot be exactly decomposed as the product of the individual exponentiations of these operators. However, this exponentiation can be decomposed using the following relation.

$$e^{(A+B)} = \lim_{n \rightarrow \infty} \left(e^{\frac{A}{n}} e^{\frac{B}{n}} \right)^n \quad (2.4)$$

This is a product formula named after [Trotter \[1959\]](#) and is widely used for approximating the exponentiation of operators. With this formula, it becomes possible to exponentiate an operator H composed of sums of other operators, given by $H = \sum_j h_j$, using n products of individual exponentials $e^{h_j/n}$, where n is a finite integer. This approximation has a bounded error of $\mathcal{O}(1/n)$. Therefore, the first-order Trotter-Suzuki formula for approximating the exponential e^{iHt} , where $t \in \mathbb{R}$, is provided below [Trotter \[1959\]](#),

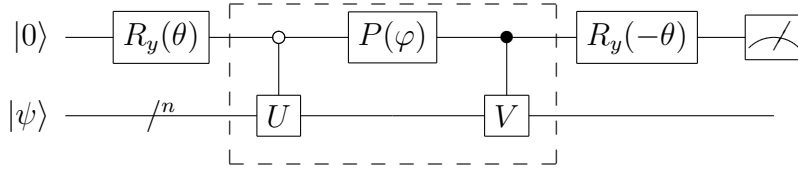


Figure 3: LCU algorithm for a linear combination of two unitary operators U and V . The dashed box represents the implementation of the operator \mathcal{O}_S , which combines the unitaries U and V . The operator $P(\varphi)$ is a phase gate that adds the phase φ required in the weight of the operator V .

Suzuki [1993].

$$e^{iHt} \approx \left(\prod_j e^{ih_j t/n} \right)^n + \mathcal{O}(1/n) \quad (2.5)$$

In quantum computing, Hamiltonians are typically decomposed into linear combinations of Pauli strings Nielsen and Chuang [2002]. By applying the Trotter-Suzuki formula, it becomes possible to approximate the evolution governed by such Hamiltonians with arbitrary accuracy Trotter [1959]. However, it is important to note that the number of layers of trotterization is limited by the capabilities of the current NISQ devices.

2.3.2 Linear Combination of Unitaries (LCU)

The LCU method was introduced as a means to simulate Hamiltonian dynamics and provide an alternative approach to the conventional method based on products of unitary operations, such as the Lie-Trotter-Suzuki formulas (see Subsection 2.3.1). The LCU method is a non-deterministic algorithm that facilitates the implementation of addition and subtraction operations on unitaries, as the name suggests Childs and Wiebe [2012]. Before generalizing this algorithm, let's consider a simple case where a non-unitary operator A can be expressed as a linear superposition of two unitary operators U and V with different weights (see Equation 2.6). In order to implement this linear combination, an ancillary qubit is introduced, expanding the Hilbert space. The operations are then applied in a specific manner such that the non-unitary operator A becomes part of a higher-dimensional unitary operator. It is important to note that both U and V are unitary operators of dimension 2^n , and with the addition of the ancillary qubit, the resulting dimension expands to 2^{n+1} . The main objective of the algorithm is to apply the operator A to a given n -qubit state, denoted as $|\psi\rangle$. The LCU algorithm, which implements these operations is depicted in Figure 3.

$$A = \alpha U + \beta e^{i\varphi} V, \quad \alpha, \beta \in \mathbb{R}^+ \quad (2.6)$$

Equation 2.7 represents the final state of the algorithm presented in Figure 3. The value of θ can be easily determined by utilizing the relations $\cos^2 \theta = \alpha/\Delta$ and $\sin^2 \theta = \beta/\Delta$, where $\Delta = \alpha + \beta$. Note that the weight of the operator V includes a complex term with a phase φ , which corresponds to the phase applied in the LCU algorithm. An interesting case arises when $\varphi = \pi$, as it results in the algorithm performing a subtraction of the operators.

$$\begin{aligned}
|0\rangle \otimes |\psi\rangle &\xrightarrow{R_y(\theta)} \cos \theta |0\rangle |\psi\rangle + \sin \theta |1\rangle |\psi\rangle \\
&\xrightarrow{\mathcal{O}_s} \cos \theta |0\rangle \otimes U |\psi\rangle + e^{i\varphi} \sin \theta |1\rangle \otimes V |\psi\rangle \\
&\xrightarrow{R_y(-\theta)} |0\rangle \otimes (\cos^2 \theta U + e^{i\varphi} \sin^2 \theta V) |\psi\rangle - \sin \theta \cos \theta |1\rangle \otimes (U - e^{i\varphi} V) |\psi\rangle
\end{aligned} \tag{2.7}$$

It is evident that when the ancillary register is measured in the state $|0\rangle$, the linear combination of unitaries that constructs the non-unitary operator A has been applied to the state $|\psi\rangle$. However, due to the inherent uncertainty in the measurement of the ancilla, the method is non-deterministic. Consequently, the probability of accurately applying the correct operator can be seen in Equation 2.8.

$$\begin{aligned}
P_{\text{correct}} = p_0 &= \langle \psi | (\cos^2 \theta U + e^{i\varphi} \sin^2 \theta V)^\dagger (\cos^2 \theta U + e^{i\varphi} \sin^2 \theta V) | \psi \rangle \\
&= \frac{1}{\Delta^2} \langle \psi | (\alpha U + e^{i\varphi} \beta V)^\dagger (\alpha U + e^{i\varphi} \beta V) | \psi \rangle \\
&= \frac{1}{\Delta^2} \langle \psi | A^\dagger A | \psi \rangle
\end{aligned} \tag{2.8}$$

Essentially, if a non-unitary operator A can be expressed as a linear combination of 2^m unitary operators $A = \sum_{i=0}^{2^m-1} \alpha_i V_i$, the LCU method provides a way to apply this operator to a given n -qubit state $|\psi\rangle$. This generalized version involves an ancillary register of m qubits, and the steps to apply the operator A are as follows and summarized in the Figure 4:

1. Prepare the initial state $|\alpha\rangle$ of the ancillary register by applying the preparation operator \mathcal{O}_p .

$$|\alpha\rangle \equiv \frac{1}{\sqrt{\Delta}} \sum_{i=0}^{2^m-1} \sqrt{|\alpha_i|} |i\rangle, \quad \Delta \equiv \sum_{i=0}^{2^m-1} |\alpha_i| \tag{2.9}$$

2. Apply the \mathcal{O}_s operator, which is a controlled version of the unitary operators V_i applied to the state $|\psi\rangle$ using the controlled states $|i\rangle$ on the ancillary register. The α_i are complex values, and as shown in the previous example, in this step, the phases $e^{i\varphi_i}$ are applied.

$$\mathcal{O}_s |\alpha\rangle \otimes |\psi\rangle = \frac{1}{\sqrt{\Delta}} \sum_{i=0}^{2^m-1} e^{i\varphi_i} \sqrt{|\alpha_i|} |i\rangle \otimes V_i |\psi\rangle \tag{2.10}$$

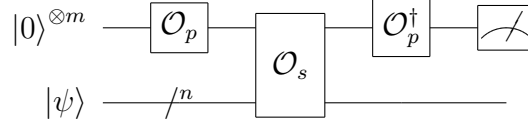


Figure 4: LCU algorithm for a linear combination of two unitary operators U and V

3. Apply the O_p^\dagger operator to obtain the final state of the algorithm. As in the previous example, a successful application of the operator A on the main register corresponds to measuring the ancillary register in the state $|0\rangle^{\otimes m}$. The probability of success can be calculated as:

$$p_{00\dots 0} = \frac{1}{\Delta^2} \langle \psi | A^\dagger A | \psi \rangle \quad (2.11)$$

However, it is worth noting that implementing controlled operations for arbitrary control states can be challenging in real quantum devices. As an alternative, when applying the LCU method to an arbitrary operator A decomposed as a linear combination of M unitary operators, we can use M ancillas instead of $\log_2 M$. In this modified approach, the control states are chosen as $|2^i\rangle$ to correspond to the i -th operator. Although this method requires more qubits, it simplifies the implementation of the control operations, as it only requires a simpler control operation with the control qubit. This approach was utilized by [Murta et al. \[2023\]](#) and can be explored in more detail in their research.

2.3.3 Quantum Fourier Transform (QFT)

The Quantum Fourier Transform (QFT) is a quantum algorithm that, as its name suggests, performs the Fourier transform on a given quantum state [Coppersmith \[2002\]](#), [Nielsen and Chuang \[2002\]](#). This algorithm is inspired by the classical discrete Fourier transform (DFT), which transforms a vector of N complex numbers $[x_0, \dots, x_{N-1}]$ into its Fourier representation in another vector of N complex numbers $[y_0, \dots, y_{N-1}]$. Each component y_k of the transformed vector is defined as follows:

$$y_k \equiv \frac{1}{\sqrt{N}} \sum_{j=0}^{N-1} \exp \left\{ i \frac{2\pi k j}{N} \right\} x_j \quad (2.12)$$

Therefore, in a similar way, the QFT transforms a computational basis state labeled as $|j\rangle$, $j \in \mathbb{Z}^+$ into the following Fourier representation:

$$|j\rangle \xrightarrow{QFT} \frac{1}{\sqrt{N}} \sum_{k=0}^{N-1} \exp \left\{ i \frac{2\pi j k}{N} \right\} |k\rangle \quad (2.13)$$

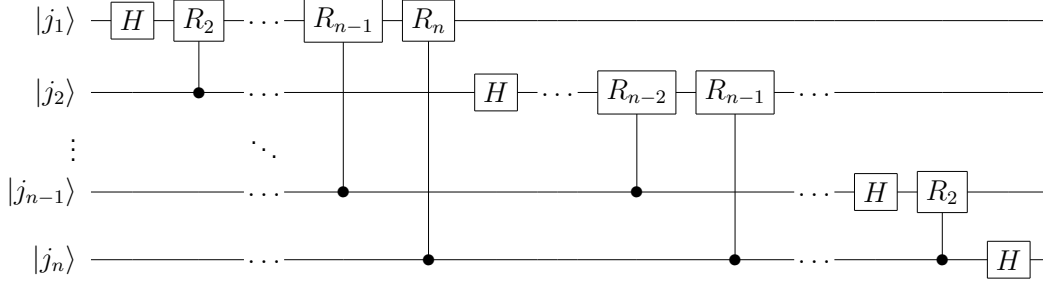


Figure 5: The figure illustrates the circuit implementation of the Quantum Fourier Transform (QFT) for an input state $|j\rangle$. It is important to note that the resulting product state at the end of the circuit is in reverse order compared to Equation 2.14. This reversal can be addressed by incorporating swap gates or by considering the reversed order when applying the circuit.

An integer j encoded in an n -bit string as $j \equiv j_1 2^{n-1} + j_2 2^{n-2} + \dots + j_n 2^0$ can be represented by a quantum state with n qubits $|j_1 \dots j_n\rangle$. When this state is changed by the Quantum Fourier Transform (QFT), it is taken to the Fourier representation shown in the equation 2.13. By performing straightforward calculations, it can be observed that the QFT transforms the $|j\rangle$ state into a product state in the following representation:

$$\begin{aligned}
 |j_1 \dots j_n\rangle &\xrightarrow{QFT} \frac{1}{2^n} \sum_{k_1=0}^1 \dots \sum_{k_n=0}^1 \bigotimes_{l=1}^n e^{i2\pi j 2^{-l} k_l} |k_l\rangle \\
 &= \bigotimes_{l=1}^n \frac{|0\rangle + e^{i2\pi j 2^{-l}} |1\rangle}{2} \\
 &= \frac{(|0\rangle + e^{i2\pi 0 \cdot j_n} |1\rangle) \otimes (|0\rangle + e^{i2\pi 0 \cdot j_{n-1} j_n} |1\rangle) \otimes \dots \otimes (|0\rangle + e^{i2\pi 0 \cdot j_1 \dots j_n} |1\rangle)}{2^n}
 \end{aligned} \tag{2.14}$$

The transformed state is represented as a product state, where each term contains a binary fraction represented as $0.j_l \dots j_m$, corresponding to the value $j_l 2^{-1} + \dots + j_m 2^{-(m-l+1)}$. The circuit implementing this unitary transformation can be constructed using Hadamard gates and controlled R_k transformations, where R_k adds a phase of $\exp\{i\frac{2\pi}{2^k}\}$ to the qubit (see Figure). For a more detailed explanation of this algorithm, please refer to Nielsen and Chuang [2002].

2.3.4 The Hadamard Test

The Hadamard Test is a quantum algorithm that aims to estimate the phase or the expectation value of a given unitary operator on a quantum state. It is a specific case of the more general quantum phase estimation algorithm (see Subsection 2.3.5 Cleve et al. [1998], Aharonov et al. [2006]). The Hadamard Test algorithm involves a main register that encodes the quantum state of interest, denoted as $|\psi\rangle$, and

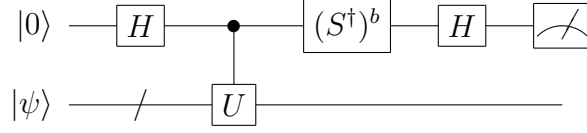


Figure 6: Scheme of the Hadamard Test for estimating the expectation value of the unitary operator U on the quantum state $|\psi\rangle$. The measurement of the ancilla qubit in the X basis ($b = 0$) yields the real part of $\langle\psi|U|\psi\rangle$, while the measurement in the Y basis ($b = 1$) yields the imaginary part. The operation S^\dagger introduces a phase of $e^{-i\frac{\pi}{2}}$ when $b = 1$, enabling the measurement of the imaginary part.

an ancilla qubit. The algorithm applies a controlled version of the target unitary operator U , denoted as C_U , to the state $|\psi\rangle$, with the ancilla serving as the control qubit, as illustrated in Figure 6. The ancillary register's measurement yields an outcome that is proportional to the expectation value of the operator U on the state $|\psi\rangle$. Consequently, this algorithm enables the estimation of the expectation value of a given unitary operator without requiring full knowledge of the quantum state $|\psi\rangle$. The state after the application of the U operator in its controlled version is depicted below.

$$\begin{aligned}
|0\rangle \otimes |\psi\rangle &\xrightarrow{H \otimes \mathbf{1}} \frac{1}{\sqrt{2}} (|0\rangle + |1\rangle) \otimes |\psi\rangle \\
&\xrightarrow{C_U} \frac{1}{\sqrt{2}} (|0\rangle \otimes |\psi\rangle + |1\rangle \otimes U|\psi\rangle)
\end{aligned} \tag{2.15}$$

Hence, the correspondence between the measurement outcome on the ancillary register and the expectation value of the operator U becomes apparent. In the case of $b = 0$, the ancillary register is measured in the X basis, providing the real part $\text{Re}\{\langle\psi|U|\psi\rangle\}$ as depicted in Equation 2.16. Conversely, when $b = 1$, the measurement is conducted in the Y basis, allowing for the measurement of the imaginary part $\text{Im}\{\langle\psi|U|\psi\rangle\}$ as shown in Equation 2.17.

$$\begin{aligned}
\langle X \rangle_{\text{ancilla}} &= \frac{1}{2} \left[\langle 0| \otimes \langle \psi| + \langle 1| \otimes \langle \psi| U^\dagger \right] X_{\text{ancilla}} \left[|0\rangle \otimes |\psi\rangle + |1\rangle \otimes U|\psi\rangle \right] \\
&= \frac{1}{2} \langle \psi| U + U^\dagger |\psi\rangle \\
&= \text{Re}\{\langle\psi|U|\psi\rangle\}
\end{aligned} \tag{2.16}$$

$$\begin{aligned}
\langle Y \rangle_{\text{ancilla}} &= \frac{1}{2} \left[\langle 0| \otimes \langle \psi| + \langle 1| \otimes \langle \psi| U^\dagger \right] Y_{\text{ancilla}} \left[|0\rangle \otimes |\psi\rangle + |1\rangle \otimes U|\psi\rangle \right] \\
&= \frac{1}{2} \langle \psi| - iU + iU^\dagger |\psi\rangle \\
&= \text{Im}\{\langle\psi|U|\psi\rangle\}
\end{aligned} \tag{2.17}$$

By utilizing the Hadamard Test algorithm, as demonstrated earlier, it is possible to estimate the expectation values of the real or imaginary parts of unitary operators. This estimation is achieved by performing

distinct measurements and evaluating the expectation value of the ancillary register in the selected basis, either X (when $b = 0$) or Y (when $b = 1$).

It is important to note that in this methodology, the main register is not directly measured. Instead, the final state of this register is obtained by applying $(\mathbb{1} \pm U) |\psi\rangle$ (when $b = 0$), depending on whether the measured state is $|0\rangle$ or $|1\rangle$. This characteristic is effectively employed in the implementation of iterative quantum phase estimation. However, due to the scope of this dissertation, the intricate details of the iterative quantum phase estimation algorithm will not be elaborated. For comprehensive insights, please refer to the provided citation [Dobšiček et al. \[2007\]](#).

2.3.5 Quantum Phase Estimation (QPE)

Let's consider a unitary operator U and an eigenstate of this operator $|\psi\rangle$ such that $U |\psi\rangle = e^{i2\pi\phi} |\psi\rangle$ the quantum phase estimation algorithm is an application of the Quantum Fourier Transform (QFT) (see Subsection 2.3.3). The QPE algorithm aims to estimate the phase ϕ [Abrams and Lloyd \[1999\]](#). The algorithm consists in two registers, the ancillary register with n -qubits where the estimation of ϕ will be performed and a main register of m -qubits for encoding the eigenstate $|\psi\rangle$.

The algorithm begins by preparing the ancillary register in a complete superposition state using Hadamard gates applied to each qubit. Then, controlled versions of powers of the unitary operator U (called oracles) are applied, where the n -th qubit controls the operation U^{2^0} , the $(n - 1)$ -th qubit controls U^{2^1} , and so on, until the first qubit controls $U^{2^{n-1}}$. The effect of these operations can be observed through the following equation:

$$\begin{aligned} |0\rangle^{\otimes n} \otimes |\psi\rangle &\xrightarrow{H^{\otimes n}} \frac{1}{\sqrt{2^n}} \sum_{k=0}^{2^n-1} |k\rangle \otimes |\psi\rangle \\ &\xrightarrow{\text{oracles}} \frac{1}{\sqrt{2^n}} \left(|0\rangle + e^{i2\pi(2^{n-1}\phi)} |1\rangle \right) \otimes \dots \otimes \left(|0\rangle + e^{i2\pi(2^0\phi)} |1\rangle \right) \otimes |\psi\rangle \quad (2.18) \\ &= \frac{1}{\sqrt{2^n}} \sum_{k=0}^{2^n-1} e^{i2\pi k\phi} |k\rangle \otimes |\psi\rangle \end{aligned}$$

This result is analogous to the expression in Equation 2.14. Therefore, it is possible to obtain a good estimation φ of ϕ by applying the inverse Quantum Fourier Transform (QFT^\dagger). The application of the inverse transform is represented by the following equation:

$$\begin{aligned}
\frac{1}{\sqrt{2^n}} \sum_{k=0}^{2^n-1} e^{i2\pi k\phi} |k\rangle \otimes |\psi\rangle &\xrightarrow{QFT^\dagger} \frac{1}{2^n} \sum_{k=0}^{2^n-1} \sum_{j=0}^{2^n-1} \exp\left\{-i\frac{2\pi}{2^n}k(j-2^n\phi)\right\} |j\rangle \otimes |\psi\rangle \\
&= \frac{1}{2^n} \sum_{k=0}^{2^n-1} \sum_{j=0}^{2^n-1} \exp\left\{-i\frac{2\pi}{2^n}k(j-\varphi)\right\} e^{i2\pi\delta k} |j\rangle \otimes |\psi\rangle
\end{aligned} \tag{2.19}$$

Since $\phi \in [0, 1]$, it is possible to approximate the value of $2^n\phi = \varphi + 2^n\delta$, where $\varphi \in \mathbb{Z}^+$ represents the nearest integer that approximates the eigenvalue of $2^n\phi$. The value of δ represents the error in the approximation, and it is bounded by $0 \leq 2^n|\delta| \leq \frac{1}{2}$. This error arises when $2^n\phi$ cannot be exactly represented as a binary integer of n bits [Cleve et al. \[1998\]](#).

For example, consider $\phi = \frac{1}{3}$. In its binary fraction representation, ϕ is $0.0101\dots$, which cannot be exactly represented as a unique integer value for any n -bit string. Increasing the resolution of the ancillary register by augmenting the number of qubits can provide a more accurate approximation, but for this example, an exact solution is not possible.

The probability of successfully measuring in the ancillary register the integer that best approximates the value of $2^n\phi$, denoted as φ , is given by $P(\varphi)$:

$$\begin{aligned}
P(\varphi) &= \left| \frac{1}{2^n} \sum_{j=0}^{2^n-1} e^{i2\pi\delta k} \right|^2 \\
&= \left| \frac{1}{2^n} \frac{1 - (e^{i2\pi\delta})^{2^n}}{1 - e^{i2\pi\delta}} \right|^2 \\
&= \left(\frac{1}{2^n} \frac{\sin \pi\delta 2^n}{\sin \pi\delta} \right)^2 \\
&\geq \left(\frac{1}{2^n} \frac{2\delta 2^n}{\pi\delta} \right)^2 \\
&= \frac{4}{\pi^2}
\end{aligned} \tag{2.20}$$

$$\tag{2.21}$$

Therefore, the probability of measuring $|\varphi\rangle$ in the ancillary register and estimating the eigenvalue ϕ is at least $\frac{4}{\pi^2}$ for $\delta \neq 0$ and $\phi \approx \frac{\varphi}{2^n}$. On the other hand, when $\delta = 0$, the probability $P(\varphi) = 1$ and $\phi = \frac{\varphi}{2^n}$ can be exactly obtained. The complete algorithm is summarized in Figure 7. For more information about this algorithm, please refer to the works by [Cleve et al. \[1998\]](#), [Abrams and Lloyd \[1999\]](#), [Nielsen and Chuang \[2002\]](#)

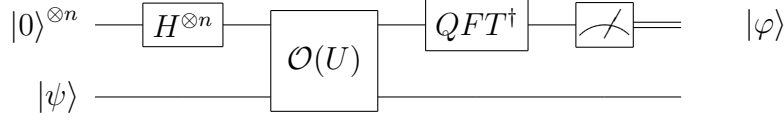


Figure 7: The circuit represents the Quantum Phase Estimation (QPE) algorithm, where U is the unitary operator of interest, $|\psi\rangle$ is the quantum eigenstate of U with eigenvalue $e^{i2\pi\phi}$, and n is the number of qubits in the ancillary register. The box labeled with $\mathcal{O}(U)$ represents the oracles corresponding to the controlled operations. The j -th qubit controls the operation $U^{2^{n-j}}$. Upon measurement, the state $|\varphi\rangle$ is obtained, where φ is the integer that provides the best estimate for $2^n\phi$.

2.3.6 Efficient Implementation of $|W\rangle$ States

The $|W\rangle$ state, named after Wolfgang Dür, is an entangled quantum state involving multiple qubits that demonstrates a form of multipartite entanglement. The general form of the $|W\rangle_N$ state for N qubits is given in the equation below [Dür et al. \[2000\]](#).

$$|W\rangle_N = \frac{1}{\sqrt{N}} (|0\dots 01\rangle + |0\dots 10\rangle + \dots + |1\dots 00\rangle) \quad (2.22)$$

Implement the $|W\rangle$ state can be achieved using an algorithm proposed by [Cruz et al. \[2019\]](#). This algorithm enables the preparation of the desired state for a general number of qubits N with a logarithmic time complexity $\mathcal{O}(\log_2 N)$, making it particularly useful for NISQ devices. This logarithmic complexity $\mathcal{O}(\log_2 N)$ is attained by leveraging the parallel execution capability of quantum operations on different qubits. By carefully selecting the target and control qubits, multiple controlled operations can be executed simultaneously, resulting in a logarithmic-depth $\mathcal{O}(\log_2 N)$ execution instead of the linear depth $\mathcal{O}(N)$ required by a sequential approach [Cruz et al. \[2019\]](#).

The algorithm relies on the application of unitary blocks $B(p)$, which are two-qubit gates with the effect shown in Equation 2.23. These gates can be decomposed into a controlled $G(p)$ (see Equation 2.24) operation and a standard $CNOT$ gate, as illustrated in Figure 8.

$$B(p) |00\rangle = |00\rangle, \quad B(p) |10\rangle = \sqrt{p} |10\rangle + \sqrt{1-p} |01\rangle \quad (2.23)$$

$$G(p) = \begin{pmatrix} \sqrt{p} & -\sqrt{1-p} \\ \sqrt{1-p} & \sqrt{p} \end{pmatrix} \quad (2.24)$$

In the sequential method, the unitary block is applied to pairs of qubits starting with qubits 1 and 2, then 2 and 3, and so on, up to the pair $N - 1$ and N for N qubits. The corresponding values of p for

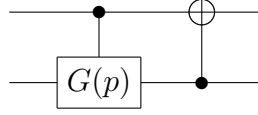


Figure 8: Decomposition of the $B(p)$ operator into a controlled $G(p)$ operation and a inverted $CNOT$ gate Cruz et al. [2019].

each block are determined by $\frac{1}{N}$, $\frac{1}{N-1}$, up to $\frac{1}{2}$.

In contrast, the logarithmic approach involves using different qubits for each parallel execution block. The values of p for each $B(p)$ block in this approach are calculated differently. The method proposed by D. Cruz employs a dichotomy tree to construct the algorithm. A dichotomy for an integer n is defined as $n = \lfloor n/2 \rfloor + \lceil n/2 \rceil$, where $\lfloor n/2 \rfloor$ and $\lceil n/2 \rceil$ are the lower and upper integer parts of $n/2$, respectively. The main idea is to build a dichotomy tree starting from the root, which is given by the pair $(\lfloor N/2 \rfloor, N)$. The leaves for a given node (n, m) are obtained by recursively applying the dichotomy operation, resulting in $(\lfloor n/2 \rfloor, \lfloor m/2 \rfloor)$ and $(\lceil n/2 \rceil, \lceil m/2 \rceil)$. This process continues until the tree reaches the leaves $(0, 1)$, $(1, 1)$, or $(1, 2)$, at which point the construction of the tree stops Cruz et al. [2019].

To illustrate this concept, let's consider the case of $N = 5$. The root of the dichotomy tree for $N = 5$ is $(2, 5)$, and the subsequent leaves can be seen in Figure 9a. In order to adapt the dichotomy tree concept for the $|W\rangle_N$ algorithm implementation, a *pruning* step is necessary. This pruning involves swapping the leaves $(1, 1)$ with $(1, 2)$ and eliminating the leaves $(0, 1)$ and $(1, 1)$. This results in a *pruned* dichotomy tree, which is used to construct the quantum algorithm.

Each node (n, m) in the pruned dichotomy tree corresponds to a block $B(n/m)$ in the algorithm. The control qubit for the controlled $G(p)$ operation is determined by the "upper line" if the block corresponds to the "upper child" (left node on the tree). Conversely, if the block corresponds to the "lower child" (right node on the tree), the control qubit is determined by the "lower line" of the parent node. The pruned tree for the given example with $N = 5$ can be seen in Figure 9b. The corresponding quantum circuit that implements the $|W\rangle_5$ state can be found in Figure 10.

The controlled operation $G(p)$ can be constructed in various ways using decomposition rules and relations with available quantum operations. In this case, the relation presented in Figure 11 is used, which involves $R_y(\theta_p)$ (see Table 2) rotations and a CNOT gate, where $\theta_p = \arcsin \sqrt{p}$.

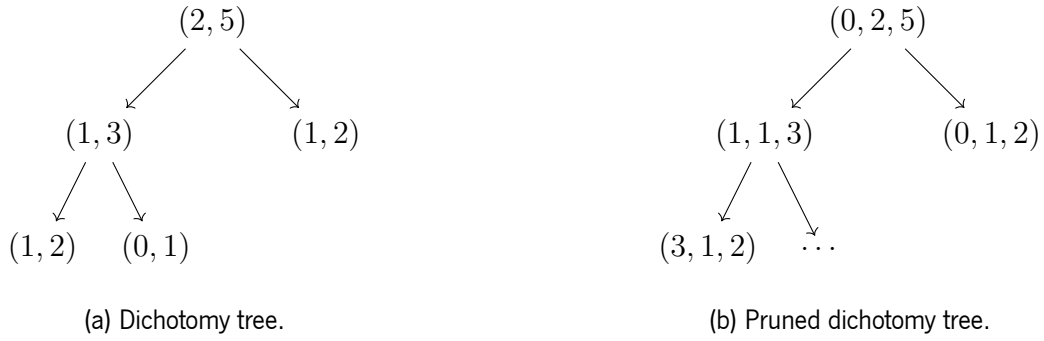


Figure 9: The Figure 9a shows the dichotomy tree for the case $N = 5$. The leaves on the right side of the tree correspond to the "lower child," while the leaves on the left side correspond to the "upper child." The Figure 9b displays the pruned tree obtained from the unpruned tree shown in the left figure. In the pruned tree, the node $(0, 1)$ has been removed. To clarify the control qubit for each leaf, the notation used for each node is (c, n, m) , where c represents the index of the control qubit (starting from 0), and n and m retain the same values as in the unpruned tree.

2.4 Spin Systems

The focus of this dissertation work is to study quantum systems through quantum simulation using digital quantum computers. The systems of interest in this study are those that can be described utilizing the spin degree of freedom. Hence, this section's objective is to introduce the key concepts related to such systems and introduce several pertinent models that will prove beneficial for the core discussions within this dissertation.

2.4.1 Spin

To comprehend the fundamental concept of a spin system, it's essential to begin with an exploration of spin itself. For this purpose, let's delve into the Stern-Gerlach Experiment (SGE) [Sakurai and Commins \[1995\]](#), [Kok \[2018\]](#). This experiment involves a particle source that emits neutral spin- $\frac{1}{2}$ particles through an inhomogeneous magnetic field \vec{B} generated by two magnets aligned along the vertical axis, commonly referred to as the \hat{z} axis. At the end of their trajectory, the particles are directed toward a screen where their positions are detected [Sakurai and Commins \[1995\]](#), [Kok \[2018\]](#). Refer to Figure 12 for a schematic representation of this experimental arrangement.

To elucidate the behavior of spin- $\frac{1}{2}$ particles in this setup, let's initially consider classical magnetic dipoles, represented as $\vec{\mu}$, traversing the magnetic field created by the magnets [Sakurai and Commins](#)

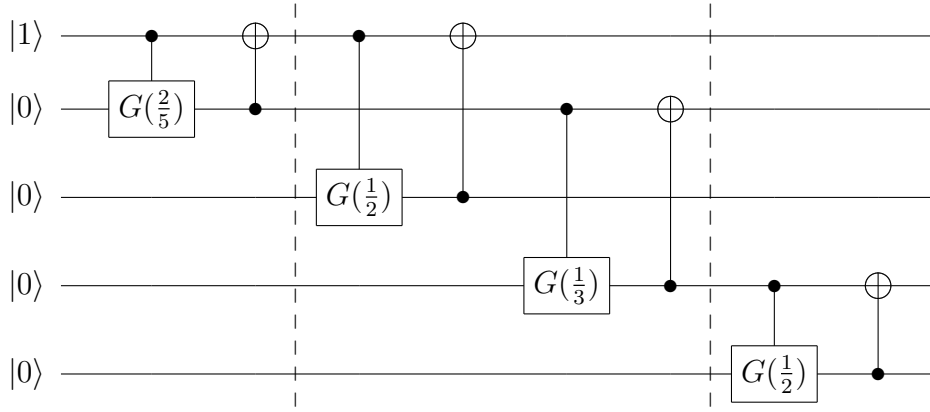


Figure 10: Quantum circuit for implementing the $|W\rangle_5$ state using the pruned dichotomy tree in 9b. Each block delimited by the barrier represents a parallel execution block, where, for instance, $B(\frac{1}{2})$ and $B(\frac{1}{3})$ are executed simultaneously. This reflects the logarithmic depth of the method, which in this case is $\lceil \log_2 5 \rceil = 3$.



Figure 11: Controlled $G(p)$ operator decomposition.

[1995]. The resulting force experienced by these dipoles can be expressed as:

$$\vec{F} = \nabla(\vec{\mu} \cdot \vec{B}) \quad (2.25)$$

Consequently, the deflection of these dipoles and their resulting positions on the detector screen will depend on their orientation with respect to the magnetic field. This phenomenon is visually depicted in Figure 13a Sakurai and Commins [1995]. In this setup, the classical dipoles are distributed along the entire \hat{z} axis, depending on the orientation of their magnetic momentum $\vec{\mu}$. However, when considering spin- $\frac{1}{2}$ particles, where the only degree of freedom under consideration for the Stern-Gerlach experiment is the spin, the results are depicted in Figure 13b. In contrast to classical magnetic dipoles, the quantum particles are deflected and hit the screen at only two positions along the \hat{z} axis. These positions correspond to the two possible values of the particle's spin $S_z = \pm\frac{1}{2}$. Hence, it is evident that the spin of a particle behaves like a magnetic dipole $\hat{\mu}$ (see Equation 2.26) in the presence of an external magnetic field. However, it is quantized, and for the present example of spin $S = \frac{1}{2}$, it has two possible values for its \hat{z} component Sakurai and Commins [1995], Kok [2018].

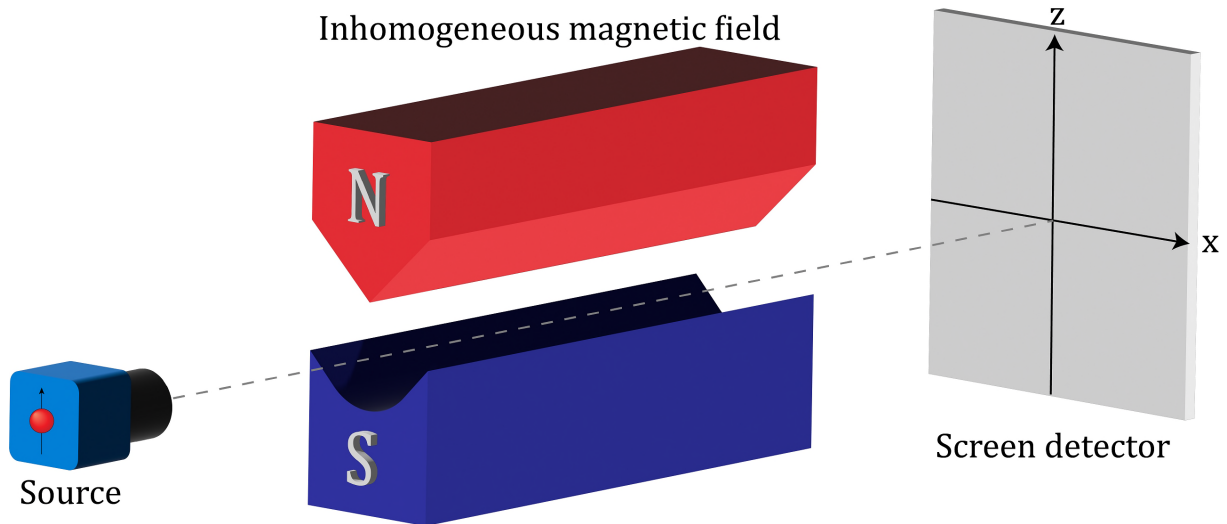


Figure 12: The figure depicts the schematic representation of the Stern-Gerlach experiment. It illustrates the particle source, the magnetic monopoles creating an inhomogeneous magnetic field \vec{B} , and the screen detector where particles are detected after passing through the magnetic field.

$$\hat{\vec{\mu}} = g\mu_B\hat{\vec{S}} \quad (2.26)$$

In this equation, g represents the gyromagnetic ratio, which has a value of $g = 2$ for particles with intrinsic spin. $\mu_B = \frac{e\hbar}{2m}$ denotes the elementary unit of magnetic moment, known as the Bohr magneton, where e stands for the electron charge, \hbar represents the reduced Planck constant, and m denotes the particle's mass [Sakurai and Commins \[1995\]](#), [Parkinson and Farnell \[2010\]](#). The operator $\hat{\vec{S}}$ corresponds to the spin vector operator associated with the particle.

Indeed, since the experiment involved non-charged particles, the observed outcomes can only be explained by the existence of spin as an intrinsic property of particles. This property is not restricted to a specific type of particle; rather, all elementary particles possess this degree of freedom [Merzbacher \[1998\]](#). For instance, electrons, neutrons, and protons are all spin- $\frac{1}{2}$ particles. Photons have a spin of $S = 1$, and the Higgs boson has a spin of $S = 0$. Here, particles can be categorized into two groups: Fermions and Bosons, which obey Fermi-Dirac and Bose-Einstein statistics, respectively. In terms of spin, fermions are those with *half-integer* spins ($\frac{1}{2}, \frac{3}{2}, \dots$), while bosons have *integer* spins [Sakurai and Commins \[1995\]](#), [Merzbacher \[1998\]](#).

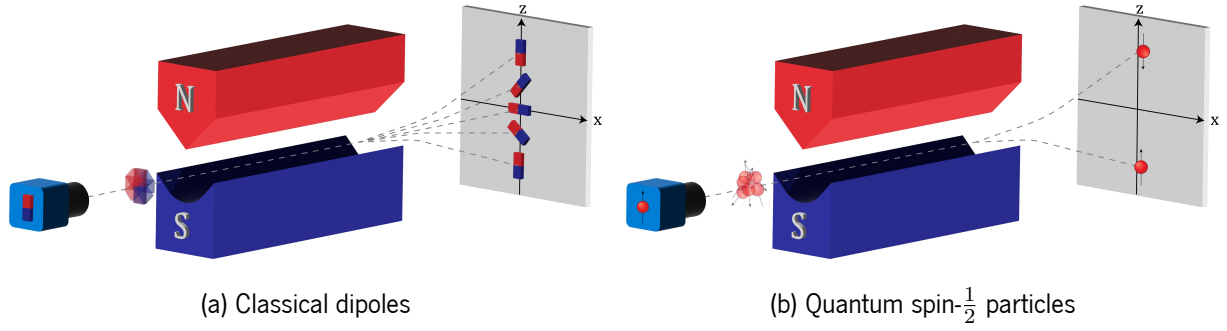


Figure 13: Schematic representation of the Stern-Gerlach experiment results: [13a](#) Using classical magnetic dipoles with different orientations of their magnetic moments $\vec{\mu}$ relative to the \hat{z} axis, the magnets deflect them based on their orientations, resulting in a distribution across the screen detector that spans the entire \hat{z} axis. [13b](#) In the quantum case, neutral spin- $\frac{1}{2}$ particles with various initial states are considered. The diagram illustrates the deflection of these particles to only two distinct points on the \hat{z} axis, determined by their \hat{z} spin components.

2.4.2 Spin Operators and Their Eigenstates

Spin behaves similarly to orbital angular momentum, and as a result, the quantum mechanics of spin operators follows the same principles. Consequently, we can describe the behavior of the total spin operator S^2 and S_z on their respective eigenstates. These eigenstates $|S, S_z\rangle$ are identified by their spin S value and their \hat{z} component [Sakurai and Commins \[1995\]](#), [Parkinson and Farnell \[2010\]](#).

$$\begin{aligned} S^2 |S, S_z\rangle &= S(S+1)\hbar^2 |S, S_z\rangle \\ S_z |S, S_z\rangle &= S_z\hbar |S, S_z\rangle \end{aligned} \quad (2.27)$$

The vector operator \vec{S} has three components that correspond to the \hat{x} , \hat{y} , and \hat{z} components of the spin. They are denoted as S_x , S_y , and S_z respectively. They follow the cyclic commutation relation $[S_i, S_j] = i\hbar\epsilon_{ijk}S_k$, where ϵ_{ijk} is the Levi-Civita symbol [Parkinson and Farnell \[2010\]](#). Moreover, two new operators, known as the raising and lowering operators, can be defined as $S^\pm = S_x \pm iS_y$. Their effects on the eigenstates are presented below [Parkinson and Farnell \[2010\]](#), [Pires \[2021\]](#).

$$\begin{aligned} S^\pm |S, S_z\rangle &= 0, & S_z &= S \\ S^\pm |S, S_z\rangle &= \hbar\sqrt{S(S+1) - S_z(S_z \pm 1)} |S, S_z \pm 1\rangle, & S_z &< S \end{aligned} \quad (2.28)$$

As the name suggests, these operators increase or decrease the \hat{z} component of the spin while transitioning between the eigenstates $|S, S_z\rangle$. For a particle with spin S , the allowed values for S_z are shown in Equation [2.29](#), and similarly for the other components when they are measured. For the purpose

of this work, the spin particles that we are going to consider are $S = \frac{1}{2}$ particles, such as electrons [Sakurai and Commins \[1995\]](#), [Parkinson and Farnell \[2010\]](#).

$$S_z \in \{-S, -S + 1, \dots, S - 1, S\} \quad (2.29)$$

Therefore, the possible values that they can have for the \hat{z} component are $S_z \in -\frac{1}{2}, \frac{1}{2}$. Moreover, the spin operators for these particles are directly related to the Pauli operators (X , Y and Z). From now on, we will consider $\hbar = 1$. The dimensionless spin operators can be written as follows [Sakurai and Commins \[1995\]](#).

$$\begin{aligned} S_x &= \frac{1}{2} X \\ S_y &= \frac{1}{2} Y \\ S_z &= \frac{1}{2} Z \end{aligned} \quad (2.30)$$

A final aspect to consider regarding spin angular momentum is the fact that it is possible to have systems with many spin particles. Therefore, describing these systems in terms of their spin degree of freedom is essential. The common approach to finding a basis that describes the total angular momentum $\vec{S}_T = \vec{S}_1 + \vec{S}_2 + \dots$ of the system is to use the angular momentum addition theorem [Sakurai and Commins \[1995\]](#). Using this theorem, it is straightforward to find the basis of this system of many particles. The eigenstates are calculated using the Clebsch-Gordan coefficients, which are commonly found in a table (Appendix C.I of [Messiah \[2014\]](#)).

To better understand this addition, let's consider a system consisting of two spin- $\frac{1}{2}$ particles. The basis states of the composite system resulting from the addition of the two individual particles, denoted as $S_{\frac{1}{2}} \otimes S_{\frac{1}{2}}$, can be described in terms of their total spin $S_T \in \{1, 0\}$. This implies that the system forms two distinct subspaces, one with a total spin of $S = 1$ and the other with $S = 0$. The possible \hat{z} spin projections for each subspace follow the relationship shown in Equation 2.29. By utilizing the Clebsch-Gordan coefficients, it becomes possible to determine how these eigenstates $|S_T, S_z\rangle$ are represented in terms of tensor product of the individual particle states $|S, S_z\rangle$.

$$\begin{aligned} |1, -1\rangle &= \left| \frac{1}{2}, -\frac{1}{2} \right\rangle \otimes \left| \frac{1}{2}, -\frac{1}{2} \right\rangle = |\downarrow\downarrow\rangle \\ |1, 0\rangle &= \frac{1}{\sqrt{2}} \left(\left| \frac{1}{2}, \frac{1}{2} \right\rangle \otimes \left| \frac{1}{2}, -\frac{1}{2} \right\rangle + \left| \frac{1}{2}, -\frac{1}{2} \right\rangle \otimes \left| \frac{1}{2}, \frac{1}{2} \right\rangle \right) = \frac{1}{\sqrt{2}} (|\uparrow\downarrow\rangle + |\downarrow\uparrow\rangle) \\ |1, 1\rangle &= \left| \frac{1}{2}, \frac{1}{2} \right\rangle \otimes \left| \frac{1}{2}, \frac{1}{2} \right\rangle = |\uparrow\uparrow\rangle \\ |0, 0\rangle &= \frac{1}{\sqrt{2}} \left(\left| \frac{1}{2}, \frac{1}{2} \right\rangle \otimes \left| \frac{1}{2}, -\frac{1}{2} \right\rangle - \left| \frac{1}{2}, -\frac{1}{2} \right\rangle \otimes \left| \frac{1}{2}, \frac{1}{2} \right\rangle \right) = \frac{1}{\sqrt{2}} (|\uparrow\downarrow\rangle - |\downarrow\uparrow\rangle) \end{aligned} \quad (2.31)$$

2.4.3 Heisenberg Model

The previous subsections have introduced the concept of spin and its description within quantum mechanics. This subsection and the following ones are dedicated to introducing various spin models that are relevant to this dissertation. As previously mentioned, a spin system comprises particles with spin, where their interactions with each other and the environment are primarily described using the spin degree of freedom. These interactions are encoded in spin model Hamiltonians, utilizing the quantum operators discussed earlier.

First, let's introduce the Heisenberg model. While this model was previously defined using the example of two spin- $\frac{1}{2}$ particles in the first chapter, it can actually be generalized to encompass varying numbers of spin particles, diverse geometries, and different types of spin particles. Fundamentally, the Heisenberg model elucidates interactions between spin particles. Its general representation is depicted in the Hamiltonian equation below [Pires \[2021\]](#).

$$H^{\text{Heis}} = \frac{1}{2} \sum_{ij} J_{ij} \vec{S}_i \cdot \vec{S}_j \quad (2.32)$$

In this equation, the interaction is represented by the dot product of the spin operators of particles i and j , where i and j encompass all particles within the system. The factor of $\frac{1}{2}$ is included to avoid double counting, and the exchange constant $J_{ij} = J_{ji}$ quantifies the strength of the interaction between particles i and j . To simplify the Hamiltonian, it is often assumed that only first-neighbour $\langle i, j \rangle$ interactions exist, all with the same strength $J_{ij} = -J$. This simplification, depicted in Equation 2.33, is common [Pires \[2021\]](#). Furthermore, for the purpose of this work, the considered geometry will be limited to $1D$ chains with periodic boundary conditions, as illustrated in Figure 14.

$$H^{\text{Heis}} = -J \sum_{\langle i, j \rangle} \vec{S}_i \cdot \vec{S}_j \quad (2.33)$$

If $J > 0$, the model is ferromagnetic, favoring a ground state where all spins align in the same direction. Conversely, if $J < 0$, the interaction is antiferromagnetic, causing spins to tend to align in opposite directions [Parkinson and Farnell \[2010\]](#), [Pires \[2021\]](#).

2.4.4 Spin Waves

To introduce the concept of spin waves, let's consider a Ferromagnetic Heisenberg model for N particles in a $1D$ dimensional chain. The ground state of this system is straightforward to find, as it's the state

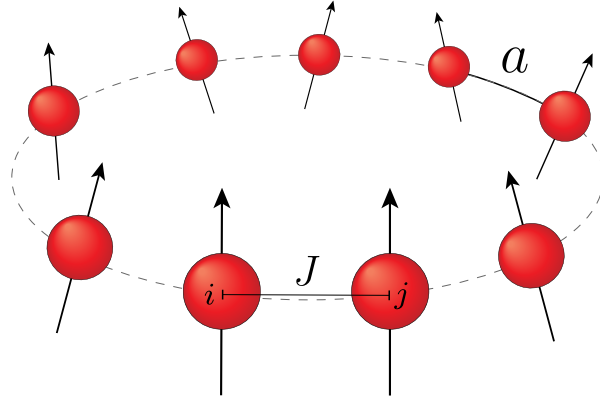


Figure 14: The figure illustrates a schematic representation of a 1D Heisenberg chain with periodic boundary conditions. Here, a represents the lattice constant, such that each spin particle is positioned at $r_i = (i - 1)a$, where $i \in [1, N]$, along the 1D chain. The value J signifies the exchange constant, determining the strength of interactions. It's important to note that the spin orientations shown are arbitrary, and the diagram is solely intended for didactic purposes.

in which all the spins point in the same direction. In this case, for simplicity, let's choose the positive \hat{z} orientation [Parkinson and Farnell \[2010\]](#), [Pires \[2021\]](#). We'll refer to this state as $|\psi_0\rangle$, as depicted below.

$$|\psi_0\rangle = |\uparrow\uparrow \dots \uparrow\rangle \quad (2.34)$$

The excited states of this simplified Hamiltonian would correspond to states where one or more spins are flipped to the $|\downarrow\rangle$ state. We will label these new states as $|\psi_i\rangle = S_i^- |\psi_0\rangle$ when the i -th spin is flipped [Parkinson and Farnell \[2010\]](#).

$$|\psi_i\rangle = |\dots \uparrow\downarrow\uparrow \dots\rangle \quad (2.35)$$

However, these states are not eigenstates of the Hamiltonian because there is no particular reason for a single i -th spin to be flipped while keeping the rest unchanged. Additionally, all the states that have a single spin flipped have the same energy. Therefore, the actual excited eigenstate, which is an eigenstate of the Hamiltonian, would be a uniform superposition of all these states, as shown below [Parkinson and Farnell \[2010\]](#).

$$|q\rangle = \frac{1}{\sqrt{N}} \sum_{n=1}^N e^{iqr_n} S_n^- |\uparrow\uparrow \dots \uparrow\rangle \quad (2.36)$$

This state $|q\rangle$ represents a magnon, which is a quantized version of the propagation of the spin perturbation, also known as a spin-wave. The term *spin-wave* refers to a plane wave e^{iqr_n} that traverses

the spins of the chain with a specific wave number q . Consequently, the effect of a single flipped spin is not localized to a particular spatial position; instead, it becomes delocalized throughout the chain [Parkinson and Farnell \[2010\]](#), [Pires \[2021\]](#).

2.4.5 Zeeman Effect

The Zeeman Effect refers to the splitting of energy levels within a given initial Hamiltonian H_0 when an external magnetic field \vec{B} is applied. This splitting of energy levels is a result of the interaction between the particle's orbital angular momentum and its spin angular momentum, which gives rise to a magnetic moment $\vec{\mu}$, as expressed in Equation 2.26. For the sake of simplicity, the contribution of orbital angular momentum is neglected, and thus, the Zeeman Effect is influenced by the intrinsic spin of the particle [Kok \[2018\]](#).

This effect is given by the Zeeman-type interaction described earlier, which corresponds to the coupling of its magnetic moment $\vec{\mu}$ with the magnetic field \vec{B} [Kok \[2018\]](#). To illustrate this effect, let's consider a single spin- $\frac{1}{2}$ particle Hamiltonian H_0 and the Zeeman interaction for a magnetic field oriented in the \hat{z} direction, given by $\vec{B} = B_z \hat{z}$, as shown below.

$$H = H_0 + g\mu_B B_z S_z \quad (2.37)$$

Let's consider, for simplicity, that $[H_0, S_z] = 0$ and that the initial energy E is given by:

$$E = \left\langle \frac{1}{2}, \pm \frac{1}{2} \left| H_0 \right| \frac{1}{2}, \pm \frac{1}{2} \right\rangle \quad (2.38)$$

The energy splitting is caused by the Zeeman term [Kok \[2018\]](#). The energy difference for each eigenstate $\left| \frac{1}{2}, \pm \frac{1}{2} \right\rangle$ is denoted as $\Delta E = g\mu_B B_z \frac{1}{2}$.

$$\left\langle \frac{1}{2}, \pm \frac{1}{2} \left| g\mu_B B_z S_z \right| \frac{1}{2}, \pm \frac{1}{2} \right\rangle = \pm g\mu_B B_z \frac{1}{2} \quad (2.39)$$

Therefore, the splitting can be represented as $E \pm \Delta E$ and depends on the value of the S_z component. This energy splitting phenomenon is summarized in Figure 15.

2.4.6 Dzyaloshinskii-Moriya interaction (DMI)

The Dzyaloshinskii-Moriya interaction (DMI) is named after physicists [Dzyaloshinsky \[1958\]](#) and [Moriya \[1960\]](#), who independently described this interaction in the mid-20th century. DMI arises from relativistic quantum effects due to the spin-orbit coupling within a crystal lattice. In simple terms, it occurs because

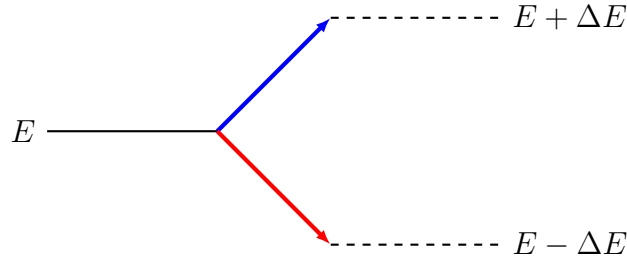


Figure 15: Zeeman splitting effect due to an applied magnetic field $\vec{B} = B_z \hat{z}$. The blue line corresponds to the splitting for the state $|\frac{1}{2}, \frac{1}{2}\rangle$, and the red one corresponds to the state $|\frac{1}{2}, -\frac{1}{2}\rangle$. The energy difference between the cases with and without a magnetic field is $\Delta z = g\mu_B B_z \frac{1}{2}$.

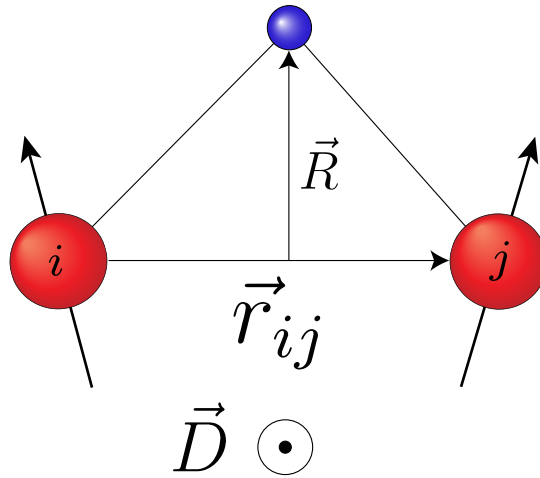


Figure 16: Illustration of the Dzyaloshinskii-Moriya Interaction (DMI). Electrons (red) in a crystal lattice experience a spin-orbit coupling influenced by the atomic nuclei (blue). This interaction induces a vector $\vec{D} \propto \vec{R} \times \vec{r}_{ij}$ that leads to non-collinear magnetic order in the material.

electrons moving through the atomic structure of a material experience an interaction with the atomic nuclei. This interaction is a result of the electron's intrinsic angular momentum, or spin, which generates an effective magnetic field as it moves. This can lead to subtle but significant interactions between neighboring magnetic moments [Dzyaloshinsky \[1958\]](#), [Moriya \[1960\]](#). The DMI is mathematically described by the following equation:

$$H^{\text{DMI}} = \vec{D} \cdot \vec{S}_i \times \vec{S}_j \quad (2.40)$$

In this equation, \vec{D} represents the Dzyaloshinskii-Moriya Interaction (DMI) vector, which is dependent on the crystal's geometry, determining its orientation and strength (see [Figure 16](#)). The cross product of two spins, $\vec{S}_i \times \vec{S}_j$, signifies a chiral coupling between adjacent spins. This is because the DMI encourages neighboring magnetic moments to adopt a non-collinear alignment. In other words, neighboring spins tend

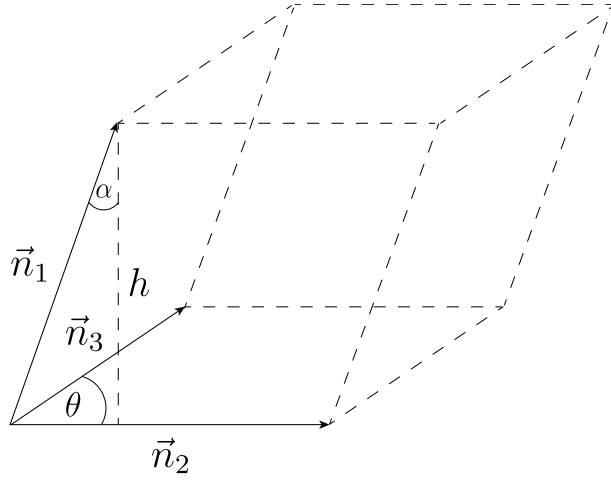


Figure 17: The volume of the parallelepiped is given by $V = h \cdot A_{\text{base}}$, where $h = \cos \alpha$ represents the height and $A_{\text{base}} = \sin \theta$ the area of the base. These relationships can be intuitively understood through geometry. Alternatively, the triple product $\vec{n}_1 \cdot \vec{n}_2 \times \vec{n}_3 = \cos \alpha \sin \theta$ yields the same result.

to prefer a specific helical arrangement rather than aligning perfectly parallel or antiparallel to each other [Dzyaloshinsky \[1958\]](#), [Moriya \[1960\]](#).

The Dzyaloshinskii-Moriya Interaction (DMI) can give rise to intriguing magnetic phenomena, most notably skyrmions [Fert et al. \[2017\]](#). Skyrmions are unique magnetic structures characterized by swirling and vortex-like spin patterns, representing topological spin structures within magnetic order [Fert et al. \[2017\]](#), [Sotnikov et al. \[2021\]](#). These structures exhibit stability and can be controlled using external fields, making them highly promising for future data storage and spintronic applications. These advancements hold great potential in various technological applications, including next-generation memory devices and quantum computing [Fert et al. \[2017\]](#).

2.5 Spin Chirality

In the field of quantum magnetism, the chirality operator $\hat{\chi}$ was introduced in 1989 with the purpose of characterizing a certain class of spin systems that exhibit a unique property: they break both P (parity) and T (time reversal) symmetries while preserving PT symmetry [Wen et al. \[1989\]](#). Here, P symmetry refers to the transformation of spatial coordinates, where $\vec{r} \rightarrow -\vec{r}$. Meanwhile, T symmetry involves the change in the sign of the time coordinate, represented as $t \rightarrow -t$. The breaking of these symmetries implies that the system exhibits different properties when subjected to individual operations of P and T inversion. Conversely, preserving PT symmetry means that the system remains invariant when both P and T inversions are applied simultaneously. This intriguing property sets these systems apart [Messiah \[2014\]](#).

The motivation of [Wen et al. \[1989\]](#) was to study chiral spin liquids (CSL) and explore their relevance in the context of high-temperature superconductors.

$$\hat{\chi} = \vec{\sigma}_1 \cdot \vec{\sigma}_2 \times \vec{\sigma}_3 \quad (2.41)$$

Here, $\vec{\sigma}_i = (X, Y, Z)$ denotes the vector operator comprised of the Pauli operators. There are several interpretations to explain what this operator means. One of the most intuitive interpretations is based on classical magnetism, where spins are described by classical vectors $\vec{S}_i = S\vec{n}_i$. In this context, the chirality operator quantifies the volume of the parallelepiped formed by the three classical spin vectors $\chi_{123}^{class} = S^3 \vec{n}_1 \cdot \vec{n}_2 \times \vec{n}_3$ (see [Figure 17](#)). This volume is a measure of the non-coplanarity of the spins. The chirality operator essentially characterizes how much the spins deviate from being in the same plane.

Therefore, in classical magnetism, the chirality operator serves as a metric for measuring the non-coplanarity of spin textures, such as skyrmions [Fert et al. \[2017\]](#) and frustrated ferromagnets [Taguchi et al. \[2001\]](#). Furthermore, recent works has extended this concept to quantum descriptions that go beyond the broken-symmetry paradigm [Roldán-Molina et al. \[2015\]](#), [Mazurenko et al. \[2023\]](#). In these quantum descriptions, the focus is on non-coplanar magnetic configurations, and the quantum version of the scalar spin chirality is identified as the appropriate order parameter to characterize these states [Sotnikov et al. \[2021\]](#).

Another possible interpretation arises when considering a system composed of three spin- $\frac{1}{2}$ particles $|\psi\rangle$, and their spins are transported around a loop through a cyclic permutation. This transformation induces a phase change in the system, commonly referred to as a Berry Phase. Consequently, the distinction between carrying out this transport around the loop in one direction \mathcal{B}_{123} versus the opposite direction \mathcal{B}_{132} is associated with the chirality of the system [Wen et al. \[1989\]](#).

$$\mathcal{B}_{123} - \mathcal{B}_{132} = \frac{i}{2} \langle \psi | \hat{\chi} | \psi \rangle$$

Furthermore, let's consider the Hubbard model in terms of creation ($c_{i\sigma}^\dagger$) and annihilation ($c_{i\sigma}$) operators. The creation operator ($c_{i\sigma}^\dagger$) creates an electron at site i with spin $\sigma \in \{\uparrow, \downarrow\}$, while the annihilation operator ($c_{j\sigma}$) destroys it [Cottam and Haghshenasfard \[2020\]](#).

$$H = -t \sum_{\langle i,j \rangle, \sigma} (c_{i\sigma}^\dagger c_{j\sigma} + \text{H.c.}) + U \sum_i n_{i\uparrow} n_{i\downarrow} \quad (2.42)$$

Here, the first term corresponds to the hopping between sites, and the second term represents the Coulomb repulsion U between electrons occupying the same site. A schematic representation of this model can be found in [Figure 18](#).

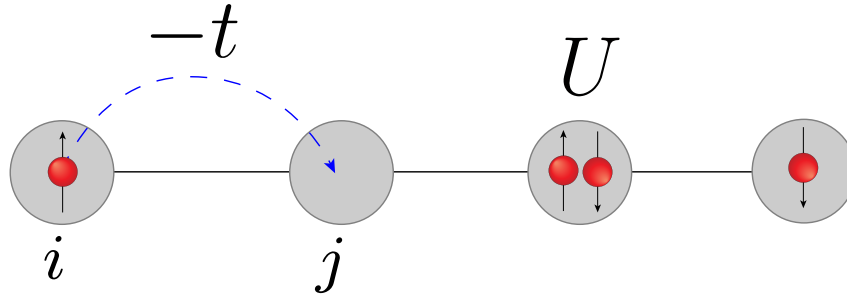


Figure 18: The figure shows a schematic representation of the Hubbard model. The blue arrow represents the hopping of one electron from site i to site j . Additionally, at the site with two electrons, there is the Coulomb repulsion term.

When considering this model in the strong-coupling limit, where $U \gg t$, the Coulomb repulsion prevents two electrons from occupying the same site. The analysis results in an effective Hamiltonian that can be studied in terms of only spin operators. This conventional approach leads to the Heisenberg model. However, this also results in a weak interaction term defined by the chirality interaction. Here, $\hat{\chi}$ represents the orbital moment operator of electrons circulating in three-site loops, and it couples linearly to an applied magnetic field [Sen and Chitra \[1995\]](#).

2.6 Genuine tripartite entanglement and spin chirality

Genuine Tripartite Entanglement (GTE) in quantum information refers to a unique form of entanglement that occurs among three quantum subsystems. This level of entanglement signifies that these subsystems, although potentially physically separated, cannot be treated as independent and non-entangled entities. As a well-established measure, quantifying this value is crucial for comprehending the entanglement structure within complex quantum systems since entanglement is recognized as a potent resource in quantum information science, including applications like quantum cryptography and communication [Xie and Eberly \[2021\]](#).

There are several approaches to measure tripartite entanglement. However, for the purpose of this work, we are going to consider the one proposed by [Xie and Eberly \[2021\]](#). This measurement technique is known as the Concurrence Fill. The Concurrence Fill involves calculating the area of the concurrence triangle, as shown in Figure 19. The vertices of the triangle represent the qubits, and the length of the edge between qubits i and $j \in \{1, 2, 3\}$ is determined by the square bipartite concurrence C_{ij} of [Wootters \[1998\]](#).

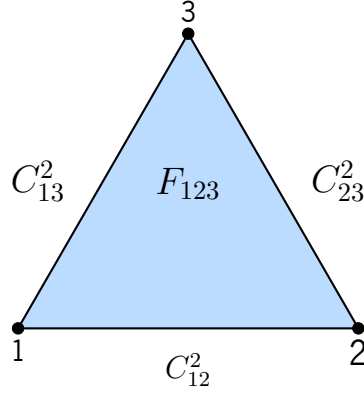


Figure 19: The figure shows a schematic representation of the Concurrence Fill. The vertices represent the qubits, and the edges are labeled as C_{ij} , where i and j correspond to the vertices of the edge. The length of the edge between qubits i and $j \in \{1, 2, 3\}$ is determined by the square bipartite concurrence C_{ij} .

$$C_{ij}(\rho) = \sqrt{2(1 - \text{Tr} \rho_{\mathcal{M}}^2)} \quad (2.43)$$

Where ρ is the system's density matrix and $\rho_{\mathcal{M}}$ represents the reduced matrix obtained by tracing over one side of the bipartition ij . Therefore, the Concurrence Fill F_{123} is defined as the area of this triangle, which can be calculated using Heron's formula, and $\frac{16}{3}$ is a normalization factor. [Xie and Eberly \[2021\]](#).

$$F_{123} \equiv \left[\frac{16}{3} Q (Q - C_{12}^2) (Q - C_{23}^2) (Q - C_{13}^2) \right]^{1/4} \quad (2.44)$$

$$Q = \frac{1}{2} (C_{12}^2 + C_{23}^2 + C_{13}^2) \quad (2.45)$$

On the other hand, [Tsomokos et al. \[2008\]](#) demonstrated that scalar spin chirality can be employed as a witness for genuine tripartite entanglement (GTE). In their work, they have shown that for a product state, the chirality is bounded by $|\hat{\chi}| \leq 1$. Consequently, if the chirality exceeds this value, it indicates the presence of correlations between two or more spins. They also investigated the chirality for a bipartite state and found that the maximum chirality is $|\hat{\chi}| = 2$. Finally, when the expectation value of the chirality operator $\langle \hat{\chi} \rangle$ surpasses a critical threshold of $\langle \hat{\chi} \rangle > 2$, it certifies the existence of genuine tripartite entanglement (GTE) [Tsomokos et al. \[2008\]](#).

Therefore, the primary focus of this dissertation, as described in the first chapter, is to develop a digital quantum circuit aimed at contributing to the study of systems exhibiting scalar spin chirality. Digital

quantum simulation of chiral spin states involves two main research directions: the synthesis of chiral logic gates to prepare and simulate the dynamics of chiral spin states [Ma et al. \[2017\]](#), [Wang et al. \[2019\]](#), and the development of measurement schemes to identify chiral spin states [Mazurenko et al. \[2023\]](#), [Sotnikov et al. \[2022\]](#). Our work contributes to the latter aspect. While [Sotnikov et al. \[2022\]](#) proposed a hardware-efficient approach to identify phase transitions associated with changes in scalar spin chirality by measuring in two or more random single-qubit bases and coarse-graining the outcomes to probe inter-scale dissimilarities [Sotnikov et al. \[2021\]](#), here we follow a physically-motivated strategy in which we compute the expectation value of the scalar spin chirality.

2.7 Methodology

This chapter serves as a guide to the methodologies employed throughout this dissertation to address its primary objectives. The methods chosen for this research encompass analytical calculations and computer-assisted simulations.

2.7.1 Python

Python, a high-level programming language created by Guido van Rossum, plays a central role in this research. Python is renowned for its versatility and wide application in scientific and numerical programming [Van Rossum et al. \[1995\]](#). In this work, Python, specifically version 3.10, along with its open-source libraries, serves as the primary toolset for executing all calculations and simulations.

In the following sections, we will introduce the most relevant libraries used in this dissertation for analytical calculations and simulations. Additionally, we employed several Python libraries to streamline calculation and simulation programming and to visualize the results presented in this work. These libraries include NumPy, which specializes in multidimensional array operations for scientific computing [Harris et al. \[2020\]](#); Matplotlib, utilized for visualizing results [Hunter \[2007\]](#); and SciPy, a library encompassing a wide range of mathematical algorithms and tools [Virtanen et al. \[2020\]](#).

2.7.2 Analytical Calculations

This dissertation utilizes analytical calculations to assess the feasibility and validity of the developed quantum circuits. These calculations adhere to the quantum mechanics and quantum computing principles outlined in the previous chapter. They constitute a fundamental aspect of this research, supporting the theoretical investigation of the proposed chirality indirect measurement methods and validating the results

obtained in the exploration of diverse spin models.

Furthermore, while most analytical calculations were performed manually, Python tools were employed to verify preliminary results and facilitate other calculations. For instance, the SymPy library was used for this purpose. SymPy is an open-source Python library designed for symbolic mathematics, a form of computation known as a computer algebra system (CAS) [Meurer et al. \[2017\]](#). This library streamlines tasks such as diagonalizing quantum operators to find their exact eigenvalues and eigenstates, as well as determining various many-body quantum operators through their explicit expressions.

2.7.3 Computer-Assisted Simulations

The computational simulations used in this research rely on two main libraries: Qiskit [Qiskit contributors \[2023\]](#) and QuSpin [Weinberg and Bukov \[2017, 2019\]](#). Qiskit aids in quantum computing simulations to test quantum circuits, while QuSpin is employed for classical simulations of the quantum systems used in this work.

Qiskit

Qiskit is an open-source software library powered by Python [Qiskit contributors \[2023\]](#). It facilitates the construction of quantum programs at the level of quantum circuits. Developed by IBM (International Business Machines Corporation), this software facilitates the creation and simulation of quantum programs using provided quantum computer simulators running on classical computers. These simulators can operate either noiselessly or with noise, mimicking real quantum hardware. Furthermore, Qiskit, in conjunction with the IBM cloud, enables the execution of quantum circuits on actual IBM-provided quantum hardware [Qiskit contributors \[2023\]](#). In this dissertation, we exclusively use the noiseless simulator, as the primary aim is to identify a well-suited Noisy Intermediate-Scale Quantum (NISQ) quantum circuit for chirality probing under ideal noiseless conditions. Moreover, all quantum circuits proposed for chirality measurement are tested using Qiskit. In Chapter 5, where chirality for various models will be tested, Qiskit simulations estimate chirality by emulating a noiseless quantum computer.

QuSpin

QuSpin is an open-source library employed for exact diagonalization and quantum dynamics of arbitrary boson, fermion, and spin many-body systems [Weinberg and Bukov \[2017, 2019\]](#). QuSpin enables the construction of diverse quantum systems and the determination of their properties through classical methods, including finding eigenstates and eigenvalues. It facilitates the modeling of spin systems and the explo-

ration of quantum observables, which can also be implemented [Weinberg and Bukov \[2017, 2019\]](#). In this dissertation, QuSpin serves as a tool to implement spin models and obtain their chirality. The results obtained using QuSpin are considered exact, against which estimations using Qiskit are compared.

Chapter 3

Chirality Eigenstate Preparation

The objective of this dissertation is to propose quantum circuits for measuring the chirality of a given quantum state. To achieve this goal, it is necessary to start with states whose chirality is well-known, using them to test various measurement approaches. The straightforward strategy involves utilizing chirality eigenstates. Hence, this chapter will identify these eigenstates and present a quantum circuit capable of preparing them within a quantum computer.

The chirality eigenstates can be easily obtained by diagonalizing the chirality operator, as referenced in [Wen et al. \[1989\]](#). Since the chirality operator is Hermitian, its eigenvalues are real. Furthermore, the rotational symmetry of this operator results in the chirality operator sharing the same eigenstates as the total spin operator $S^2 = (\hat{S}_1 + \hat{S}_2 + \hat{S}_3)^2$ and the S_z operator. This relationship can also be understood through the properties of the $\hat{\chi}^2$ operator (refer to Equation 3.1).

$$\hat{\chi}^2 = -4 \left(\hat{S}_1 + \hat{S}_2 + \hat{S}_3 \right)^2 + 15 \quad (3.1)$$

According to the angular momentum addition theorem, for a system of three spin- $\frac{1}{2}$ particles, a basis can be formed in which the total angular momentum is divided into a spin- $\frac{3}{2}$ multiplet denoted as $|S = \frac{3}{2}, S_z\rangle$ (see Equation 3.2), and two spin- $\frac{1}{2}$ multiplets denoted as $|S = \frac{1}{2}, S_z\rangle^\lambda$ (see Equation 3.3), where λ can take values of ± 1 [Wen et al. \[1989\]](#).

Equation 3.1 demonstrates that the multiplet with $S = \frac{3}{2}$ has zero chirality, while the multiplet with $S = \frac{1}{2}$ should have non-zero chirality values, specifically $\pm 2\sqrt{3}$. To construct the chirality operator's eigenstates, the states with $S = \frac{3}{2}$ are first generated using the angular momentum addition theorem. Then, the corresponding spin- $\frac{1}{2}$ states with $S = \frac{1}{2}$ are constructed to be orthogonal to the $|S = \frac{3}{2}, S_z\rangle$ states by adding certain phases ω and ω^2 , which are the cube roots of unity, satisfying the condition $1 + \omega + \omega^2 = 0$. In this context, $\omega = e^{i\frac{2\pi}{3}}$. Hence, the eigenstates of the chirality operator are presented below.

$$\begin{aligned}
|S = \frac{3}{2}, S_z = \frac{3}{2}\rangle &= |\uparrow\uparrow\uparrow\rangle \\
|S = \frac{3}{2}, S_z = \frac{1}{2}\rangle &= \frac{1}{\sqrt{3}} (|\downarrow\uparrow\uparrow\rangle + |\uparrow\downarrow\uparrow\rangle + |\uparrow\uparrow\downarrow\rangle)
\end{aligned} \tag{3.2}$$

$$\begin{aligned}
|S = \frac{1}{2}, S_z = \frac{1}{2}\rangle^{+1} &= \frac{1}{\sqrt{3}} (|\downarrow\uparrow\uparrow\rangle + \omega |\uparrow\downarrow\uparrow\rangle + \omega^2 |\uparrow\uparrow\downarrow\rangle) \\
|S = \frac{1}{2}, S_z = \frac{1}{2}\rangle^{-1} &= \frac{1}{\sqrt{3}} (|\downarrow\uparrow\uparrow\rangle + \omega^2 |\uparrow\downarrow\uparrow\rangle + \omega |\uparrow\uparrow\downarrow\rangle)
\end{aligned} \tag{3.3}$$

The eigenstates with $S_z = -\frac{1}{2}$ and $S_z = -\frac{3}{2}$ can be easily found by applying the spin flip operator $|\uparrow\rangle \rightarrow |\downarrow\rangle$ to all three spins. Therefore, for the purpose of our discussion, we can focus on these eigenstates based on their chirality eigenvalue χ .

$$\hat{\chi} |\chi = \lambda, S_z\rangle = 2\sqrt{3} \lambda |\chi = \lambda, S_z\rangle \tag{3.4}$$

The notation $\lambda \in \{0, \pm 1\}$ represents the values of zero, positive and negative chirality, respectively. Therefore, the following section will cover the implementation of these states in a quantum computer.

3.1 Building Chirality Eigenstates

In the context of our quantum simulation on quantum computers, it is necessary to map the previously discussed eigenstates to the quantum computational basis. This mapping can be easily accomplished by associating $|\uparrow\rangle$ with $|0\rangle$ and $|\downarrow\rangle$ with $|1\rangle$. Furthermore, it's important to note that in our earlier discussion, we adopted a ket notation order where the first particle is placed on the top left and the last particle on the top right. This arrangement is referred to as *little-endian* notation, indicating that the lowest index comes first. However, in contrast, Qiskit, which we will be using along with Python, employs the *big-endian* notation. In this notation, the last particle is positioned on the top left, and the first particle on the top right. For consistency, we will adhere to the 'big-endian' scheme in our notation.

Hence, in this section, the chirality eigenstates in the quantum computational notation are divided based on the difficulty of preparing them on a quantum computer. The trivial chirality eigenstates with $\chi = 0$ are $|000\rangle$ and $|111\rangle$. The non-trivial eigenstates can be found below.

$$\left| \chi = \lambda, S_z = \frac{1}{2} \right\rangle = \frac{1}{\sqrt{3}} (|001\rangle + \omega_\lambda |010\rangle + \omega_\lambda^2 |100\rangle) \tag{3.5}$$

Here, $\lambda \in \{0, \pm 1\}$ denotes the zero, positive, and negative chirality non-trivial eigenstates with $S_z = \frac{1}{2}$, and $\omega_\lambda = e^{i\frac{2\pi}{3}\lambda}$. Similarly, the remaining eigenstates with $S_z = -\frac{1}{2}$ are obtained by flipping the states $|0\rangle \rightarrow |1\rangle$ and $|1\rangle \rightarrow |0\rangle$.

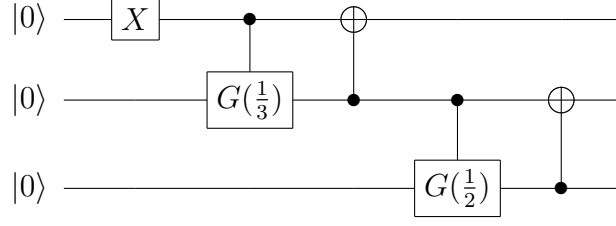


Figure 20: This figure depicts the quantum circuit $|W\rangle_3 \langle 0|^{\otimes 3}$ that prepares the $|W\rangle_3$ state.

These non-trivial eigenstates are entangled states that belong to the W class, with both zero chirality or non-zero chirality. This is why the preparation of the $|W\rangle$ states was discussed in the previous chapter 2.3.6. Consequently, the entangled state with zero chirality and $S_z = \frac{1}{2}$ can be implemented straightforwardly by following the implementation of $|W\rangle$ states for $N = 3$ qubits (see Figure 20).

$$|W\rangle_3 = \frac{1}{\sqrt{3}} (|001\rangle + |010\rangle + |100\rangle) \quad (3.6)$$

The state with $S_z = -\frac{1}{2}$ has the opposite spin orientation, and the quantum operations required to transform the simple $|W\rangle_3$ state into this state involve flipping each individual qubit. The gate that performs this operation is the Pauli X . Hence, at the end of the encoding of the $|W\rangle_3$ state, it is only necessary to apply the $X^{\otimes 3}$ operator. These relations are summarized in Equation 3.7.

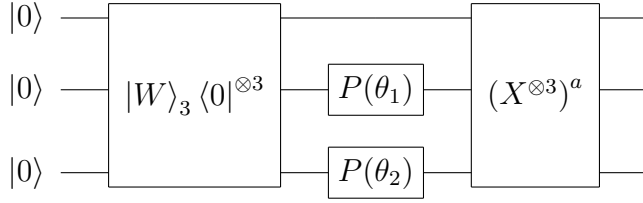
$$\begin{aligned} |\chi = 0, S_z = \frac{1}{2}\rangle &= |W\rangle_3 \\ |\chi = 0, S_z = -\frac{1}{2}\rangle &= X^{\otimes 3} |W\rangle_3 \end{aligned} \quad (3.7)$$

The eigenstates with non-zero chirality can be prepared by adding certain phases to the $|W\rangle_3$ states and flipping the qubits in the case of $S_z = -\frac{1}{2}$. The operator $P(\phi)$ applies the desired phase ϕ to the qubits. For instance, consider the states $|\chi = -1, S_z\rangle$. The construction of these states is depicted by Equation 3.8.

$$\begin{aligned} |\chi = -1, S_z = \frac{1}{2}\rangle &= (P(\frac{2\pi}{3}) \otimes P(\frac{4\pi}{3}) \otimes \mathbf{1}) |W\rangle_3 \\ |\chi = -1, S_z = -\frac{1}{2}\rangle &= X^{\otimes 3} |\chi = -1, S_z = \frac{1}{2}\rangle \end{aligned} \quad (3.8)$$

The states with positive chirality can be constructed using the same approach, with the only difference being the change in phases from ω to ω^2 , as shown in Equation 3.9. The circuit that summarizes the preparation of these states can be seen in Figure 21. Note that this circuit uses the computational basis notation, specifically the Big-endian scheme, where the higher index is positioned on the left side of the ket notation. In terms of the quantum circuit representation, the higher index corresponds to the bottom line of the circuit.

$$\begin{aligned}
|\chi = 1, S_z = \frac{1}{2}\rangle &= (P(\frac{4\pi}{3}) \otimes P(\frac{2\pi}{3}) \otimes \mathbb{1}) |W\rangle_3 \\
|\chi = 1, S_z = -\frac{1}{2}\rangle &= X^{\otimes 3} |\chi = 1, S_z = \frac{1}{2}\rangle
\end{aligned}
\tag{3.9}$$



χ	$P(\theta_1)$	$P(\theta_2)$
0	$\mathbb{1}$	$\mathbb{1}$
$2\sqrt{3}$	ω	ω^2
$-2\sqrt{3}$	ω^2	ω

Figure 21: The left Figure represents the quantum algorithm in the form of a circuit, with the corresponding values for the phases provided in the table on the right. The values of these phases depend on the desired state to be prepared. For states with zero chirality, no phase is applied. For states with positive chirality, the phases used are ω and ω^2 , while for states with negative chirality, the phases are ω^2 and ω , as indicated in the table and explained in the text. The value of a in the last operator changes between states with $S_z = \frac{1}{2}$ when $a = 0$, and $S_z = -\frac{1}{2}$ when $a = 1$.

Chapter 4

Chirality Measurement

In the field of quantum simulation, considerable efforts have been made to develop algorithms that can prepare specific quantum states. However, there is a noticeable lack of quantum algorithms focused on extracting information from a system through measurements. The most commonly employed method for measuring the expectation values of operators is quantum tomography. Unfortunately, this approach has the drawback of requiring measurements on all the qubits that encode the states, considering all possible combinations of Pauli's strings that form the operator. Therefore, the objective of this dissertation project is to propose alternative approaches that minimize the number of measurements needed. This chapter will present the developed methods, offering promising solutions to this challenge.

These approaches are based on different existing methods such as the Linear Combination of Unitaries (LCU), Quantum Phase Estimation (QPE), Hadamard Test, and combinations thereof. In the subsequent sections, these methods will be discussed in more detail. The chirality eigenstates, which were previously discussed, assist in testing the proposed approaches since their chirality is already known.

This chapter exclusively employs chirality eigenstates for evaluating and comparing the methods via simulations implemented using Qiskit. Towards the end of the chapter, a thorough comparison will be carried out to discern the unique strengths exhibited by each algorithm. This comparative analysis will enable the identification of the strengths and weaknesses of each algorithm, facilitating the selection of the most suitable approach based on specific applications.

4.1 Characterizing Chirality through Permutation Operations

The chirality operator is defined as the box product of spin vector operators for three particles. However, as outlined in the theoretical background chapter, the concept of chirality is intimately linked to order parameters associated with the violation of parity (P) and time-reversal (T) symmetry. This connection has inspired an alternative definition of the chirality operator, proposed by [Subrahmanyam \[1994\]](#), in terms of

spin permutation operators.

To define the chirality operator as proposed by [Subrahmanyam \[1994\]](#), we start by introducing the operator Θ_i . This operator is defined for a general number of N spin-1/2 particles and is obtained by taking the product of $\lfloor \frac{N-1}{2} \rfloor$ permutations P_{ij} . These permutation operators swap the states between sites i and j . In the context of spin operators, the permutation operator can be described as $P_{ij} = 2 \left(\vec{S}_i \cdot \vec{S}_j + \frac{1}{2} \right)$. In quantum computing, the equivalent operation to the permutation operator is a SWAP operation that exchanges qubits i and j .

$$\begin{aligned} \Theta_i &= \prod_{j=1}^{\lfloor \frac{N-1}{2} \rfloor} P_{(i+j)(N+i-j)} \\ &= 2^{\lfloor \frac{N-1}{2} \rfloor} \prod_{j=1}^{\lfloor \frac{N-1}{2} \rfloor} \left(\vec{S}_{i+j} \cdot \vec{S}_{N+i-j} + \frac{1}{2} \right) \end{aligned} \quad (4.1)$$

Hence, the definition proposed by [Subrahmanyam \[1994\]](#) can be observed in Equation 4.2 for the case of $N = 3$. In his paper, this definition is generalized for an arbitrary number of spin-1/2 particles. The issue with this definition is that it is specific to a particular type of system governed by the Heisenberg Hamiltonian, unlike the conventional definition based on the box product, which is problem-independent.

$$\hat{\chi} = 2i [\Theta_i, \Theta_{i+1}] \quad (4.2)$$

Nevertheless, it is possible to observe that although this definition cannot be assumed as the "correct" one for generalized chirality in the case of an arbitrary number of particles, the scenario presented here for $N = 3$ spin-1/2 particles is indeed equivalent to the scalar spin chirality defined by the box product. This correspondence can be demonstrated by employing the commutation relations of Pauli operators and utilizing properties of the cross product. Therefore, to explicitly illustrate this relation, let us consider $\Theta_i = \Theta_1 = P_{23}$ and $\Theta_2 = P_{31}$. By doing so, it becomes apparent that the traditional definition is recovered, as depicted below.

$$\begin{aligned} \hat{\chi} &= 2i [P_{23}, P_{31}] \\ &= \frac{i}{2} [\vec{\sigma}_2 \cdot \vec{\sigma}_3, \vec{\sigma}_3 \cdot \vec{\sigma}_1] \\ &= \vec{\sigma}_1 \cdot \vec{\sigma}_2 \times \vec{\sigma}_3 \end{aligned} \quad (4.3)$$

This representation will prove useful in the upcoming sections since, in the realm of quantum operations, the chirality operator is defined as the commutation between two SWAP operations. This definition offers a simpler approach compared to the complete description involving the expansion of the box product,

which entails considering six Pauli strings.

4.2 Employing the Linear Combination of Unitaries (LCU) method for Chirality Operator Implementation

The chirality operator, as described previously, is a Hermitian operator defined as the sum of six Pauli strings or, alternatively, in terms of permutation operators, as the difference of two permutation products. However, quantum computers, by their inherent nature, can only implement unitary operations, which is not the case for the chirality operator. Therefore, directly implementing the chirality operator in a quantum computer is not possible; alternative techniques must be employed to enable its implementation. To address this challenge, a method known as the Linear Combination of Unitaries (LCU) (see Subsection 2.3.2), proposed by Childs and Wiebe [2012], can be employed.

4.2.1 Chirality Operator using LCU

The chirality operator, being Hermitian, cannot be implemented directly on a quantum computer. However, by expressing it as a combination of unitary operators, either through Pauli strings or permutation operators, the LCU method offers a viable solution. The permutation description of the chirality operator stands out for its simplicity compared to the Pauli string representation, which involves six terms. The permutation description requires only the difference of two terms, making it more resource-efficient. By utilizing the permutation description, the chirality operator can be expressed as the difference of two terms, as shown in Equation 4.4 with $R = P_{23}P_{31}$.

$$\hat{\chi} = 2i (R - R^\dagger) \quad (4.4)$$

Given that the chirality operator can be described using two unitary operators, we can employ the previously discussed example illustrated in Figure 3. By setting $U = R$ and $V = R^\dagger$. Since the desired operation is a difference, the phase to be applied in this case is $\varphi = \pi$. The ancillary register should be initialized by applying a rotation $\mathcal{O}_p = R_y(\theta)$, where $\cos^2 \theta = \sin^2 \theta = \frac{1}{2}$, which corresponds to the Hadamard operator. Therefore, $\mathcal{O}_p = H$.

Figure 22 summarizes the LCU method for applying the difference of R and R^\dagger . The probability of success can be obtained using the result derived in Equation 2.8, and it can be expressed in terms of the chirality operator as follows.

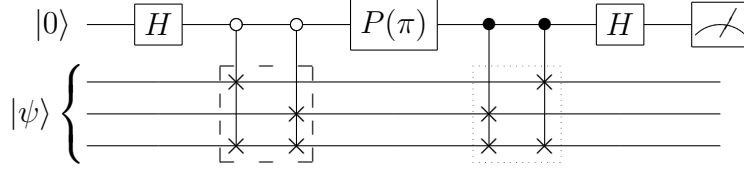


Figure 22: The figure illustrates the Linear Combination of Unitaries (LCU) method for applying the chirality operator using the permutation description in 4.4. The dashed box represents the controlled operation R , while the dotted box represents R^\dagger .

$$\begin{aligned}
 p_0 &= \frac{1}{4} \langle \psi | (R - R^\dagger)^\dagger (R - R^\dagger) | \psi \rangle \\
 &= \frac{1}{16} \langle \psi | \hat{\chi}^\dagger \hat{\chi} | \psi \rangle \\
 &= \frac{1}{16} \langle \psi | \hat{\chi}^2 | \psi \rangle
 \end{aligned} \tag{4.5}$$

As the chirality operator $\hat{\chi}$ is Hermitian $\hat{\chi}^\dagger = \hat{\chi}$, the probability of successfully applying it to a given 3-qubit state $|\psi\rangle$ is given by the expectation value of $\hat{\chi}^2$, as shown in 4.5. However, it is possible to interpret this result from another perspective. The probability of measuring the ancillary qubit in the state $|0\rangle$ is directly related to the expectation value of $\hat{\chi}^2$ for the input state $|\psi\rangle$. By performing the LCU algorithm multiple times and collecting statistical data on the probability of obtaining $|0\rangle$, we can approximate the expectation value of $\hat{\chi}^2$. This expectation value obtained using the LCU method represents the energy of the trimer Heisenberg Hamiltonian, as described in the Theoretical Background section $\mathcal{H}^{(\text{Heisenberg})} \propto \hat{\chi}^2$.

Therefore, the input states for the LCU measurement approach are prepared using the circuit shown in Figure 21, which was previously discussed in Section 3.1. Thus, the estimation of the squared chirality expectation value is obtained by simulating the circuit $N_{\text{shoots}} = 10,000$ times using a noiseless simulator provided by Qiskit. Since the variance for estimating p_0 , the probability of measuring $|0\rangle$ in the ancillary register, is bounded by $\text{Var}(p_0) \leq \frac{1}{4N_{\text{shoots}}}$, the error for measuring $\langle \hat{\chi}^2 \rangle$ is $\varepsilon = \frac{8}{\sqrt{N_{\text{shoots}}}} = 0.08$. The summary of the results is shown in Table 3.

4.3 Measuring Chirality via Hadamard Test and LCU

The previous section shows that it is possible to gain insights about a desired quantum state through indirect measurement methods. The LCU algorithm not only provides a method to implement the chirality operator but also offers an indirect approach to obtain information about the squared expectation value of chirality for a given state. Utilizing the aforementioned method, we can effectively apply the chirality operator to a desired state by leveraging an ancillary register. More importantly, for our purposes, it allows

Table 3: The table summarizes the results obtained by simulating the circuit shown in Figure 22 that apply the LCU method to estimate $\langle \hat{\chi}^2 \rangle$ for each chirality eigenstate. The error is given by $\varepsilon = \frac{8}{\sqrt{N_{shoots}}} = 0.08$, where $N_{shoots} = 10\,000$.

$ \psi\rangle$	$\langle \hat{\chi}^2 \rangle$ (exact)	$\langle \hat{\chi}^2 \rangle$ (estimated)
$ \chi = -2\sqrt{3}\rangle$	12	12.01 ± 0.08
$ \chi = 0\rangle$	0	0.00 ± 0.08
$ \chi = 2\sqrt{3}\rangle$	12	11.99 ± 0.08

us to determine if the chirality of a system is non-zero. However, the aim is to develop an algorithm that not only obtains the chirality absolute value but also distinguishes between positive, negative, and zero values.

Therefore, it is necessary to explore alternative methods that enable us to accomplish our objective. Since we already have a means to implement the chirality operator on a given state, we can explore approaches that involve measuring the outcome of the operator when applied to the state. One possible approach is to employ the Hadamard Test circuit (see Subsection 2.3.4 Cleve et al. [1998], Aharonov et al. [2006]). By leveraging the Hadamard Test in conjunction with the chirality operator implemented using the LCU method, we can estimate the chirality of a given state.

4.3.1 Combining the Hadamard Test and LCU Algorithm

Having discussed the LCU algorithm for implementing the chirality operator and separately introduced the Hadamard Test for estimating expectation values by applying the controlled version of a specific operator U , we can now combine both approaches to achieve our goal of measuring the chirality of a given state $|\psi\rangle$. This involves implementing the controlled version of the operator $U = \hat{\chi}$ using the LCU method within the framework of the Hadamard Test. Consequently, we will be able to measure the expectation value of the chirality operator using this combined approach.

However, it is important to note that the implementation of the chirality operator using the LCU method is non-deterministic, requiring the addition of another ancillary qubit as per the method's requirements. The circuit that summarizes the integration of both methods can be seen in Figure 23.

To illustrate the relationship between the measurement outcomes of the ancillary qubits and the actual expectation value of the chirality operator, let's examine the final state of the algorithm. It is worth recalling that the chirality operator can be expressed as the difference between the operator $R = P_{23}P_{31}$ and its conjugate, given by $\hat{\chi} = 2i(R - R^\dagger)$. Thus, the state after the application of the LCU in its controlled

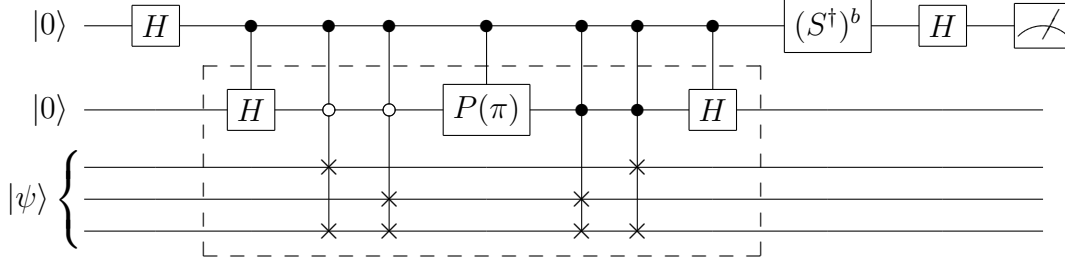


Figure 23: Circuit diagram showcasing the combined approach of the LCU algorithm and the Hadamard Test for measuring the expectation value of the chirality operator. The controlled version of the operator $\hat{\chi}$ is implemented using the LCU method (dashed box), enabling the measurement of the chirality operator's expectation value.

version C_{LCU} is depicted below.

$$\begin{aligned}
|00\psi\rangle &\xrightarrow{H\otimes\mathbb{1}\otimes\mathbb{1}} \frac{1}{\sqrt{2}} (|00\psi\rangle + |10\psi\rangle) \\
&\xrightarrow{C_{LCU}} \frac{1}{\sqrt{2}} \left[|00\psi\rangle + |1\rangle \otimes \frac{1}{2} (|0\rangle \otimes (R - R^\dagger) |\psi\rangle - |1\rangle \otimes (R + R^\dagger) |\psi\rangle) \right]
\end{aligned} \tag{4.6}$$

Therefore, as previously discussed, by measuring either in the X basis ($b = 0$) or the Y basis ($b = 1$), it becomes possible to measure the real or imaginary part of the applied operator. It is important to note that in this specific case, where the LCU method is utilized for implementing the difference between the operators R and R^\dagger , there is no requirement to measure its ancillary qubit. This is because the measurement of the qubit for the Hadamard test only provides results that are directly related to the accurate implementation of the operator $R - R^\dagger$ by the LCU. This can be observed in equations 4.7 and 4.8, where the results of measuring the Hadamard test in the X and Y basis are presented.

$$\begin{aligned}
\langle X \rangle_{\text{ancilla}} &= \frac{1}{2} \left[\langle 00\psi | + \langle 1 | \otimes \frac{1}{2} (\langle 0 | \otimes \langle \psi | (R - R^\dagger)^\dagger - \langle 1 | \otimes \langle \psi | (R + R^\dagger)^\dagger) \right] \\
&\quad X_{\text{ancilla}} \left[|00\psi\rangle + |1\rangle \otimes \frac{1}{2} (|0\rangle \otimes (R - R^\dagger) |\psi\rangle - |1\rangle \otimes (R + R^\dagger) |\psi\rangle) \right] \\
&= \frac{1}{4} \langle \psi | (R - R^\dagger) + (R - R^\dagger)^\dagger | \psi \rangle \\
&= \frac{1}{2} \text{Re} \{ \langle \psi | R - R^\dagger | \psi \rangle \} \\
&= \frac{1}{4} \text{Im} \{ \langle \psi | \hat{\chi} | \psi \rangle \}
\end{aligned} \tag{4.7}$$

Table 4: The table summarizes the results obtained by simulating the circuit shown in Figure 23 that uses the Hadamard Test and the LCU method to estimate $\langle \hat{\chi} \rangle$ for each chirality eigenstate. The error is given by $\varepsilon = \frac{4}{\sqrt{N_{shoots}}} = 0.04$, where $N_{shoots} = 10\,000$.

$ \psi\rangle$	$\langle \hat{\chi} \rangle$ (exact)	$\langle \hat{\chi} \rangle$ (estimated)
$ \chi = -2\sqrt{3}\rangle$	$-2\sqrt{3} \approx -3.46$	-3.46 ± 0.04
$ \chi = 0\rangle$	0	0.00 ± 0.04
$ \chi = 2\sqrt{3}\rangle$	$2\sqrt{3} \approx 3.46$	3.44 ± 0.04

$$\begin{aligned}
\langle Y \rangle_{\text{ancilla}} &= \frac{1}{2} \left[\langle 00\psi | + \langle 1 | \otimes \frac{1}{2} (\langle 0 | \otimes \langle \psi | (R - R^\dagger)^\dagger - \langle 1 | \otimes \langle \psi | (R + R^\dagger)^\dagger) \right] \\
Y_{\text{ancilla}} &\left[|00\psi\rangle + |1\rangle \otimes \frac{1}{2} (|0\rangle \otimes (R - R^\dagger) |\psi\rangle - |1\rangle \otimes (R + R^\dagger) |\psi\rangle) \right] \\
&= \frac{1}{2} \text{Im} \{ \langle \psi | R - R^\dagger | \psi \rangle \} \\
&= \frac{1}{4} \text{Re} \{ \langle \psi | \hat{\chi} | \psi \rangle \}
\end{aligned} \tag{4.8}$$

The first important observation regarding these calculations is that implementing the operator to estimate its expectation value using the LCU method introduces a factor of $\frac{1}{2}$, which differs from the general derivation presented earlier. Additionally, it should be noted that the presence of an imaginary factor multiplying the implemented operator $R - R^\dagger$ via LCU results in the measurement of the imaginary part of the expectation value of the chirality operator when measured in the X basis, and the measurement of the real part when measured in the Y basis.

The combination of the Hadamard test with the LCU method for applying the chirality operator enables the estimation of the chirality of a given input state. To evaluate the results of the circuit, let's consider the chirality eigenstates as the input and estimate their chirality by measuring the Y ($b = 1$) operator since all the eigenvalues of this operator are real. The error of the estimation should be bounded by the number of estimation trials, denoted as $N_{shoots} = 10,000$, with an error bound of $\varepsilon = \frac{4}{\sqrt{N_{shoots}}} = 0.04$ obtained through the variance of measuring one Pauli operator $\text{Var}(\langle Pauli \rangle) = \frac{1}{N_{shoots}}$. The estimation results, compared with the theoretical values, are presented in Table 4.

In this study, two methods were investigated: the LCU method for implementing non-unitary operators that can be decomposed into a linear combination of unitary operators, and the Hadamard test for estimating expectation values. Although these methods were specifically applied to estimate the chirality operator, which is a Hermitian operator, it is evident that both approaches have broader applicability and can be utilized to measure expectation values for other operators as well. However, it is important to note

that the results obtained for the chirality operator using the Hadamard test and the LCU method (see Equations 4.7 and 4.8) differ from the results obtained for the Hadamard test of unitary operators that do not require the LCU method for implementation (see Equations 2.16 and 2.17).

4.4 Time Evolution Chirality Operator

The previous discussion focused on measuring the chirality of a given state by applying the chirality operator to the state. The upcoming approaches will address the problem of chirality measurement by utilizing the time evolution of the chirality operator.

To simplify future results, let's consider the normalized version of the chirality operator, where the eigenvalues are $0, \pm 1$. The normalized chirality operator is defined as:

$$\hat{\chi} = \frac{1}{2\sqrt{3}} \vec{\sigma}_1 \cdot \vec{\sigma}_2 \times \vec{\sigma}_3 = \frac{i}{\sqrt{3}} [P_{23}, P_{31}] \quad (4.9)$$

The time evolution of the chirality operator is obtained by exponentiating it, as defined in Equation 2. Therefore, in order to implement this unitary operator on a quantum computer, it needs to be expressed in terms of quantum operations permitted in such a system. The usual approach, which was discussed subsection 2.3.1, involves using the Trotterization method to approximate the desired evolution.

$$U_{\chi}(t) = e^{-i\hat{\chi}t} \quad (4.10)$$

The chirality operator can be decomposed into six Pauli strings using the expansion of the box product formula, as shown in Equation 4.11. Therefore, as discussed in the theoretical background, the Trotter-Suzuki formula enables the approximation of the evolution over a time period t by expanding the exponential of the six Pauli strings in terms of the individual exponentials of each. This approximation is achieved by dividing the time interval into smaller steps of $\Delta t = t/n$, where n represents the number of steps as was shown in Equation 2.5.

$$\hat{\chi} = \frac{XYZ + YZX + ZXY - XZY - YXZ - ZYX}{2\sqrt{3}} \quad (4.11)$$

Due to the large number of terms involved, it can be observed that even with just one Trotter layer, the number of quantum operations required is significant. Additionally, it is important to note that this method only provides an approximation of the total evolution and does not correspond to an exact implementation. However, since the objective is not to implement the time evolution operator for an arbitrary time interval,

but rather to utilize this dynamics to estimate the chirality of a specific state, it is possible to analyze the operation in order to find a more efficient approach that takes advantage of the problem's characteristics.

Therefore, let's consider expressing the chirality operator in terms of the cyclical permutation operator $R = P_{23}P_{31}$ and its Hermitian conjugate R^\dagger . Since the subsequent analysis of $U_\chi(t)$ will be conducted using its Taylor expansion, the equations below demonstrate the expansions for the square and cube of the chirality operator.

The square of the chirality operator:

$$\begin{aligned}\hat{\chi}^2 &= -\frac{1}{3} (R^2 + (R^\dagger)^2 - 2) \\ &= -\frac{1}{3} (R + R^\dagger - 2)\end{aligned}\tag{4.12}$$

The cube of the chirality operator:

$$\begin{aligned}\hat{\chi}^3 &= -\frac{i}{3\sqrt{3}} (R + R^\dagger - 2) (R - R^\dagger) \\ &= -\frac{i}{3\sqrt{3}} (R^2 - (R^\dagger)^2 - 2R + 2R^\dagger) \\ &= -\frac{i}{3\sqrt{3}} (R^\dagger - R - 2R + 2R^\dagger) \\ &= \frac{i}{\sqrt{3}} (R - R^\dagger) \\ &= \hat{\chi}\end{aligned}\tag{4.13}$$

In the equations, it was utilized the property that $R^2 = R^\dagger$ and $(R^\dagger)^2 = R$, which can be easily confirmed by observing the effect of these operators on a state. Additionally, an interesting result arises from this property, namely, the cube of the chirality operator is equal to the chirality operator itself. Hence, the Taylor expansion of $U_\chi(t)$ is as follows:

$$\begin{aligned}U_\chi(t) &= e^{-i\hat{\chi}t} = \sum_{k=0}^{\infty} \frac{(-it)^k}{k!} \hat{\chi}^k \\ &= 1 + (\cos t - 1) \hat{\chi}^2 - i \sin t \hat{\chi}\end{aligned}\tag{4.14}$$

By expanding the chirality operator in terms of the operators R and R^\dagger , the following relation can be obtained:

$$\begin{aligned}U_\chi(t) &= 1 - \frac{1}{3} (\cos t - 1) (R + R^\dagger - 2) + \frac{1}{\sqrt{3}} \sin t (R - R^\dagger) \\ &= \frac{1}{3} + \frac{2}{3} \cos t + \left(\frac{1}{\sqrt{3}} \sin t - \frac{1}{3} (\cos t - 1) \right) R - \left(\frac{1}{\sqrt{3}} \sin t + \frac{1}{3} (\cos t - 1) \right) R^\dagger\end{aligned}\tag{4.15}$$

Therefore, by setting the time $t = \frac{2\pi}{3}$, it becomes apparent that the time evolution operator for chirality simplifies to the cyclical permutation operator R .

$$U_\chi\left(\frac{2\pi}{3}\right) = R \quad (4.16)$$

The relationship between $U_\chi(t)$ and the specific time $t = \frac{2\pi}{3}$ allows for a more straightforward implementation of this operator on quantum computers. Since the operator R is simpler to implement compared to the Trotterization of $U_\chi(t)$, the upcoming algorithms will utilize this implementation. Indeed, it is important to emphasize that the main objective is to measure the chirality of a given state, rather than implementing the operator for arbitrary times. In this context, the simplified implementation using the operator R becomes highly valuable and practical.

4.5 Using Quantum Phase Estimation (QPE) for Chirality Determination

As discussed in the previous section, a straightforward method was presented for implementing the chirality time evolution operator $U_\chi(t)$ by wisely selecting the time interval as $t = \frac{2\pi}{3}$. Consequently, the eigenvalues of this operator would be given by $e^{-i\frac{2\pi}{3}\lambda}$, where the corresponding chirality eigenstates are labeled as $|\chi = \lambda\rangle$ with $\lambda = 0, \pm 1$. To estimate the phase of this unitary operation, a commonly used approach is the Quantum Phase Estimation (QPE) algorithm (see Subsection 2.3.5 [Abrams and Lloyd \[1999\]](#)).

This algorithm utilizes an ancillary register consisting of n qubits to estimate the phase ϕ of a given eigenvalue $e^{i2\pi\phi}$. The best estimation of $2^n\phi$, denoted as $\varphi \in \mathbb{Z}^+$, is encoded in the state $|\varphi\rangle$ obtained after measuring the ancillary register. The probability of measuring the best estimation φ is lower bounded by $P(\varphi) \geq \frac{4}{\pi^2}$ [Cleve et al. \[1998\]](#). Since the eigenvalues of the chirality operator are also encoded in exponential form $e^{-i\frac{2\pi}{3}\lambda}$, the QPE approach can be employed to estimate these values.

By comparing the $U_\chi(\frac{2\pi}{3})$ eigenvalues $e^{-i\frac{2\pi}{3}\lambda}$ with the exponential form $e^{i2\pi\phi}$ estimated in the QPE algorithm, we can determine the value to be estimated using this approach, which is $\phi = -\frac{\lambda}{3} \in \{0, \pm\frac{1}{3}\}$. It is important to note that when $\lambda = -1$, we have $\phi = \frac{1}{3}$. As shown in the previous example in the QPE Subsection 2.3.5, this value cannot be exactly measured for any arbitrary number of n qubits in the ancillary register because it does not have a finite binary fraction representation. Increasing the number of qubits in the ancillary register only increases the resolution of the approximation $\varphi \approx 2^n \cdot \frac{1}{3}$. On the other hand, when $\lambda = 1$, we have $\phi = -\frac{1}{3}$, which is a negative value. However, the QPE method only

estimates positive integer values of $\varphi \approx 2^n \phi$. Therefore, the value that would be obtained through QPE by utilizing the periodicity of the complex exponential is $e^{i(2\pi - \frac{2\pi}{3}\lambda)} = e^{-i\frac{2\pi}{3}\lambda}$. Consequently, when $\lambda = 1$, the value to be estimated is $\phi = 1 - \frac{1}{3} = \frac{2}{3}$. Once again, this value cannot be exactly represented by a binary integer φ .

As observed, there is no specific number of qubits, denoted as n , for which the values of λ can be exactly obtained using the Quantum Phase Estimation (QPE) method. However, the objective of utilizing the QPE algorithm is to have a reliable method to distinguish between the three values of λ , namely $\lambda \in \{0, \pm 1\}$. To achieve this objective, it is crucial to determine the minimum number of qubits needed in the ancillary register to effectively discriminate between the eigenvalues.

To effectively distinguish between the three possible outcomes of the QPE algorithm, namely $\phi \in \{0, \frac{1}{3}, \frac{2}{3}\}$, it is crucial that the separation between the outcomes must be significant enough to allow for accurate discrimination. Therefore, the number of qubits n required can be determined using the following expression:

$$\begin{aligned} \log_2 \frac{1}{2^n} &= \left\lceil \log_2 \left(\frac{1}{3} \right) \right\rceil \\ n &= \lceil \log_2 3 \rceil = 2 \end{aligned} \quad (4.17)$$

To distinguish between the three possible outcomes of φ , a total of $n = 2$ qubits is required. With this configuration, we can proceed to calculate the probability of accurately estimating the value of $\phi = \frac{1}{3}$ when $\lambda = -1$ using the Equation 2.20. First, let's determine the nearest integer to the correct solution and calculate its deviation δ using the following equation:

$$\begin{aligned} 2^n \phi &= 2^2 \frac{1}{3} \xrightarrow{\text{Binary}} 2^2 0.0101 \dots = 01 + 0.0101 \dots \\ &= \varphi + 2^2 \delta \end{aligned} \quad (4.18)$$

Therefore, the nearest integer to the correct solution is $\varphi = 1$, which in binary representation is 01. The deviation δ can be represented as $\delta = \frac{1}{12}$, which in binary fraction is 0.0001010... Consequently, we can calculate the probability of obtaining the correct solution as follows:

$$\begin{aligned} P(\varphi = 1) &= \left(\frac{1 \sin \frac{\pi}{3}}{4 \sin \frac{\pi}{12}} \right)^2 \\ &\approx 0.70 \end{aligned} \quad (4.19)$$

The probability of correctly measuring the state $|01\rangle$, which corresponds to the value that best approximates the actual value of $\phi = \frac{1}{3}$, is approximately $P(\varphi = 1) \approx 0.70$. Similarly, for measuring $\phi = \frac{2}{3}$, the nearest integer is the value of $\varphi = 3$, represented in binary as 11, with a deviation of $\delta = \frac{1}{12}$ such that

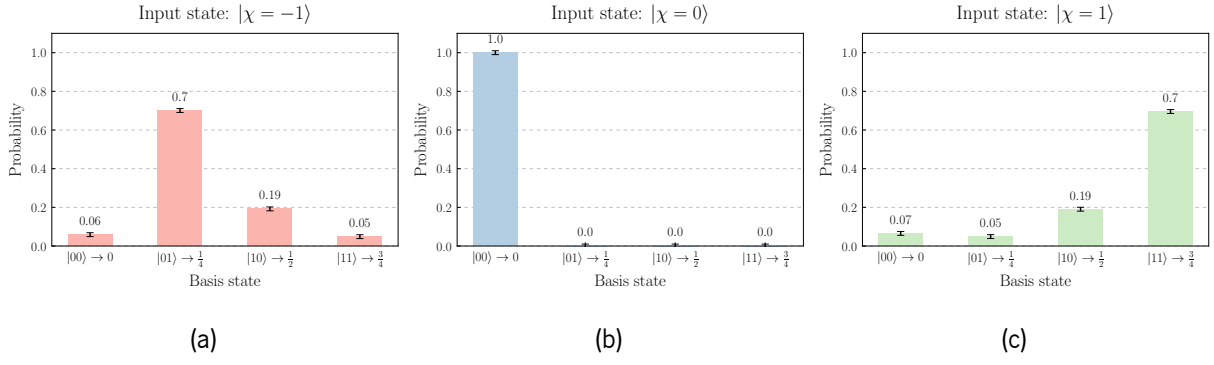


Figure 24: The figure displays the probabilities of measuring each basis state of $n = 2$ qubits using the QPE algorithm, obtained through a noiseless simulation using Qiskit. The simulation consisted of $N_{\text{shoots}} = 2,500$ runs to estimate the probabilities with an error of $\varepsilon = 0.01$, represented in the figure by error bars. Figure 24a shows the probability estimation using the chirality eigenstate $|\chi = -1\rangle$ as the input, figure 24b corresponds to $|\chi = 0\rangle$, and figure 24c corresponds to $|\chi = 1\rangle$. The x-axis of each figure also represents the corresponding values of $\frac{\phi}{2^2}$. The chirality eigenvalue was estimated by considering the state with the highest probability (see Table 5).

$2^2 \phi = \varphi - 2^2 \delta$. The probability of correctly measuring this value is approximately $P(\varphi = 3) \approx 0.70$. Conversely, since $2^n \phi = 0$ can be exactly represented with $n = 2$ qubits as $\varphi = 0$, the probability of correctly measuring this value is $P(\varphi = 0) = 1$.

Therefore, the error in the estimation of ϕ is bounded by $\delta_{\text{max}} = \frac{1}{2^{n+1}} = 0.125$. Consequently, the estimation of $\chi = \lambda$ is subject to an error bounded by $\epsilon = 3\delta_{\text{max}} = 0.375$. To validate these results through a noiseless Qiskit simulation, we conducted $N_{\text{shoots}} = 2,500$ runs to obtain an estimation error on the probability $P(\varphi)$ of $\varepsilon = \frac{1}{2\sqrt{N_{\text{shoots}}}} = 0.01$. The input states used in the simulation were the chirality eigenstates discussed in section 3.1 and previously employed to test the other methods. The measured probabilities for each input state are depicted in Figure 24, and the estimated eigenvalues are presented in Table 5. The obtained results are consistent with the expected outcomes.

The previous results showed the minimum resources required to distinguish between the three possible eigenstates $\chi \in 0, \pm 1$. To obtain a more precise estimation using the Quantum Phase Estimation (QPE) algorithm, let's add more qubits to the ancillary register. With $n = 5$ qubits, the maximum error in the estimated value of ϕ is $\delta_{\text{max}} = \frac{1}{2^{n+1}} \approx 0.02$, and the error in the chirality estimation is $\epsilon = 3\delta_{\text{max}} \approx 0.05$. The results are summarized in Table 6.

Table 5: Estimated eigenvalues $\chi = \lambda$ using QPE. The estimation error is limited by the precision determined by the number of qubits. With $n = 2$ qubits, the binary fraction error is bounded by $\delta_{\max} = \frac{1}{2^{n+1}} = 0.125$. Consequently, the chirality estimation error is $\epsilon = 3\delta_{\max} = 0.375$. The measured value of $\frac{\phi}{2^2}$, providing the best approximation of the binary fraction representing $\phi = -\frac{\lambda}{3}$, was obtained by selecting the result with the highest probability from simulations with different input states (see Figure 24).

Input State	Measured $\frac{\phi}{2^2}$	Estimated χ
$ \chi = -1\rangle$	0.2 ± 0.1	-0.8 ± 0.4
$ \chi = 0\rangle$	0.0 ± 0.1	0 ± 0.4
$ \chi = 1\rangle$	0.8 ± 0.1	0.8 ± 0.4

Table 6: Estimated eigenvalues $\chi = \lambda$ using QPE with $n = 5$ qubits. The estimation error is limited by the precision determined by the number of qubits. With $n = 5$ qubits in the ancillary register, the maximum error in the estimated value of ϕ is $\delta_{\max} = \frac{1}{2^{n+1}} \approx 0.02$. Consequently, the error in the chirality estimation is $\epsilon = 3\delta_{\max} \approx 0.05$. The table summarizes the results obtained for the estimated eigenvalues using the enhanced QPE setup.

Input State	Measured $\frac{\phi}{2^5}$	Estimated χ
$ \chi = -1\rangle$	0.34 ± 0.02	-1.03 ± 0.05
$ \chi = 0\rangle$	0.00 ± 0.02	0.00 ± 0.05
$ \chi = 1\rangle$	0.65 ± 0.02	1.03 ± 0.05

4.5.1 QPE with Qutrits

Another alternative to address the issue of encoding the values $\phi = \frac{1}{3}$ ($\chi = -1$) and $\phi = \frac{2}{3}$ ($\chi = 1$) in binary fractions is to utilize a qutrit, which is a quantum system with 3-level quantum states, in the ancillary register. By employing a qutrit, it becomes possible to precisely encode the potential outcomes since they can be represented exactly in terms of ternary fractions, with $3^1\phi \in \{0, 1, 2\}$. While our focus for this problem is on qutrits, it is important to note that this concept can be extended to the use of qudits, which are quantum systems with d -level quantum states, either in the ancillary register or the main register. This extension has been discussed by [Tonchev and Vitanov \[2016\]](#).

One notable change when transitioning from QPE with qubits to qutrits is the preparation of the ancillary register. In the case of qubits, Hadamard gates are used for this purpose. However, for qutrits, the

equivalent operation is the application of a one-qutrit Quantum Fourier Transform (QFT_3), as depicted in the equation below. Similarly, the final transformation is accomplished using the adjoint of the QFT_3 , denoted as QFT_3^\dagger .

$$QFT_3 = \frac{1}{\sqrt{3}} \begin{pmatrix} 1 & 1 & 1 \\ 1 & \omega & \omega^2 \\ 1 & \omega^2 & \omega \end{pmatrix} \quad QFT_3^\dagger = \frac{1}{\sqrt{3}} \begin{pmatrix} 1 & 1 & 1 \\ 1 & \omega^2 & \omega \\ 1 & \omega & \omega^2 \end{pmatrix}, \quad \omega = e^{i\frac{2\pi}{3}} \quad (4.20)$$

In the case of using qutrits, the controlled unitary operation $U_\chi \left(\frac{2\pi}{3}\right)$, also known as oracles $\mathcal{O}(U_\chi)$, involves a qutrit as the control. The state $|k\rangle$, $k \in \{0, 1, 2\}$ is used to control the application of the corresponding power of U_χ^k to the main register, which encodes the input state $|\chi\rangle$ using qubits.

$$\mathcal{O}(U_\chi) |k\rangle \otimes |\chi\rangle = e^{-i\frac{2k\pi}{3}\chi} |k\rangle \otimes |\chi\rangle \quad (4.21)$$

The final state of the Quantum Phase Estimation (QPE) algorithm with the ancillary qutrit, when applied to a chirality eigenstate $|\chi\rangle$ as input, can be described by the following equations. Please note that the label $|\rangle_d$ indicates that the state is encoded using a qudit.

$$\begin{aligned} |0\rangle_3 \otimes |\chi\rangle_2 &\xrightarrow{QFT_3} \frac{1}{\sqrt{3}} (|0\rangle_3 + |1\rangle_3 + |2\rangle_3) \otimes |\chi\rangle_2 \\ &\xrightarrow{\mathcal{O}(U_\chi)} \frac{1}{\sqrt{3}} \left(|0\rangle_3 + e^{-i\frac{2\pi}{3}\chi} |1\rangle_3 + e^{-i\frac{4\pi}{3}\chi} |2\rangle_3 \right) \otimes |\chi\rangle_2 \\ &\xrightarrow{QFT_3^\dagger} \begin{cases} |0\rangle_3 \otimes |\chi\rangle_2 & \text{if } \chi = 0 \\ |1\rangle_3 \otimes |\chi\rangle_2 & \text{if } \chi = -1 \\ |2\rangle_3 \otimes |\chi\rangle_2 & \text{if } \chi = 1 \end{cases} \end{aligned} \quad (4.22)$$

Indeed, the result can be easily observed since ω and ω^2 are the cube roots of unity and satisfy the relation $1 + \omega + \omega^2 = 0$. This relationship leads to a circuit modification in the QPE that enables the discrimination of the chirality eigenvalue with a single measurement. In this modified version, the probability of successfully measuring the correct value is always $P(\varphi) = 1$ for all possible chirality eigenstates as input. This demonstrates the effectiveness of utilizing a qutrit-based encoding and the resulting circuit structure in achieving accurate and deterministic measurements of the chirality eigenvalue.

On the other hand, if the input state is a general state $|\psi\rangle$, this circuit allows for the estimation of the chirality expectation value $\langle\psi|\hat{\chi}|\psi\rangle$ by computing the probabilities of measuring each qutrit basis state. The final state of the ancillary register is directly related to the chirality distribution of the state $|\psi\rangle$. Specifically, the probability of measuring $|0\rangle$ in the ancillary register is directly related to the probability

of measuring the state $|\psi\rangle$ with $\chi = 0$, while the probabilities of measuring $|1\rangle$ and $|2\rangle$ correspond to the chirality eigenvalues $\chi = -1$ and $\chi = 1$, respectively. The chirality expectation value can then be calculated as follows:

$$\langle\psi|\hat{\chi}|\psi\rangle = P(\varphi = 2) - P(\varphi = 1) \quad (4.23)$$

Moreover, if the input state $|\psi\rangle$ is a linear combination of states with different chirality, applying the QPE with the qutrit ancillary register will result in the collapse of the wavefunction into a single chirality eigenstate, with the specific chirality indicated by the measurement outcome. Therefore, this circuit provides a means to initialize states with well-defined chirality, similar to recently proposed algorithms for preparing valence-bond-solid states [Murta et al. \[2023\]](#) and the Gutzwiller wave function [Murta and Fernández-Rossier \[2021\]](#).

4.6 Assessing Chirality using the Cycle Test

This section will discuss a final method to probe chirality over a given input state $|\psi\rangle$. First, according to the result provided by equation 4.14, $U_\chi(t)$ can be expressed in terms of a real and imaginary part. Additionally, let's recall the definition of the time evolution operator $U_\chi(t = \frac{2\pi}{3}) = R$ for the specific time $t = \frac{2\pi}{3}$ (see Section 4.4). This operator is straightforward to implement in a quantum computer since it is composed of just two qubit permutations $R = P_{23}P_{31}$. Therefore, the equation below shows the combination of both definitions.

$$U_\chi\left(t = \frac{2\pi}{3}\right) = 1 - \frac{3}{2}\hat{\chi}^2 - i\frac{\sqrt{3}}{2}\hat{\chi} = R \quad (4.24)$$

The equation above shows that the operator R is directly related to the chirality operator, as its real part is formed by $\hat{\chi}^2$ and its imaginary part by $\hat{\chi}$. Consequently, the expectation value of this operator for an arbitrary state can be expressed as equation 4.25. In this dissertation work, a circuit has already been presented to measure either the real or imaginary part of a given unitary operator, known as the Hadamard test. Therefore, it is possible to perform the Hadamard test on the operator R to obtain the chirality of a given input state $|\psi\rangle$. The circuit can be seen in Figure 25.

$$\langle\psi|R|\psi\rangle = 1 - \frac{3}{2}\langle\psi|\hat{\chi}^2|\psi\rangle - i\frac{\sqrt{3}}{2}\langle\psi|\hat{\chi}|\psi\rangle \quad (4.25)$$

The algorithm used in the Hadamard test, which involves a cyclical permutation operator, is referred to as the cycle test. It was recently proposed by [Oszmaniec et al. \[2021\]](#) as a method for measuring the

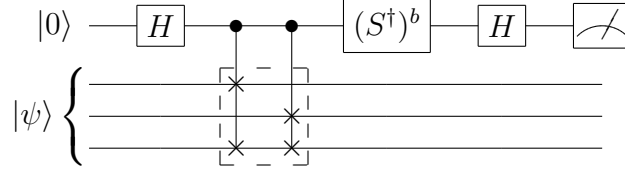


Figure 25: The figure depicts the Hadamard test for the unitary operator $U_\chi \left(\frac{2\pi}{3} \right) = R$, indicated by the dashed box. As mentioned in the main text (see Subsection 2.3.4), when measured in the Y basis ($b = 1$), the result corresponds to the imaginary part of the unitary operator R , which in this case gives $\langle \psi | \hat{\chi} | \psi \rangle$ (see Equation 4.25). On the other hand, the measurement in the X basis ($b = 0$) captures the real part of R , which is associated with $\langle \psi | \hat{\chi}^2 | \psi \rangle$ (see Equation 4.25).

unitary invariant properties of a set of states, which characterize their relative geometrical orientation. The relationship between these properties will be further explored in the next chapter. By measuring the ancilla in the Y (X) basis with $b = 1$ ($b = 0$), it becomes possible to obtain $\langle \psi | \hat{\chi} | \psi \rangle$ ($\langle \psi | \hat{\chi}^2 | \psi \rangle$) as shown below.

$$\begin{aligned} \langle \psi | \hat{\chi} | \psi \rangle &= -\frac{2}{\sqrt{3}} \langle Y_{ancilla} \rangle \\ \langle \psi | \hat{\chi}^2 | \psi \rangle &= \frac{2}{3} (1 - \langle X_{ancilla} \rangle) \end{aligned} \quad (4.26)$$

Similarly to the previous methods, this method was also tested using Qiskit, with the input being the chirality eigenstates we have been using. The noiseless simulation involved $N_{shots} = 10,000$ trials to obtain an estimation in the Pauli expectation value with an error bound of $\varepsilon = \frac{1}{\sqrt{N_{shots}}}$. Consequently, the bounded errors for $\langle \hat{\chi} \rangle$ and $\langle \hat{\chi}^2 \rangle$ are $\epsilon_\chi = \frac{2}{\sqrt{3}}\varepsilon$ and $\epsilon_{\chi^2} = \frac{2}{3}\varepsilon$, respectively. The results of these simulations are presented in Table 7, and as expected, the correct outcomes were obtained.

Table 7: The table shows the results of the noiseless simulation of the cycle test (see Figure 25), for the chirality eigenstates as input. The estimation was obtained with $N_{shots} = 10,000$ trials. The error bounds for the chirality and chirality squared are $\epsilon_\chi = \frac{2}{\sqrt{3}N_{shots}} \approx 0.01$ and $\epsilon_{\chi^2} = \frac{2}{3} \frac{1}{\sqrt{N_{shots}}} \approx 0.007$, respectively.

$ \psi\rangle$	χ (estimated)	χ^2 (estimated)
$ \chi = -1\rangle$	-1.01 ± 0.01	0.993 ± 0.007
$ \chi = 0\rangle$	-0.01 ± 0.01	0.000 ± 0.007
$ \chi = 1\rangle$	0.99 ± 0.01	0.999 ± 0.007

4.7 Selecting the Best Approach

This chapter was dedicated to presenting all the methods proposed for estimating the chirality of a given input state $|\psi\rangle$ using alternatives to conventional quantum tomography. All of these methods were tested using the chirality eigenstates prepared in the previous chapter (see Chapter 3), and as expected, they all enabled the determination of chirality. However, not all of the proposed approaches are suitable for NISQ devices due to the required resources. In this section, we aim to compare the methods based on the number of gates, depth, ancillary qubits required, and the number of trials needed to achieve a certain precision ε in the estimation. This comparison will help us choose the most suitable approach for the chirality test and also describe the advantages and limitations of each method.

The comparison in terms of the number of gates for both one-qubit and two-qubit operations, specifically the count of CNOT gates for the two-qubit operations, as well as the circuit depth was conducted as follows: Firstly, the circuits built in Qiskit were decomposed into the basic gates that can be handled by the Python tool PyZx [Kissinger and van de Wetering \[2020\]](#). Then, the quantum circuit instructions were transformed into the Open Quantum Assembly Language (QASM) [Cross et al. \[2017\]](#), which can be understood by the PyZx module. This procedure was performed to utilize the PyZx library to optimize the circuits. By using the *basic_optimization* function provided by the PyZx module, the circuits were optimized. This ensures that the comparison is made in a fair manner. The statistics of each circuit were then obtained for this comparison (see Table 8).

Table 8: The table presented below provides an overview of the resources needed for performing the chirality estimation. It compares the number of ancillary qubits, circuit depth, and the total number of gates. Specifically, the count of CNOT gates is explicitly displayed.

Methods	Number of Ancillas	Depth	Number of Gates	CNOT count
LCU	1	50	66	27
HT + LCU	2	123	142	66
QPE ($n = 2$)	2	82	116	47
QPE ($n = 5$)	5	793	1115	460
Cycle Test	1	26	36	14

The application of the chirality operator using the LCU method (see Section 4.2), which we will simply refer to as LCU for simplicity, is intended to implement non-unitary operators using a probabilistic approach. However, it has been observed that by repeating the process, the squared chirality operator

can be estimated. It should be noted that while the goal of this chapter is to develop a circuit that estimates chirality, this approach does not achieve that objective. As a result, this method is excluded from the comparison. Nonetheless, statistics using PyZx were computed for the LCU method. Although the LCU method cannot be used to measure chirality directly, it does provide a means to apply the chirality operator to a given state, as utilized in the combined approach of the Hadamard test and LCU (HT+LCU) (see Section 4.3).

The other methods discussed in this chapter enable chirality estimation, although not all of them can estimate the chirality of an arbitrary state. For example, the Quantum Phase Estimation (QPE) method (see Section 4.5) only provides an estimation with a certain probability of success for a given chirality input state, and the precision of the estimation depends on the number of ancillary qubits. The main advantage of this method lies in using a qutrit as an ancilla (see Subsection 4.5.1), which transforms the circuit into a qutrit Hadamard test functioning as a QPE. As demonstrated earlier, this approach allows for either the deterministic single-shot determination of chirality when the input state is a chirality eigenstate, the preparation of states with known chirality, or the estimation of chirality by estimating the probability of each outcome. However, since our goal is to design a circuit that utilizes only qubits to operate on digital NISQ devices, the qutrit QPE is not the optimal approach.

Moreover, the other comparison mentioned at the beginning of this section is related to the precision of the estimation. It aims to determine which algorithm achieves a better precision with fewer resources. This comparison will consider the number of ancillary qubits and the number of trials required to obtain the chirality estimation with a bounded error of ε .

The HT + LCU method requires a constant number of two ancillary qubits, and the number of shots, denoted by N_{shots} , scales with $\mathcal{O}\left(\frac{1}{\varepsilon^2}\right)$ in order to achieve the desired precision. On the other hand, the QPE methods only estimate the chirality for the chirality eigenstates with a certain probability, but not for general input states. The precision of the QPE method depends on the number of ancillary qubits, denoted by n , and scales with $\mathcal{O}\left(\log_2 \frac{1}{\varepsilon}\right)$. Lastly, the cycle test requires a constant number of ancillary qubits, and the number of runs needed scales with $\mathcal{O}\left(\frac{1}{\varepsilon^2}\right)$. The exact number of resources required to estimate the chirality with a desired precision of $\varepsilon = 0.01$ is summarized in Table 9.

Indeed, the cycle test approach appears to be the best method for probing chirality, as it achieves the goal with fewer resources, including the number of ancillary qubits, circuit depth, and CNOT count. The reduction in the number of CNOT gates is particularly important as multi-qubit operations can introduce errors due to the physical interactions between qubits Mötönen et al. [2004]. The cycle test method achieves the desired goal with a circuit depth of 26 and a CNOT count of 14, achieved by decomposing 7

Table 9: The table below compares the number of ancillary qubits and the number of shots N_{shots} required to obtain the chirality estimation with a bounded error of $\varepsilon = 0.01$. For the QPE method, the number of shots is associated with a probability of obtaining the correct result in a single shot, and this probability is explicitly stated in the table.

Methods	Number of Ancillas	N_{shots}
HT + LCU	2	$\frac{4}{\varepsilon^2} = 160,000$
QPE	$\log_2 \frac{1}{\varepsilon} - 1 \approx 4$	1 with a probability of success of 70%
Cycle Test	1	$\frac{4}{3\varepsilon^2} \approx 13,334$

CNOT gates for each Fredkin gate, as described by [Cruz and Murta \[2023\]](#).

Furthermore, the cycle test method allows for the estimation of the chirality expectation value for a general input state with better precision and fewer trials (N_{shots}) and ancillas compared to other methods. Therefore, considering both the reduction in resources and the improved precision, it is evident that the cycle test algorithm is the most suitable approach for probing chirality.

Chapter 5

Chirality in Spin Models

In Chapter 4, a quantum circuit was developed to measure the chirality expectation value of a given input state. As discussed in that chapter, the cycle test is considered the most effective approach to achieve this goal. The results of the cycle test were tested using the chirality eigenstates prepared in Chapter 3. However, there are other cases that provide more interesting descriptions when it comes to chirality. For example, in classical magnetism, chirality characterizes non-coplanar spin textures. In quantum magnetism, it serves as an order parameter for chiral spin liquids, and in quantum information, spin chirality acts as a witness of genuine tripartite entanglement. Therefore, the purpose of this chapter is to explore other spin models where the chirality can probe these intriguing results by utilizing the cycle test.

5.1 Broken symmetry magnetism and Bargmann invariants

In broken symmetry magnetism, the behavior of spins can be effectively described using vectors. In the context of broken symmetry magnetism, these vectors can also be represented as product states. For spin- $\frac{1}{2}$ systems, these product states correspond to vectors located on the Bloch sphere. Therefore, for the purpose of this section, the focus will be on considering product states of coherent spin states. These states are eigenstates of the spin operator and can be described classically by $\vec{m} = S\vec{n}$, where S represents the spin value, which in this case is $S = \frac{1}{2}$. The unit vector \vec{n} , as shown in Figure 26a, characterizes the orientation of the spin and is defined by the equation below.

$$\vec{n} = \cos \varphi \sin \theta \hat{x} + \sin \varphi \sin \theta \hat{y} + \cos \theta \hat{z} \quad (5.1)$$

To determine the classical chirality of the trio of spins denoted as i, j , and k , represented as χ_{ijk}^{class} , one can calculate the scalar triple product of the unitary vectors that characterize each spin. This computation yields a measure of the non-coplanarity of the spin vectors, which is captured by the classical chirality.

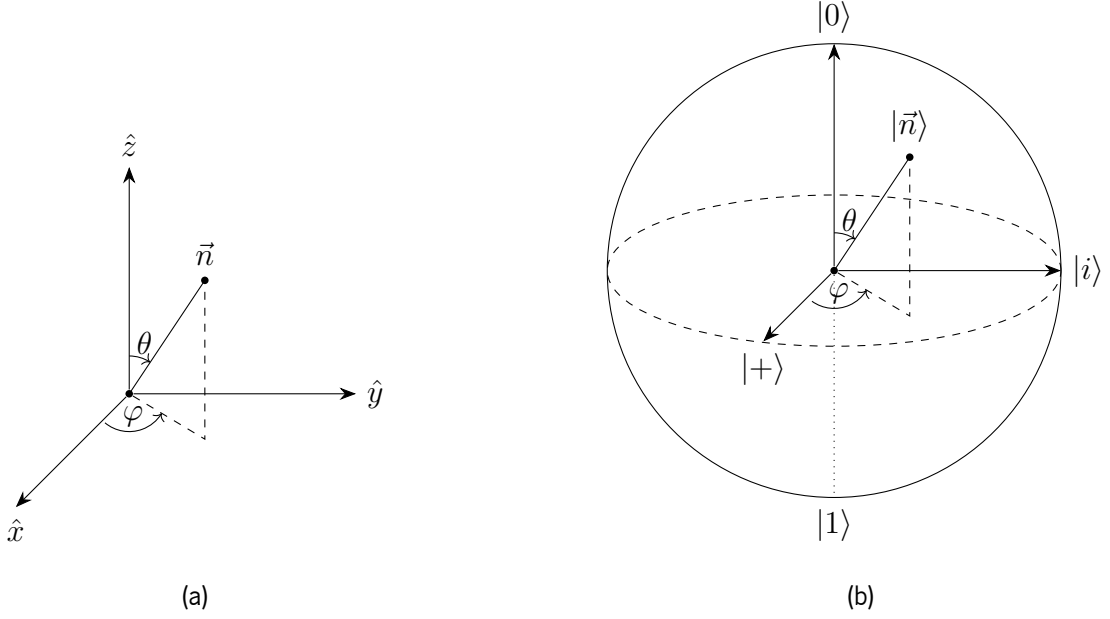


Figure 26: Figure 26a illustrates the schematic representation of the unitary vector \vec{n} characterized by the polar angle φ and azimuthal angle θ . Additionally, Figure 26b depicts a schematic representation of a general coherent state $|\vec{n}\rangle$ in the Bloch sphere, demonstrating the relationship between the state and the classical vector \vec{n} .

$$\chi_{ijk}^{class} = \frac{4S^3}{\sqrt{3}} \vec{n}_i \cdot \vec{n}_j \times \vec{n}_k \quad (5.2)$$

On the other hand, for the case of $S = \frac{1}{2}$, the spin states can be represented as vectors in the Bloch sphere, commonly referred to as Bloch states. Figure 26b illustrates a general coherent state $|\vec{n}\rangle$ in the Bloch Sphere, where \vec{n} represents the classical vector defined earlier.

$$|\vec{n}\rangle = \cos \frac{\theta}{2} |0\rangle + e^{i\varphi} \sin \frac{\theta}{2} |1\rangle \quad (5.3)$$

Therefore, broken-symmetry magnetism can be described in terms of product states utilizing these Bloch states. In this case, the broken-symmetry state $|\Psi\rangle_{br.symm.}$ can be represented as a product of N coherent states, as shown in Equation 5.4.

$$|\Psi\rangle_{br.symm.} = |\vec{n}_1\rangle \otimes |\vec{n}_2\rangle \otimes \cdots \otimes |\vec{n}_N\rangle \quad (5.4)$$

Consequently, it becomes possible to calculate the expectation value of the quantum scalar chirality operator for the trios of spins i , j , and k in the broken-symmetry state $|\Psi\rangle_{br.symm.}$, as shown below.

$$\begin{aligned}
\langle \Psi_{br.symm.} | \hat{\chi} | \Psi_{br.symm.} \rangle &= \frac{1}{2\sqrt{3}} \langle \Psi_{br.symm.} | \vec{\sigma}_i \cdot \vec{\sigma}_j \times \vec{\sigma}_k | \Psi_{br.symm.} \rangle \\
&= \frac{\varepsilon^{\mu\nu\eta}}{2\sqrt{3}} \langle \vec{n}_i | \sigma_i^\mu | \vec{n}_i \rangle \langle \vec{n}_j | \sigma_j^\nu | \vec{n}_j \rangle \langle \vec{n}_k | \sigma_k^\eta | \vec{n}_k \rangle \\
&= \frac{\varepsilon^{\mu\nu\eta}}{2\sqrt{3}} n_i^\mu n_j^\nu n_k^\eta \\
&= \frac{1}{2\sqrt{3}} \vec{n}_i \cdot \vec{n}_j \times \vec{n}_k \\
&= \chi_{ijk}^{class}
\end{aligned} \tag{5.5}$$

The box product was expanded using the Levi-Civita symbol $\varepsilon_{\mu\nu\eta}$, with the sum over all free indices μ , ν , and η implicitly implied, where μ , ν , and η each take values from 1, 2, and 3. This expansion allowed for each Pauli operator σ_l^a to act on particle l , where $a \in \{1, 2, 3\}$ corresponds to the Pauli operators X , Y , and Z , respectively. Notably, for product states, the expectation value of each Pauli component a corresponds to the same component of the classical vector n_l^a . This remarkable result demonstrates that the quantum chirality operator encompasses the classical description, providing a unified framework for characterizing chirality in both classical magnetism and quantum spin- $\frac{1}{2}$ systems.

Additionally, the cycle test method, which was studied in the previous chapter for the context of quantum spin chirality, demonstrates the feasibility of measuring its expectation value. The analysis conducted earlier also reveals the ability to unify the description of chirality in both classical and quantum spin- $\frac{1}{2}$ systems. Consequently, the cycle test method can also be employed to measure the classical chirality in classical magnetism.

Furthermore, the cycle test, as proposed by [Oszmaniec et al. \[2021\]](#), enables the measurement of a specific quantity known as the Bargmann invariants. In the realm of classical magnetism, the imaginary part of the Bargmann invariant Δ_{ijk} (see Equation 5.6) of the product state $|\psi\rangle = |\vec{n}_i\rangle \otimes |\vec{n}_j\rangle \otimes |\vec{n}_k\rangle$ corresponds to the scalar spin chirality. This observation emerged due to the fact that the quantum algorithm for probing chirality in a given state is, in fact, the same as the one used to measure the Bargmann invariants.

$$\Delta_{ijk} = \langle \vec{n}_i | \vec{n}_j \rangle \langle \vec{n}_j | \vec{n}_k \rangle \langle \vec{n}_k | \vec{n}_i \rangle \tag{5.6}$$

$$\langle \psi | \hat{\chi} | \psi \rangle = \frac{2}{\sqrt{3}} \text{Im} \{ \Delta_{ijk} \} \tag{5.7}$$

This connection is not coincidental. In the case of three single-qubit (i.e., spin- $\frac{1}{2}$) states, the imaginary part of Δ_{ijk} is nonzero if and only if χ_{ijk}^{class} is nonzero. This condition precisely corresponds to the

presence of chirality in classical states. However, it should be noted that for entangled states, this geometric interpretation is not possible. However, the cycle test method can still be utilized to probe $\hat{\chi}$.

5.2 Spin chirality and tripartite entanglement of one-magnon states

The previous section aimed to study classical magnetism and demonstrate the applicability of the cycle test to both quantum and classical magnetism. This was done by showcasing that classical states can be described as product states, such as coherent spin states. However, the measurement circuits proposed in the chapter 4 were specifically designed within the context of quantum magnetism. Therefore, in this section, the focus shifts to the investigation of multi-spin- $\frac{1}{2}$ entangled states. Specifically, the chosen system is a spin wave state, also known as a one-magnon state in a one-dimensional lattice. This state is defined as follows.

$$|q\rangle = \frac{1}{\sqrt{N}} \sum_{n=1}^N e^{iqn} S_n^- |\uparrow\uparrow \dots \uparrow\rangle \quad (5.8)$$

Here, N represents the number of sites, S_n^- denotes the spin-lowering operator at site n , and $q = \frac{2\pi}{N}m$ corresponds to the wavenumber of the magnon, where $m \in \{0, 1, 2, \dots, N-1\}$. It is important to note that for the specific case where $N = 3$, the spin waves are eigenstates of the chirality operator for any value of $q = 0, \pm \frac{2\pi}{3}$. Consequently, the chirality has already been studied in the previous chapters and is presented below.

$$\hat{\chi}|q\rangle = q \frac{3}{2\pi} |q\rangle \quad (5.9)$$

In this context, a notable difference between classical and quantum chirality becomes evident. The states mentioned above exhibit non-zero chirality for $q \neq 0$ and are entangled states. Unlike classical magnetism, there is no classical geometric interpretation for this property. To illustrate this point further, let's compute the classical spin projection for each particle i , denoted as $\vec{s}_i = (\langle S_i^x \rangle, \langle S_i^y \rangle, \langle S_i^z \rangle)$. It becomes apparent that when $q = \frac{2\pi}{3}$, all sites $i \in \{1, 2, 3\}$ have parallel classical vectors, given by $\vec{s}_i = (0, 0, \frac{1}{6})$ for all i . Consequently, the classical chirality in this case is zero, once again highlighting the distinction from quantum chirality.

Moreover, the chirality of a general spin wave state $|q\rangle$, consisting of N particles, can be computed by utilizing the definition of the chirality operator in terms of the cyclical permutation operator $R = P_{23}P_{31}$.

This approach allows us to straightforwardly obtain the scalar spin chirality for any trio of particles in an N site spin-wave state. After some straightforward algebra, we find that the chirality expectation value can be easily calculated using the following equation:

$$\langle q | \hat{\chi}_{n_1, n_2, n_3} | q \rangle = \frac{2 [\sin(q\Delta_{21}) + \sin(q\Delta_{32}) + \sin(q\Delta_{13})]}{N\sqrt{3}} \quad (5.10)$$

Here, $\Delta_{ij} \equiv n_i - n_j$, with n_1, n_2, n_3 labeling arbitrary sites. On the other hand, recent works show the relationship between chirality and genuine tripartite entanglement (GTE), indicating that the existence of chirality can serve as a witness of the presence of GTE. In this work, it is demonstrated that if the scalar spin chirality of a given state is above $\frac{1}{\sqrt{3}}$ (after normalization), it is a witness that the state possesses genuine tripartite entanglement (GTE) [Tsomokos et al. \[2008\]](#).

Therefore, the maximum scalar spin chirality for any trio of spins- $\frac{1}{2}$ for spin-wave states defined on $N \in [3, 10]$ sites was computed and compared with the values obtained through the evaluation of the concurrence fill, which is a metric used to identify GTE [Xie and Eberly \[2021\]](#). These results are summarized in Figure 27.

The calculations show that while the scalar spin chirality only guarantees the existence of GTE in the spin-wave states for $N = 3$ sites, non-zero concurrence values are obtained for larger N , confirming the presence of tripartite entanglement. However, it appears that the tripartite entanglement vanishes for sufficiently large system sizes. This contrasts with the macroscopic bipartite entanglement of magnons in the thermodynamic limit, as reported in the literature [Morimae et al. \[2005\]](#), [Zou et al. \[2020\]](#).

5.3 Scalar spin chirality in spin spirals

In this section, our goal is to compute the scalar spin chirality for the ground state $|\psi_0\rangle$ of the model presented in Equation 5.11. We are interested in studying this system because, in contrast with the previous cases, where the product of coherent states only exhibits classical chirality, and in the magnons system, there is only quantum spin chirality. This system presents both classical and quantum chirality in the broken-symmetry case.

$$\hat{H} = -J \sum_{\langle i, j \rangle} \vec{S}_i \cdot \vec{S}_j + \vec{D} \cdot \sum_{\langle i, j \rangle} \vec{S}_i \times \vec{S}_j + B_x \hat{S}_1^x + B \sum_i \hat{S}_i^z \quad (5.11)$$

Here, the notation $\langle i, j \rangle$ indicates the coupling between first-neighbors for a system comprising N particles under periodic boundary conditions. The Hamiltonian consists of a Heisenberg ferromagnetic

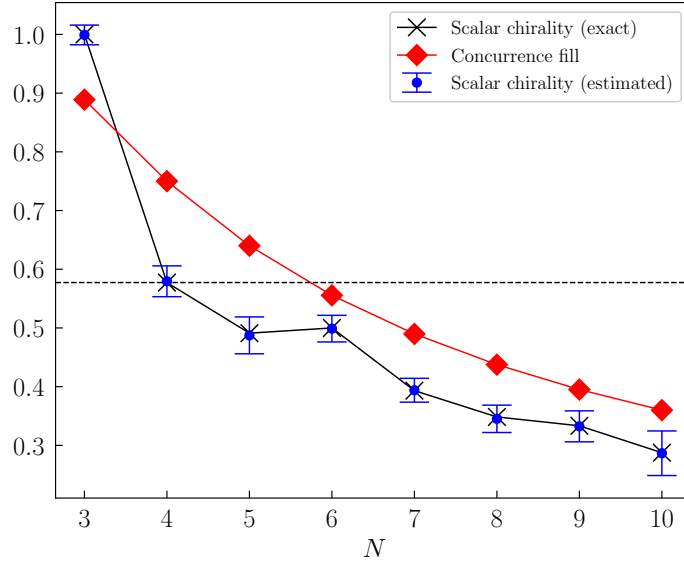


Figure 27: Estimation of scalar spin chirality $\hat{\chi}$ in spin-wave states defined on an N -site ring. The maximal value of $\hat{\chi}$ across all trios of spins- $\frac{1}{2}$ and all N spin-wave states is shown in black (Equation 5.10). The same values were estimated using the Hadamard test in Fig. 25 with 10,000 samples for each N , shown in blue. The horizontal dashed line marks the threshold for genuine tripartite entanglement [Tsomokos et al. \[2008\]](#). While the scalar spin chirality surpasses this threshold only for $N = 3$, the concurrence fill [Xie and Eberly \[2021\]](#), a measure of tripartite entanglement, confirms its existence for all system sizes in the plot. The black and red solid lines emphasize the decay of $\hat{\chi}$ and the concurrence fill with the system size N .

term ($J > 0$), the Dzyaloshinskii-Moriya (DM) interaction $\vec{D} = D\hat{z}$, a local magnetic field B_x along the \hat{x} direction acting on the first spin, and the Zeeman interaction with the magnetic field B in the \hat{z} direction.

5.3.1 Classical treatment

In this classical treatment, we consider the Ferromagnetic and Dzyaloshinskii-Moriya interactions. The ferromagnetic interaction which favors the alignment of the spins along the same direction, while the Dzyaloshinskii-Moriya (DM) interaction affects the components of the spins in the plane perpendicular to the vector \vec{D} . The DM interaction tends to align the spins perpendicularly to their local neighbors. This competition between the interactions leads to the formation of classical spin spirals, as spins try to simultaneously align along the ferromagnetic direction and adjust their orientation to be perpendicular to the \vec{D} vector.

Therefore, the spins particles in classical magnetism can be described in terms of vectors $\vec{S}_i = S\vec{n}_i$

(see Equation 5.12), where \vec{n}_i is the unit vector as shown in Figure 26a. Here, all spins have the same azimuthal angle $\theta_i = \theta$, which is a reasonable simplification since the system is symmetric under rotation around the axis parallel to \vec{D} . However, they have different polar angles φ_i , which characterize the spin spiral.

$$\vec{S}_i = S (\cos \varphi_i \sin \theta \hat{x} + \sin \varphi_i \sin \theta \hat{y} + \cos \theta \hat{z}) \quad (5.12)$$

Hence, considering a one-dimensional system with N spin particles and periodic boundary conditions, the classical energy E of the system can be rewritten as follows:

$$E = -J \sum_{\langle i,j \rangle} S^2 \cos(\varphi_j - \varphi_i) \sin^2 \theta + \cos^2 \theta + D \sum_{\langle i,j \rangle} S^2 \sin(\varphi_j - \varphi_i) \sin^2 \theta \quad (5.13)$$

Here, it is possible to write each polar angle in terms of the spiral wave vector q as $\varphi_i = qr_i$, where $r_i = a(i - 1)$ is the position vector of each particle $i \in [1, N]$ in the ring with a lattice constant $a = 1$. Therefore, since the interactions are considered only for first neighbors, the energy of the system depends on the wave number of the spiral.

$$E(q) = NS^2 (D \sin q - J \cos q) \sin^2 \theta - NJS^2 \cos^2 \theta \quad (5.14)$$

Therefore, the first thing to find is the condition for the wave number q_{\min} that minimizes the energy of the system, which will correspond to its ground state. This can be achieved by computing the partial derivative of E with respect to q , as shown below.

$$\frac{\partial E}{\partial q} = NS^2 (D \cos q + J \sin q) \sin^2 \theta = 0 \quad (5.15)$$

$$\tan q_{\min} = -\frac{D}{J} \quad (5.16)$$

By replacing the value of D obtained from the condition found above, we can see that the value of the azimuthal angle θ that minimizes the ground energy is given by $\theta = \frac{\pi}{2}$. This means that in the ground state, the spins in the classical spin spiral are aligned perpendicular to the \vec{D} vector, confirming the result described initially.

$$E(q_{\min}) = NS^2 D \sin q_{\min} - NJS^2 J \cos q_{\min} \quad (5.17)$$

5.3.2 Quantum Ground State and Broken Symmetry

The previous subsection discussed the classical treatment of the problem involving Ferromagnetic and Dzyaloshinskii-Moriya (DM) interactions, whose ground state corresponds to a spin spiral residing in the plane perpendicular to the \vec{D} vector and wave number q_{\min} . In this subsection, we will qualitatively explore the quantum version of this problem and confirm the expected results through simulations using QuSpin, a Python package that offers open-source tools for exact diagonalization and quantum dynamics simulations of various many-body systems, including spins [Weinberg and Bukov \[2017, 2019\]](#).

Before delving into the quantum spin spiral, it is essential to note that the system exhibits invariance to global rotations of the spins. Consequently, all spin spirals with the same wave number q_{\min} but different global phase ϕ possess the same energy. As a result, there exists an infinite set of spin spirals that are ground states of the system. Each classical spin vector $\vec{S}_{i,\phi}$ is depicted below.

$$\vec{S}_{i,\phi} = S [\cos(q_{\min}r_i + \phi) \hat{x} + \sin(q_{\min}r_i + \phi) \hat{y}] \quad (5.18)$$

This degeneracy leads to a quantum ground state that is a superposition of all these spin spirals defined by the global phase ϕ . Analytically computing this result can be challenging and is not the primary focus of this work. Instead, we will compare the classical analysis with simulations using QuSpin. In these simulations, we will measure the spin vector \vec{S}_i observables and correlators $\hat{S}_1^\alpha \hat{S}_i^\alpha$ with $\alpha \in \{x, y, z\}$ and $i \in [2, N]$.

In the classical treatment, if we consider a spin spiral with, for example, $\phi = 0$, the measurement of \vec{S}_i will be in the form of $\vec{S}_i, 0$. In the case of the correlators, only $S_1^x S_i^x = S^2 \cos q_{\min}r_i$ is non-zero; the others are zero. On the other hand, if we assume that the ground state is a superposition of all the infinite possibilities of ϕ , the classical result for \vec{S}_i and the correlators would be an average over all values of ϕ , as shown below.

$$\vec{S}_i = \frac{1}{2\pi} \int_0^{2\pi} d\phi \vec{S}_{i,\phi} = 0 \quad (5.19)$$

$$S_1^\alpha S_i^\alpha = \frac{1}{2\pi} \int_0^{2\pi} d\phi S_{1,\phi}^\alpha S_{i,\phi}^\alpha = \frac{S^2}{2} \cos q_{\min}r_i, \quad \alpha \in \{x, y\} \quad (5.20)$$

The first step in the simulation is to choose the spin spiral wave number for the ground state, which should be $q_{\min} = \frac{2\pi}{N}$ for the system with $N = 10$ particles and the ferromagnetic coupling constant $J = 1$. Following the classical ground state condition found in Equation 5.16, we have $D = -J \tan q_{\min}$. This ground state should be a superposition of the infinite possible spin spirals with global phase ϕ , and

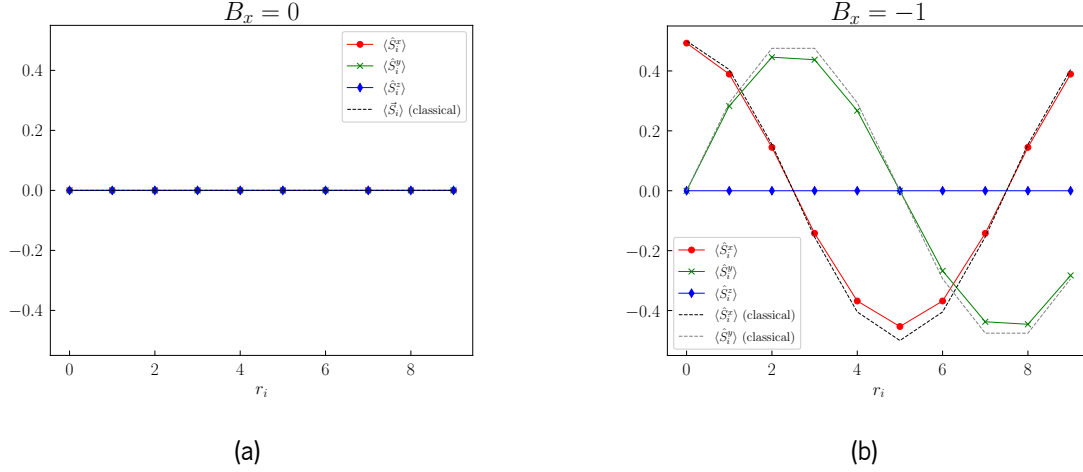


Figure 28: The figures display the simulation results obtained using QuSpin for a ring with $N = 10$ particles, $J = 1$, and $D = -J \tan \frac{2\pi}{N}$. In these simulations, the operator \vec{S}_i was measured for each particle $i \in [1, N]$ in two systems: one without a local magnetic field ($B_x = 0$, 28a) and the other with a local magnetic field ($B_x = -1$, 28b) to achieve a broken-symmetry ground state. The dashed lines in the figures represent the analytical solutions obtained through classical analysis.

the simulation results using QuSpin should be consistent with the classical analysis.

However, to obtain a unique spin spiral, we need to add a local magnetic field $B_x = -1$ located only on the first spin. This will lead to a broken-symmetry ground state that chooses the spin spiral with $\phi = 0$. Again, the simulation results compared with the classical analysis will allow us to confirm that the assumptions were correct. By comparing the simulation results with the classical analysis for both cases (superposition of all ϕ and broken-symmetry ground state with $\phi = 0$), we can verify the expected behavior of the quantum ground state and its agreement with the classical treatment.

The Figures 28 and 29 display the simulation results and their comparison with the classical analysis. Figures 28a and 29a demonstrate the concordance with the case without a local magnetic field ($B_x = 0$), in which the ground state is a superposition of all infinite spin spirals with a phase ϕ . On the other hand, figures 28b and 29b illustrate the case of broken symmetry achieved by adding a local magnetic field ($B_x = -1$), which selects the spin spiral with a global phase $\phi = 0$. In both cases, the classical results obtained previously are shown by dashed lines.

Indeed, these results and their agreement with the classical analysis strongly support the conclusion that the quantum ground state is a degenerate state. In this ground state, the system exists in a superposition of all spin spirals, obtained through global rotations of the spins.

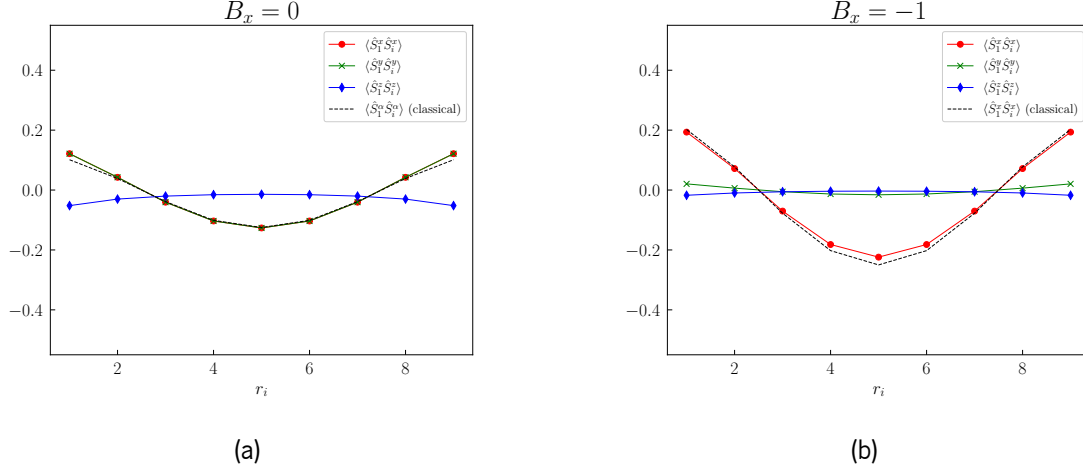


Figure 29: The figures display the simulation results obtained using QuSpin for a ring with $N = 10$ particles, $J = 1$, and $D = -J \tan \frac{2\pi}{N}$. In these simulations, the correlator $S_1^\alpha S_i^\alpha$, $\alpha \in \{x, y, z\}$ was measured for each particle $i \in [2, N]$ in two systems: one without a local magnetic field ($B_x = 0$, 29a) and the other with a local magnetic field ($B_x = -1$, 29b) to achieve a broken-symmetry ground state. The dashed lines in the figures represent the analytical solutions obtained through classical analysis. In subfigure 29a, the dashed lines represent the analytical classical solutions for $\langle S_1^\alpha S_i^\alpha \rangle$, where $\alpha \in \{x, y\}$.

5.3.3 Classical and Quantum Chirality

The goal of studying the chirality of spin spirals is to explore the coexistence of classical and quantum chirality in the broken-symmetry case. When the Zeeman component of the Hamiltonian $B \neq 0$, the spins tend to align with this magnetic field, resulting in a non-coplanar spin structure in the classical description. This non-coplanarity leads to a state with non-zero classical chirality. Moreover, due to the nature of the interactions, the quantum version of the system also exhibits non-zero chirality. The quantum chirality arises from the entanglement of quantum states and is a unique feature of quantum systems.

First, let's calculate the analytical expression for the classical chirality of spin spirals' trios ijk using the definition in terms of the box product of the unit vector \vec{n}_i , as shown below:

$$\chi_{ijk}^{cla} = \frac{1}{2\sqrt{3}} \vec{n}_i \cdot \vec{n}_j \times \vec{n}_k \quad (5.21)$$

where \vec{n}_i , \vec{n}_j , and \vec{n}_k are the unit vectors corresponding to the spins at sites i , j , and k in the spin spiral, respectively. Thus, by using the expression for the classical spins in Equation 5.12 as $\vec{n}_i = \frac{\vec{S}_i}{S}$, the classical chirality can then be written in terms of the azimuthal angle θ , the wave number q_{min} , and the difference between the sites $\Delta\alpha\beta \equiv r_\alpha - r_\beta$ as follows:

$$\chi_{ijk}^{cla} = \frac{\cos \theta \sin^2 \theta [\sin (q_{min} \Delta_{ji}) + \sin (q_{min} \Delta_{kj}) + \sin (q_{min} \Delta_{ik})]}{2\sqrt{3}} \quad (5.22)$$

Note that for the case in which the ground state is a superposition of all the spin spirals, the classical chirality is always zero. This result is obtained based on the conclusions from the previous subsection, as shown in Equation 5.19. Therefore, to obtain a broken-symmetry ground state with classical and quantum chirality, a local magnetic field $B_x = -0.1$ is applied to the first spin. This state corresponds to a single spin spiral with a global phase $\phi = 0$ in the absence of an external magnetic field ($B = 0$).

In this study, a sweep was conducted over the values of B in the range $[0, 1]$, and the classical and quantum chirality were computed for a system with $N = 10$ particles, a ferromagnetic coupling constant $J = 1$, and $D = J \tan(q_{min})$, where $q_{min} = \frac{2\pi}{N}$ ensures that a period of the spin spirals is completed upon covering all N sites.

To obtain the classical ground state of the system, numerical simulation was employed. The classical energy of the system $E(\theta, q)$ (see Equation 5.23) was minimized to find the optimal values for the wave number of the spin spiral q_{min} and the azimuthal angle θ , which depends on the external magnetic field B . Using the analytical expression found in Equation 5.22, the classical chirality was then computed.

$$E(\theta, q) = NS^2 (D \sin q \sin^2 \theta - J \cos q \sin^2 \theta - J \cos^2 \theta) + B_x S \sin \theta + NSB \cos \theta \quad (5.23)$$

The quantum ground state of the system was obtained using QuSpin through exact diagonalization. The quantum operator $\hat{\chi}$ was utilized to obtain the exact quantum chirality for each value of B , and the results were validated by applying the cycle test via noiseless simulation with Qiskit. Furthermore, the classical version of this quantum ground state was obtained by computing the expectation value of each spin component. The classical spin vector is given by $\vec{s}_i = (\langle S_i^x \rangle, \langle S_i^y \rangle, \langle S_i^z \rangle)$ for each particle i , and the box product using these vectors was computed to obtain the classical chirality $\langle \chi_{ijk}^{cla} \rangle$ of the quantum ground state $|\psi_0\rangle$.

$$\langle \psi_0 | \chi_{ijk}^{cla} | \psi_0 \rangle = \frac{4}{\sqrt{3}} \vec{s}_i \cdot \vec{s}_j \times \vec{s}_k \quad (5.24)$$

Hence, Figure 30 shows the results of the simulation where the chirality for the sites 1, 4, and 9 was computed for the cases in which $B_x = 0$ and $B_x = -0.1$. The broken-symmetry case exhibits non-zero classical chirality, as expected. Furthermore, the quantum chirality is larger than the classical chirality due to entanglement, consistent with previous discussions. In the $B_x = 0$ case, the system's chirality is entirely quantum and appears to be discretized along the values of B , representing a fully quantum

phenomenon with no classical explanation.

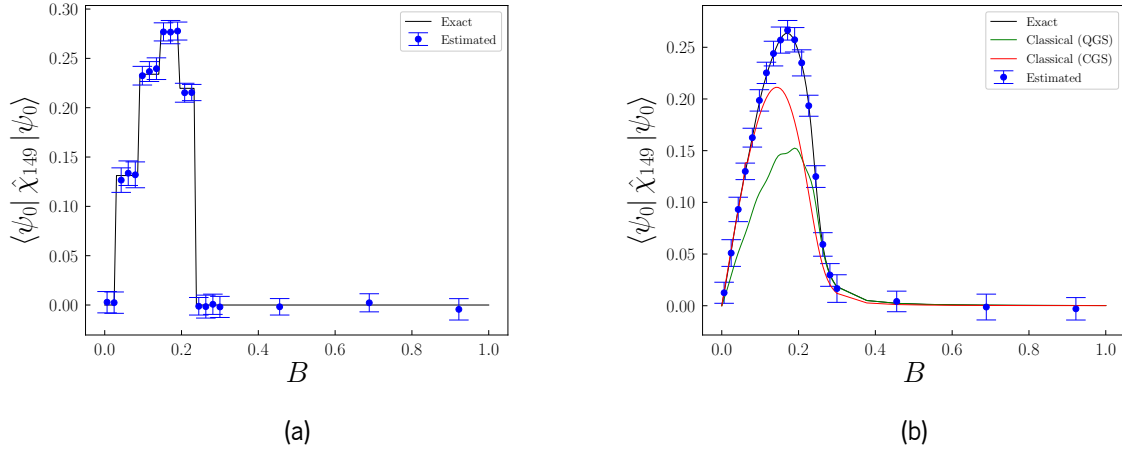


Figure 30: Simulation results for the chirality measurement of the Hamiltonian in Equation 5.11 for $B_x = 0$ (30a) and $B_x = -0.1$ (30b) with varying $B \in [0, 1]$. The Quantum Ground State (QGS) was obtained through exact diagonalization using QuSpin. The Classical Ground State (CGS) was obtained by minimizing the classical energy $E(\theta, q)$ (Equation 5.23). In the case where $B_x = 0$, the ground state is a superposition of an infinite set of spin spirals, resulting in a classical chirality of zero. However, in the case with $B_x = -0.1$, the system leads to a broken-symmetry ground state that allows the existence of classical chirality. Black curve: Exact quantum chirality $\langle \hat{\chi}_{149} \rangle$. Blue dots: Estimated quantum chirality using the cycle test circuit in Qiskit. Green: Classical chirality $\langle \chi_{149}^{cla} \rangle$ computed from the box product of classical spin vectors $\vec{s}_i = (\langle S_i^x \rangle, \langle S_i^y \rangle, \langle S_i^z \rangle)$ over the QGS (see Equation 5.24). Red: Classical chirality χ_{149}^{cla} calculated using Equation 5.22 with values of θ and q_m from the CGS.

The broken-symmetry system with non-zero classical chirality allows us to create a classical representation of the spin vectors and visually show the non-coplanarity achieved due to the Zeeman component. In Figure 31, we present schematic representations for three different values of B .

1. For $B = 0$, the classical configuration is coplanar in the $\hat{x}\hat{y}$ plane.
2. For the chiral case with $B = 0.17$, the non-coplanarity is evident.
3. Lastly, for $B = 1$, the spins are aligned with the external magnetic field, and therefore, the chirality vanishes.

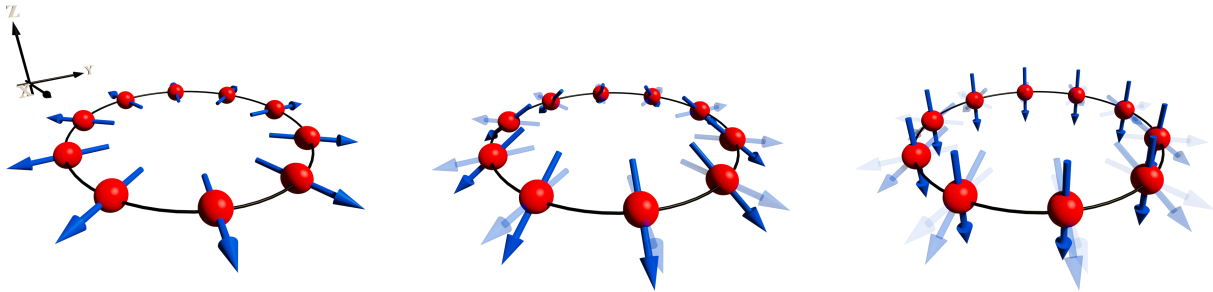


Figure 31: Classical spin vectors for three different values of B . The left figure corresponds to $B = 0$, and its spin configuration is a coplanar spin spiral with zero chirality. In the middle figure, for $B = 0.17$, the maximum quantum chirality is observed, and the non-zero classical chirality is apparent due to the non-coplanar spin configuration. The right figure, for $B = 1$, shows zero chirality, with the spins aligned with the external magnetic field. The chirality values were presented in Figure 30.

Chapter 6

Conclusions and Future Work

6.1 Conclusions

In summary, this dissertation proposes quantum circuits for probing the scalar spin chirality of trios of spin- $\frac{1}{2}$ particles in a wave function defined on an arbitrary lattice. Initially, we studied how to implement chiral states with well-known chirality values, identifying them as chirality eigenstates (Chapter 3). These states were employed to validate various approaches within our research.

The initial approach to address this challenge involved employing the Linear Combination of Unitaries (LCU) method to map the non-Unitary chirality operator $\hat{\chi}$ onto a digital quantum computer (Section 4.2). Through this approach, we established a connection between the probabilistic application of $\hat{\chi}$ and the ancilla measurement, yielding the expectation value $\langle \hat{\chi}^2 \rangle$. Subsequently, by utilizing the Hadamard Test and the LCU technique, we successfully measured the desired chirality expectation value of an input system (Section 4.3).

Another approach to address this problem involved exponentiating the normalized chirality operator to obtain a unitary operator $U_{\chi}(t) = e^{-i\hat{\chi}t}$ (Section 4.4). The implementation of this unitary operator facilitated the use of various techniques, including Quantum Phase Estimation and the Hadamard test, to investigate the chirality of a given system. However, it was demonstrated that implementing this unitary operator for an arbitrary time t would require a substantial number of quantum operations, typically achieved through Trotterization. Nevertheless, through a clever selection of time, specifically $t = \frac{2\pi}{3}$, this unitary operator simplifies to a simple cyclic permutation. This simplified version can be readily implemented in a quantum computer using *SWAP* gates.

Hence, employing this approach in conjunction with other quantum circuits enables the measurement of the chirality operator. The quantum circuit utilizing the Hadamard test with U_{χ} maps the expectation value of either $\hat{\chi}$ or $\hat{\chi}^2$ to the average value of Y or X for the ancillary qubit. When $t = \frac{2\pi}{3}$, the algorithm becomes equivalent to the cycle test (Section 4.6) [Oszmaniec et al. \[2021\]](#).

Furthermore, when the Hadamard test is implemented with a qutrit as the ancilla, it is equivalent to quantum phase estimation (QPE) and enables the single-shot readout of the eigenvalues of $\hat{\chi}$ when the main register is prepared in a corresponding eigenstate (Section 4.5). Importantly, if the main register is initialized in a linear superposition of states with different scalar spin chirality, executing the QPE algorithm causes the wave function to collapse onto the components indicated by the ancilla readout. This approach can be employed as a strategy to prepare states with well-defined scalar spin chirality in selected triads of spins, similar to recently proposed algorithms for preparing valence-bond-solid states [Murta et al. \[2023\]](#) and the Gutzwiller wave function [Murta and Fernández-Rossier \[2021\]](#).

All of the proposed algorithms were assessed in terms of the quantum resources needed to achieve a specific level of precision (Section 4.7). This allowed for the selection of the most efficient approach, which was found to be the cycle test quantum circuit. Subsequently, the cycle test quantum circuit was employed for the remainder of the dissertation's work and was tested in various scenarios.

We have demonstrated the applicability of this method (Chapter 5) to classical magnetism using spin states (Section 5.1). Our results indicate that the cycle test method is effective for both separable and entangled states. Moreover, in the context of classical magnetism, we have established a direct correlation between chirality and the imaginary component of the Bargmann invariant for three particles. This correlation aligns with existing descriptions of chirality, which consider the disparity in Berry Phases [Wen et al. \[1989\]](#).

The application of this method to one-magnon states (Section 5.2) has provided valuable insights into the results proposed by the authors. Specifically, it was demonstrated that for certain chirality values, the system serves as a witness for genuine tripartite entanglement (GTE) [Tsomokos et al. \[2008\]](#). Consequently, chirality measurements were conducted and compared with theoretical predictions made within this work. Notably, it was revealed that only the $N = 3$ magnon state exhibited a significantly high chirality, confirming the presence of GTE. However, as the values were compared with the corresponding concurrence [fill Xie and Eberly \[2021\]](#), it became apparent that for larger values of N , there still existed a certain degree of GTE, which correlated with the limited presence of chirality.

In the thermodynamic limit as $N \rightarrow \infty$, this GTE phenomenon gradually diminishes, which stands in contrast to the well-documented macroscopic bipartite entanglement observed in magnons in the thermodynamic limit as reported in existing literature [Morimae et al. \[2005\]](#), [Zou et al. \[2020\]](#). The final application of the cycle test involved the ground state of a simplified model representing a chiral ferromagnet (Section 5.3). This analysis included a classical treatment to examine the behavior of the ground state's spin spiral. Utilizing QuSpin, the quantum ground state was obtained and subsequently compared

with the results of the earlier classical analysis. To explore this system further, the chirality of the ground state was measured under various external magnetic field strengths, denoted as B . The measurements were conducted using QuSpin to determine the theoretical chirality, while the cycle test, implemented with Qiskit for a noiseless simulation, was employed to estimate the chirality.

This project served as an invaluable learning experience, encompassing the acquisition of fundamental concepts within the field of quantum magnetism and its associated formalism, which underpins this dissertation. Furthermore, it involved an educational journey in quantum simulation, encompassing a solid foundation in quantum simulation principles.

The project also entailed a comprehensive study of various quantum algorithms, each with significant applications in different facets of quantum simulation, allowing for the simulation of a wide range of systems. Consequently, the knowledge gained throughout this endeavor not only proved pivotal in achieving the primary objectives of the dissertation but also serves as a valuable resource for addressing future challenges within the domain of quantum simulation.

In conclusion, our findings represent a significant step forward in the realm of efficient digital quantum simulation of magnetic materials with chiral characteristics. Furthermore, our quantum methodologies establish a crucial bridge between the scalar spin chirality formula, a staple in classical magnetism descriptions often formulated in terms of product states, and its quantum counterpart, which extends its applicability to entangled states.

6.2 Future Work

Future work will address the extension of our results to the determination of the scalar spin chirality of spin systems with $S > \frac{1}{2}$. This will involve investigating how our quantum circuit methodologies can serve as motivation to adapt the description of quantum chirality to handle higher spin states.

Additionally, we will focus on the generalization of the chirality concept to sets of more than three spins. One promising avenue for this generalization is building upon the relation we discovered between the chirality and Bargmann invariants, as well as the self-definition of chirality in terms of Berry Phases. Therefore, the generalization will likely emerge from a broader concept of chirality related to cyclical permutations. Exploring the behavior of chirality in larger spin systems will provide valuable insights into the complex interactions that arise in such systems. Overall, these future research directions aim to expand the applicability of our findings and contribute to a deeper understanding of the theory of chirality, motivated by the quantum computing approach developed in this dissertation.

Bibliography

Daniel S Abrams and Seth Lloyd. Quantum algorithm providing exponential speed increase for finding eigenvalues and eigenvectors. *Physical Review Letters*, 83(24):5162, 1999.

Dorit Aharonov, Vaughan Jones, and Zeph Landau. A polynomial quantum algorithm for approximating the jones polynomial. In *Proceedings of the thirty-eighth annual ACM symposium on Theory of computing*, pages 427–436, 2006.

Baptiste Anselme Martin, Pascal Simon, and Marko J. Rančić. Simulating strongly interacting hubbard chains with the variational hamiltonian ansatz on a quantum computer. 4(2):023190, 2022. ISSN 2643-1564. doi: 10.1103/PhysRevResearch.4.023190. URL <https://link.aps.org/doi/10.1103/PhysRevResearch.4.023190>.

Adriano Barenco, Charles H Bennett, Richard Cleve, David P DiVincenzo, Norman Margolus, Peter Shor, Tycho Sleator, John A Smolin, and Harald Weinfurter. Elementary gates for quantum computation. *Physical review A*, 52(5):3457, 1995.

Bela Bauer, Sergey Bravyi, Mario Motta, and Garnet Kin-Lic Chan. Quantum algorithms for quantum chemistry and quantum materials science. 120(22):12685–12717, 2020. ISSN 0009-2665, 1520-6890. doi: 10.1021/acs.chemrev.9b00829. URL <https://pubs.acs.org/doi/10.1021/acs.chemrev.9b00829>.

Katherine L. Brown, William J. Munro, and Vivien M. Kendon. Using quantum computers for quantum simulation. 12(11):2268–2307, 2010. ISSN 1099-4300. doi: 10.3390/e12112268. URL <https://www.mdpi.com/1099-4300/12/11/2268>. Number: 11 Publisher: Molecular Diversity Preservation International.

Alessandro Carbone, Davide Emilio Galli, Mario Motta, and Barbara Jones. Quantum circuits for the preparation of spin eigenfunctions on quantum computers. 14(3):624, 2022. ISSN 2073-8994. doi: 10.3390/sym14030624. URL <https://www.mdpi.com/2073-8994/14/3/624>. Number: 3 Publisher: Multidisciplinary Digital Publishing Institute.

- Arnaud Carignan-Dugas, Joel J Wallman, and Joseph Emerson. Characterizing universal gate sets via dihedral benchmarking. *Physical Review A*, 92(6):060302, 2015.
- Yanran Cheng and Zhihui Lou. A brief review of linear regression estimation in quantum tomography. In *2020 39th Chinese Control Conference (CCC)*, pages 5813–5817, 2020. doi: 10.23919/CCC50068.2020.9188692.
- Andrew M Childs. Lecture notes on quantum algorithms. *Lecture notes at University of Maryland*, 2017.
- Andrew M Childs and Nathan Wiebe. Hamiltonian simulation using linear combinations of unitary operations. *arXiv preprint arXiv:1202.5822*, 2012.
- Daniel Claudino. The basics of quantum computing for chemists. 122(23):e26990, 2022. ISSN 1097-461X. doi: 10.1002/qua.26990. URL <https://onlinelibrary.wiley.com/doi/abs/10.1002/qua.26990>. _eprint: <https://onlinelibrary.wiley.com/doi/pdf/10.1002/qua.26990>.
- Richard Cleve, Artur Ekert, Chiara Macchiavello, and Michele Mosca. Quantum algorithms revisited. *Proceedings of the Royal Society of London. Series A: Mathematical, Physical and Engineering Sciences*, 454(1969):339–354, 1998.
- Don Coppersmith. An approximate fourier transform useful in quantum factoring. *arXiv preprint quant-ph/0201067*, 2002.
- Michael G Cottam and Zahra Haghshenasfard. *Many-body theory of condensed matter systems: An Introductory course*. Cambridge University Press, 2020.
- Andrew W Cross, Lev S Bishop, John A Smolin, and Jay M Gambetta. Open quantum assembly language. *arXiv preprint arXiv:1707.03429*, 2017.
- Diogo Cruz, Romain Fournier, Fabien Gremion, Alix Jeannerot, Kenichi Komagata, Tara Tomic, Jarla Thiesbrummel, Chun Lam Chan, Nicolas Macris, Marc-André Dupertuis, and Clément Javerzac-Galy. Efficient quantum algorithms for ghz and w states, and implementation on the ibm quantum computer. *Advanced Quantum Technologies*, 2(5-6):1900015, 2019. doi: <https://doi.org/10.1002/qute.201900015>. URL <https://onlinelibrary.wiley.com/doi/abs/10.1002/qute.201900015>.
- Pedro MQ Cruz and Bruno Murta. Shallow unitary decompositions of quantum fredkin and toffoli gates for connectivity-aware equivalent circuit averaging. *arXiv preprint arXiv:2305.18128*, 2023.

- Andrew J. Daley, Immanuel Bloch, Christian Kokail, Stuart Flannigan, Natalie Pearson, Matthias Troyer, and Peter Zoller. Practical quantum advantage in quantum simulation. 607(7920):667–676, 2022. ISSN 1476-4687. doi: 10.1038/s41586-022-04940-6. URL <https://www.nature.com/articles/s41586-022-04940-6>. Number: 7920 Publisher: Nature Publishing Group.
- GM D'Ariano and P Lo Presti. Quantum tomography for measuring experimentally the matrix elements of an arbitrary quantum operation. *Physical review letters*, 86(19):4195, 2001.
- Miroslav Dobšiček, Göran Johansson, Vitaly Shumeiko, and Göran Wendin. Arbitrary accuracy iterative quantum phase estimation algorithm using a single ancillary qubit: A two-qubit benchmark. *Physical Review A*, 76(3):030306, 2007.
- W. Dür, G. Vidal, and J. I. Cirac. Three qubits can be entangled in two inequivalent ways. *Phys. Rev. A*, 62:062314, Nov 2000. doi: 10.1103/PhysRevA.62.062314. URL <https://link.aps.org/doi/10.1103/PhysRevA.62.062314>.
- Igor Dzyaloshinsky. A thermodynamic theory of “weak” ferromagnetism of antiferromagnetics. *Journal of physics and chemistry of solids*, 4(4):241–255, 1958.
- Albert Fert, Nicolas Reyren, and Vincent Cros. Magnetic skyrmions: advances in physics and potential applications. *Nature Reviews Materials*, 2(7):1–15, 2017.
- Richard P. Feynman. Simulating physics with computers. 21(6):467–488, 1982. ISSN 1572-9575. doi: 10.1007/BF02650179. URL <https://doi.org/10.1007/BF02650179>.
- Richard P Feynman. Quantum mechanical computers. *Optics news*, 11(2):11–20, 1985.
- S. Flannigan, N. Pearson, G. H. Low, A. Buyskikh, I. Bloch, P. Zoller, M. Troyer, and A. J. Daley. Propagation of errors and quantitative quantum simulation with quantum advantage. (arXiv:2204.13644), 2022. URL <http://arxiv.org/abs/2204.13644>.
- Charles R. Harris, K. Jarrod Millman, Stéfan J. van der Walt, Ralf Gommers, Pauli Virtanen, David Cournapeau, Eric Wieser, Julian Taylor, Sebastian Berg, Nathaniel J. Smith, Robert Kern, Matti Picus, Stephan Hoyer, Marten H. van Kerkwijk, Matthew Brett, Allan Haldane, Jaime Fernández del Río, Mark Wiebe, Pearu Peterson, Pierre Gérard-Marchant, Kevin Sheppard, Tyler Reddy, Warren Weckesser, Hameer Abbasi, Christoph Gohlke, and Travis E. Oliphant. Array programming with NumPy. *Nature*, 585(7825):357–362, September 2020. doi: 10.1038/s41586-020-2649-2. URL <https://doi.org/10.1038/s41586-020-2649-2>.

- Loic Henriët, Lucas Beguin, Adrien Signoles, Thierry Lahaye, Antoine Browaeys, Georges-Olivier Reymond, and Christophe Jurczak. Quantum computing with neutral atoms. 4:327, 2020. ISSN 2521-327X. doi: 10.22331/q-2020-09-21-327. URL <http://arxiv.org/abs/2006.12326>.
- Roger A Horn and Charles R Johnson. Norms for vectors and matrices. pages 313–386. Cambridge University Press Cambridge, 1990.
- J. D. Hunter. Matplotlib: A 2d graphics environment. *Computing in Science & Engineering*, 9(3):90–95, 2007. doi: 10.1109/MCSE.2007.55.
- Youngseok Kim, Andrew Eddins, Sajant Anand, Ken Xuan Wei, Ewout Van Den Berg, Sami Rosenblatt, Hasan Nayfeh, Yantao Wu, Michael Zaletel, Kristan Temme, et al. Evidence for the utility of quantum computing before fault tolerance. *Nature*, 618(7965):500–505, 2023.
- Aleks Kissinger and John van de Wetering. PyZX: Large Scale Automated Diagrammatic Reasoning. In Bob Coecke and Matthew Leifer, editors, Proceedings 16th International Conference on *Quantum Physics and Logic*, Chapman University, Orange, CA, USA., 10-14 June 2019, volume 318 of *Electronic Proceedings in Theoretical Computer Science*, pages 229–241. Open Publishing Association, 2020. doi: 10.4204/EPTCS.318.14.
- A. Yu. Kitaev. Quantum measurements and the abelian stabilizer problem. 1995. doi: 10.48550/ARXIV.QUANT-PH/9511026. URL <https://arxiv.org/abs/quant-ph/9511026>.
- Pieter Kok. *A first introduction to quantum physics*. Springer, 2018.
- Seth Lloyd. Universal quantum simulators. 273(5278):1073–1078, 1996. ISSN 0036-8075, 1095-9203. doi: 10.1126/science.273.5278.1073. URL <https://www.science.org/doi/10.1126/science.273.5278.1073>.
- Shi-Yuan Ma, Sheng-Wen Li, Han Cai, Da-Wei Wang, and Hichem Eleuch. Chiral spin flipping gate implemented in ibm quantum experience. *Appl. Math. Inf. Sci*, 11(5):1519–1526, 2017.
- Vladimir V Mazurenko, Iliia A Iakovlev, Oleg M Sotnikov, and Mikhail I Katsnelson. Estimating patterns of classical and quantum skyrmion states. *Journal of the Physical Society of Japan*, 92(8):081004, 2023.
- Sam McArdle, Tyson Jones, Suguru Endo, Ying Li, Simon C Benjamin, and Xiao Yuan. Variational ansatz-based quantum simulation of imaginary time evolution. *npj Quantum Information*, 5(1):1–6, 2019.

Jarrod R. McClean, Ryan Babbush, Peter J. Love, and Alán Aspuru-Guzik. Exploiting locality in quantum computation for quantum chemistry. 5(24):4368–4380, 2014. doi: 10.1021/jz501649m. URL <https://doi.org/10.1021/jz501649m>. Publisher: American Chemical Society.

Eugen Merzbacher. *Quantum mechanics*. John Wiley & Sons, 1998.

Albert Messiah. *Quantum mechanics*. Courier Corporation, 2014.

Aaron Meurer, Christopher P. Smith, Mateusz Paprocki, Ondřej Čertík, Sergey B. Kirpichev, Matthew Rocklin, AMiT Kumar, Sergiu Ivanov, Jason K. Moore, Sartaj Singh, Thilina Rathnayake, Sean Vig, Brian E. Granger, Richard P. Muller, Francesco Bonazzi, Harsh Gupta, Shivam Vats, Fredrik Johansson, Fabian Pedregosa, Matthew J. Curry, Andy R. Terrel, Štěpán Roučka, Ashutosh Saboo, Isuru Fernando, Sumith Kulal, Robert Cimrman, and Anthony Scopatz. Sympy: symbolic computing in python. *PeerJ Computer Science*, 3:e103, January 2017. ISSN 2376-5992. doi: 10.7717/peerj-cs.103. URL <https://doi.org/10.7717/peerj-cs.103>.

Kosuke Mitarai and Keisuke Fujii. Methodology for replacing indirect measurements with direct measurements. 1(1):013006, 2019. ISSN 2643-1564. doi: 10.1103/PhysRevResearch.1.013006. URL <https://link.aps.org/doi/10.1103/PhysRevResearch.1.013006>.

Christopher Monroe, Wes C Campbell, LM Duan, Z-X Gong, Alexey V Gorshkov, PW Hess, R Islam, K Kim, Norbert M Linke, Guido Pagano, et al. Programmable quantum simulations of spin systems with trapped ions. *Reviews of Modern Physics*, 93(2):025001, 2021.

Tomoyuki Morimae, Ayumu Sugita, and Akira Shimizu. Macroscopic entanglement of many-magnon states. *Phys. Rev. A*, 71:032317, Mar 2005. doi: 10.1103/PhysRevA.71.032317. URL <https://link.aps.org/doi/10.1103/PhysRevA.71.032317>.

Tôru Moriya. Anisotropic superexchange interaction and weak ferromagnetism. *Physical review*, 120(1):91, 1960.

Mikko Möttönen, Juha J Vartiainen, Ville Bergholm, and Martti M Salomaa. Quantum circuits for general multiqubit gates. *Physical review letters*, 93(13):130502, 2004.

Bruno Murta and J. Fernández-Rossier. Gutzwiller wave function on a digital quantum computer. *Phys. Rev. B*, 103:L241113, Jun 2021. doi: 10.1103/PhysRevB.103.L241113. URL <https://link.aps.org/doi/10.1103/PhysRevB.103.L241113>.

- Bruno Murta, Pedro M. Q. Cruz, and J. Fernández-Rossier. Preparing valence-bond-solid states on noisy intermediate-scale quantum computers. *Phys. Rev. Res.*, 5:013190, Mar 2023. doi: 10.1103/PhysRevResearch.5.013190. URL <https://link.aps.org/doi/10.1103/PhysRevResearch.5.013190>.
- Michael A Nielsen and Isaac Chuang. *Quantum computation and quantum information*. American Association of Physics Teachers, 2002.
- Michał Oszmaniec, Daniel J Brod, and Ernesto F Galvão. Measuring relational information between quantum states, and applications. *arXiv:2109.10006*, 2021. URL <https://arxiv.org/abs/2109.10006>.
- John Parkinson and Damian J J Farnell. *An Introduction to Quantum Spin Systems*, volume 816 of *Lecture Notes in Physics*. Springer Berlin Heidelberg, 2010. ISBN 978-3-642-13289-6 978-3-642-13290-2. doi: 10.1007/978-3-642-13290-2. URL <http://link.springer.com/10.1007/978-3-642-13290-2>.
- Alberto Peruzzo, Jarrod McClean, Peter Shadbolt, Man-Hong Yung, Xiao-Qi Zhou, Peter J Love, Alán Aspuru-Guzik, and Jeremy L O'brien. A variational eigenvalue solver on a photonic quantum processor. *Nature communications*, 5(1):4213, 2014.
- Antonio Sergio Teixeira Pires. *Theoretical tools for spin models in magnetic systems*. IOP Publishing, 2021.
- John Preskill. Quantum computing in the NISQ era and beyond. 2:79, 2018. ISSN 2521-327X. doi: 10.22331/q-2018-08-06-79. URL <http://arxiv.org/abs/1801.00862>.
- Qiskit contributors. Qiskit: An open-source framework for quantum computing, 2023. URL <https://doi.org/10.5281/zenodo.2573505>.
- A Roldán-Molina, MJ Santander, AS Nunez, and Joaquín Fernández-Rossier. Quantum fluctuations stabilize skyrmion textures. *Physical Review B*, 92(24):245436, 2015.
- Jun John Sakurai and Eugene D Commins. *Modern quantum mechanics, revised edition*. American Association of Physics Teachers, 1995.
- Diptiman Sen and R Chitra. Large- u limit of a hubbard model in a magnetic field: Chiral spin interactions and paramagnetism. *Physical Review B*, 51(3):1922, 1995.

- OM Sotnikov, VV Mazurenko, J Colbois, F Mila, MI Katsnelson, and EA Stepanov. Probing the topology of the quantum analog of a classical skyrmion. *Physical Review B*, 103(6):L060404, 2021.
- OM Sotnikov, IA Iakovlev, AA Iliasov, MI Katsnelson, AA Bagrov, and VV Mazurenko. Certification of quantum states with hidden structure of their bitstrings. *npj Quantum Information*, 8(1):41, 2022.
- V. Subrahmanyam. Chirality operators for heisenberg spin systems. 50(9):6468–6470, 1994. ISSN 0163-1829, 1095-3795. doi: 10.1103/PhysRevB.50.6468. URL <https://link.aps.org/doi/10.1103/PhysRevB.50.6468>.
- Masuo Suzuki. Improved trotter-like formula. *Physics Letters A*, 180(3):232–234, 1993.
- Francesco Tacchino, Alessandro Chiesa, Stefano Carretta, and Dario Gerace. Quantum computers as universal quantum simulators: State-of-the-art and perspectives. 3(3): 1900052, 2020. ISSN 2511-9044. doi: 10.1002/qute.201900052. URL <https://onlinelibrary.wiley.com/doi/abs/10.1002/qute.201900052>. _eprint: <https://onlinelibrary.wiley.com/doi/pdf/10.1002/qute.201900052>.
- Y Taguchi, Y Oohara, H Yoshizawa, N Nagaosa, and Y Tokura. Spin chirality, Berry phase, and anomalous hall effect in a frustrated ferromagnet. *Science*, 291(5513):2573–2576, 2001.
- Tetsufumi Tanamoto. Generation of chiral spin state by quantum simulation. *Phys. Rev. B*, 93:235137, Jun 2016. doi: 10.1103/PhysRevB.93.235137. URL <https://link.aps.org/doi/10.1103/PhysRevB.93.235137>.
- Hristo S Tonchev and Nikolay V Vitanov. Quantum phase estimation and quantum counting with qudits. *Physical Review A*, 94(4):042307, 2016.
- Hale F Trotter. On the product of semi-groups of operators. *Proceedings of the American Mathematical Society*, 10(4):545–551, 1959.
- Dimitris I. Tsomokos, Juan José García-Ripoll, Nigel R. Cooper, and Jiannis K. Pachos. Chiral entanglement in triangular lattice models. *Phys. Rev. A*, 77:012106, Jan 2008. doi: 10.1103/PhysRevA.77.012106. URL <https://link.aps.org/doi/10.1103/PhysRevA.77.012106>.
- Guido Van Rossum, Fred L Drake, et al. *Python reference manual*, volume 111. Centrum voor Wiskunde en Informatica Amsterdam, 1995.

Pauli Virtanen, Ralf Gommers, Travis E. Oliphant, Matt Haberland, Tyler Reddy, David Cournapeau, Evgeni Burovski, Pearu Peterson, Warren Weckesser, Jonathan Bright, Stéfan J. van der Walt, Matthew Brett, Joshua Wilson, K. Jarrod Millman, Nikolay Mayorov, Andrew R. J. Nelson, Eric Jones, Robert Kern, Eric Larson, C J Carey, İlhan Polat, Yu Feng, Eric W. Moore, Jake VanderPlas, Denis Laxalde, Josef Perktold, Robert Cimrman, Ian Henriksen, E. A. Quintero, Charles R. Harris, Anne M. Archibald, Antônio H. Ribeiro, Fabian Pedregosa, Paul van Mulbregt, and SciPy 1.0 Contributors. SciPy 1.0: Fundamental Algorithms for Scientific Computing in Python. *Nature Methods*, 17:261–272, 2020. doi: 10.1038/s41592-019-0686-2.

Da-Wei Wang, Chao Song, Wei Feng, Han Cai, Da Xu, Hui Deng, Hekang Li, Dongning Zheng, Xiaobo Zhu, H. Wang, Shi-Yao Zhu, and Marlan O. Scully. Synthesis of antisymmetric spin exchange interaction and chiral spin clusters in superconducting circuits. 15(4):382–386, 2019. ISSN 1745-2473, 1745-2481. doi: 10.1038/s41567-018-0400-9. URL <http://www.nature.com/articles/s41567-018-0400-9>.

Phillip Weinberg and Marin Bukov. Quspin: a python package for dynamics and exact diagonalisation of quantum many body systems part i: spin chains. *SciPost Physics*, 2(1):003, 2017.

Phillip Weinberg and Marin Bukov. Quspin: a python package for dynamics and exact diagonalisation of quantum many body systems. part ii: bosons, fermions and higher spins. *SciPost Physics*, 7(2):020, 2019.

X. G. Wen, Frank Wilczek, and A. Zee. Chiral spin states and superconductivity. 39(16):11413–11423, 1989. ISSN 0163-1829. doi: 10.1103/PhysRevB.39.11413. URL <https://link.aps.org/doi/10.1103/PhysRevB.39.11413>.

Samuel A Wilkinson and Michael J Hartmann. Superconducting quantum many-body circuits for quantum simulation and computing. *Applied Physics Letters*, 116(23):230501, 2020.

William K Wootters. Entanglement of formation of an arbitrary state of two qubits. *Physical Review Letters*, 80(10):2245, 1998.

Mingzhong Wu and Axel Hoffmann. *Recent advances in magnetic insulators-from spintronics to microwave applications*. Academic Press, 2013.

Songbo Xie and Joseph H. Eberly. Triangle measure of tripartite entanglement. *Phys. Rev. Lett.*, 127:

040403, Jul 2021. doi: 10.1103/PhysRevLett.127.040403. URL <https://link.aps.org/doi/10.1103/PhysRevLett.127.040403>.

Ji Zou, Se Kwon Kim, and Yaroslav Tserkovnyak. Tuning entanglement by squeezing magnons in anisotropic magnets. *Phys. Rev. B*, 101:014416, Jan 2020. doi: 10.1103/PhysRevB.101.014416. URL <https://link.aps.org/doi/10.1103/PhysRevB.101.014416>.

